

國立交通大學
機械工程研究所
碩士論文

TFT-LCD 電漿背光源之二維流體模式模擬

Two-Dimensional Fluid Modeling of a Plasma Backlight Source

for TFT-LCD panel



研究生：胡孟樺

指導教授：吳宗信 博士

中華民國九十五年七月

TFT-LCD 電漿背光源之二維流體模式模擬

**Two-Dimensional Fluid Modeling of a Plasma Backlight Source for
TFT-LCD Panel**

研究生：胡孟樺
指導教授：吳宗信博士

Student : Meng-Hua Hu
Advisor : Dr. Jong-Shinn Wu

國立交通大學
機械工程研究所
碩士論文



**Submitted to Institute of Mechanical Engineering Collage of
National Chiao Tung University**

**In Partial Fulfillment of the Requirements
for the degree of
Master of Science**

**In
Mechanical Engineering**

July 2006

Hsinchu, Taiwan, Republic of China

中華民國九十五年七月

致謝

在交大兩年的研究所生涯，感謝指導教授 吳宗信老師的關心與教導，讓我無論在研究或做人處世上都成長許多，同時也感謝口試委員傅武雄教授、江仲驊博士和郭添全博士在口試時提供的寶貴意見，以及韓國POSTECH大學Jae-Koo Lee教授提供程式與中華映管公司計畫的支持，在此一併致謝。

感謝學長邵雲龍、許佑霖、連又永、許國賢、李允民、洪捷榮、許哲維、鄭凱文、李富利、黃柏誠、鍾東霖、陳立軒、學姊周欣芸、林姝吟在研究上的教導及協助，從不吝於幫助我解決難題，使得論文能順利完成，感謝同學百彥、育進、偉豪在求學中的相互鼓勵，以及學弟們在生活上的幫助，你們是一輩子的知己。

最後要感謝我最愛的親人，首先感謝父母胡信坤先生與李素珠女士對我辛苦的栽培，因為你們的愛支持我繼續學習，親愛的姐姐、妹妹、老弟，以及姐夫與弟媳，你們關懷與包容，是支持我前進的動力，當然不能漏掉可愛的小侄子皓揚與立承，謝謝你們的陪伴，為繁忙的研究生生活帶來了樂趣。此外，在天國的外婆，請你放心，我會謹記您的教誨，讓自己更加熱觀進取。同時也感謝親愛的楓龍，謝謝你對我的呵護與支持，讓我在研究的路途走的更順遂。

要感謝的人太多，最後再一次獻上我最誠摯的謝意，謝謝你們。

胡孟樺 謹誌

九五年七月于風城交大

TFT-LCD 電漿背光源之二維流體模式模擬

學生：胡孟樺

指導教授：吳宗信

國立交通大學機械工程學系

摘要

CCFL 因為能提供較高的效率與亮度，經常被使用在 LCD 作為背光源。然而，CCFL 因為含汞，在低環境溫度下點火較困難，相對的達到飽和亮度的時間勢必增長。此外，隨著環保意識的增強，各國已逐漸減少工業生產中的用汞量，並積極鼓勵採用無汞的新技術。

不含汞的平面電漿背光源已被發展。平面光源由於可以實現大面積均勻發光，壽命長，無污染等優點而備受重視。本研究使用二維流體模式模擬 TFT-LCD 之電漿背光模組的放電情況。在此流體模式中，考慮中性粒子、帶電粒子與激發態粒子的連續方程以計算各粒子的密度空間分布。電場空間分布則由帕松方程結合連續方程求得。semi-implicit 的數值方法被引用以增加模擬時間差的長度。所有電漿參數的研究與討論主要為求得電漿背光源的最佳化。模擬幾何長度為 20.5 mm，寬為 9.4 mm。

Two-Dimensional Fluid Modeling of a Plasma Backlight Source for TFT-LCD Panel

Student : Meng-Hua Hu

Advisor : Dr. Jong-Shinn Wu

Department of Mechanical Engineering
National Chiao-Tung University

Abstract

Generally CCFL is used in LCD as backlight because it provides high efficacy and brightness. However, the use of mercury leads to difficulties in lamp ignition at low ambient temperature and a relatively long build-up time is necessary for the lamp to reach the saturated luminance level. In addition, a use of mercury is not recommended for environmental protection.

A mercury-free flat discharge fluorescent lamp, plasma backlight, has been developed for LCD backlighting. This research uses a two-dimensional fluid modeling code to investigate the phenomenon of a plasma backlight module cell of TFT-LCD panel. In this fluid model, we have considered the continuity equations of neutral particles, charged particles and excited particles to calculate the density of each species spatial distribution. And we also use the Poisson's equation to calculate the electric field spatial distribution. A semi-implicit numerical method is applied to increase the length of Δt . All plasma parameters are studied and discussed in order to find the optima of backlight source system. The time-dependent distributions of electron density, electron temperature, ion density and excited particles density are obtained during the discharge period in a plasma backlight cell. The two-dimensional simulation geometry length is 20.5 mm, and the width is 9.4 mm.

Table of Contents

摘要	I
Abstract.....	II
Table of Contents.....	III
List of Table.....	V
List of Figures.....	VI
Symbols.....	VIII
Chapter 1 Introduction.....	1
1.1. Motivation	1
1.2. Background.....	2
1.2.1. Numerical Models in Low-temperature Plasma Physics.....	2
1.2.1.1. Fluid Modeling	2
1.2.1.2. Particle Modeling (Particle-In-Cell Method)	3
1.2.1.3. Hybrid Modeling	3
1.2.2. The Plasma Backlight Technology	3
1.3. Literature Survey	5
1.4. The Scope of this Thesis.....	6
Chapter 2 Numerical Methods.....	8
2.1. Global Model.....	8
2.1.1. Modeling Equations.....	8
2.1.2. Derivation of Rate Constants.....	9
2.1.3. Solution Procedures.....	10
2.2. Fluid Model	13
2.2.1. Modeling Equations.....	13
2.2.1.1. Continuity Equation.....	13
2.2.1.2. Momentum Equation with Drift-Diffusion Approximation	14
2.2.1.3. Poisson's Equation for Electrostatic Potential.....	14
2.2.1.4. Radiation Transport Equation.....	15
2.2.2. Discretization of Modeling Equations.....	16
2.2.2.1. Continuity Equation with Drift-Diffusion Approximation.....	16
2.2.2.2. Poisson's Equation.....	19
2.2.2.3. Radiation Transport Equation.....	22
2.2.2.4. Boundary Condition	23
Chapter 3 Simulation of Plasma Backlight	25
3.1 Global simulation	25
3.2 Fluid simulation.....	25
3.2.1. Applied Pulse Voltage.....	26
3.2.2. Parametric Studies	27
Chapter 4 Results and Discussion	28
4.1 Global model	28
4.2 Fluid model.....	28
4.2.1 Typical Test Case.....	29
4.2.2 Efforts of Pulse Frequency	30
4.2.3 Effects of Gas Pressure.....	31
4.2.4 Effects of Duty Ratio.....	31
4.2.5 Effects of Dielectric Thickness.....	32
Chapter 5 Conclusions.....	33
5.1 Summary.....	33
5.2 Recommendations of the Future Work.....	34



List of Table

Table 1. Comparison of LCD backlight options.....	2
Table 2. The important reactions for discharge in Xe gas.....	4
Table 3. Plasma backlight unit details and operating parameters.....	26
Table 4. Details of averaged quantities versus pulse frequency 45~85kHz.	62
Table 5. Details of averaged quantities versus gas pressure 90~120 Torr.....	66
Table 6. Details of averaged quantities versus duty ratio 25~75%.....	70
Table 7. Details of averaged quantities versus dielectric thickness 200~700 μ m.	78



List of Figures

Figure 1.1. Schematic drawing of a cold cathode fluorescent lamp (CCFL).....	38
Figure 1.2. Flow diagram of a PIC-MCC model.....	38
Figure 1.3. Schematic drawing of a plasma backlight unit.....	39
Figure 1.4. Schematic of electrode shape.....	39
Figure 1.5. Plasma backlight micro-discharges.....	40
Figure 1.6. The waveform of applied voltage and load current.....	40
Figure 1.7. Plasma backlight operating principle.....	41
Figure 1.8. Energy level diagram of Xe.....	41
Figure 2.1. Simulation mesh diagram.....	42
Figure 2.2. Computation cell geometry.....	42
Figure 2.3. Dielectric constant ϵ , number n , and mobility μ weight the grid point.....	43
Figure 2.4. Simulation mesh diagram of radiation transport.....	43
Figure 2.5. Neuman boundary condition used on the side boundary.....	44
Figure 3.1. Neutral Xenon ionization cross-section.....	44
Figure 3.2. Schematic of the simulated geometry.....	45
Figure 3.3. Mobility in various E/p	45
Figure 3.4. Diffusion in various E/p	46
Figure 3.5. Energy in various E/p	46
Figure 3.6. Ionization coefficient in various E/p	47
Figure 3.7. The waveform of the applied pulse voltage.....	47
Figure 3.8. Pulse shapes of the applied voltages biased at the electrodes.....	48
Figure 4.1. Plasma density versus frequency.....	48
Figure 4.2. Sheath voltage versus frequency.....	49
Figure 4.3. Electron temperature versus frequency.....	49
Figure 4.4. Mean free path versus frequency.....	50
Figure 4.5. Debye length versus frequency.....	50
Figure 4.6. Applied voltage in (a) $\phi = 0.06T$, (b) $\phi = 0.16T$, (c) $\phi = 0.34T$, (d) $\phi = 0.40T$, (e) $\phi = 0.70T$	51
Figure 4.7. Potential and electric field in (a) $\phi = 0.06T$, (b) $\phi = 0.16T$, (c) $\phi = 0.34T$, (d) $\phi = 0.40T$, (e) $\phi = 0.70T$	52
Figure 4.8. Densities of charged species, e^- , Xe^+ , and Xe_2^+ in (a) $\phi = 0.06T$, (b)	

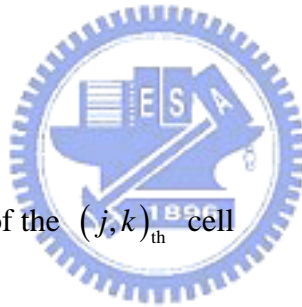
$\phi = 0.16T$, (c) $\phi = 0.34T$, (d) $\phi = 0.40T$, (e) $\phi = 0.70T$	53
Figure 4.9. Densities of excited species , $\text{Xe}^*(^3P_1)$, $\text{Xe}^*(^3P_2)$, and Xe^{**} , in (a) $\phi = 0.06T$, (b) $\phi = 0.16T$, (c) $\phi = 0.34T$, (d) $\phi = 0.40T$, (e) $\phi = 0.70T$	54
Figure 4.10. Densities of excited species, $\text{Xe}_2^*(O_u^+)$, $\text{Xe}_2^*(^1\Sigma_u^+)$, and $\text{Xe}_2^*(^3\Sigma_u^+)$ in (a) $\phi = 0.06T$, (b) $\phi = 0.16T$, (c) $\phi = 0.34T$, (d) $\phi = 0.40T$, (e) $\phi = 0.70T$	55
Figure 4.11. Powers of charged species in (a) $\phi = 0.06T$, (b) $\phi = 0.16T$, (c) $\phi = 0.34T$, (d) $\phi = 0.40T$, (e) $\phi = 0.70T$	56
Figure 4.12. Time evolutions of the spatially averaged quantities @ $f=55\text{kHz}$, V_a $=1740\text{V}$, duty ratio=35%, $P=90\text{torr}$, $T=350\text{K}$	57
Figure 4.13. Cycle averaged quantities of charged species @ $f=55\text{kHz}$, $V_a=1740\text{V}$, duty ratio= 35%, $P=90\text{torr}$, $T=350\text{K}$	58
Figure 4.14. Cycle averaged quantities of excited species @ f 55kHz, V_a 1740V, duty ratio 35%, P 90torr, T 350K.	58
Figure 4.15. Time evolutions of the spatially averaged densities of charged species versus pulse frequency 45~85kHz.....	59
Figure 4.16. Time evolutions of the spatially averaged densities of excited species versus pulse frequency 45~85kHz.....	60
Figure 4.17. Time evolutions of the spatially averaged powers of charged species versus pulse frequency 45~85kHz.....	61
Figure 4.18. The averaged quantities (a) charged species densities, (b) excited species densities, and (c) charged species powers versus pulse frequency 45~85kHz.....	62
Figure 4.19. Time evolutions of the spatially averaged densities of charged species versus gas pressure 90~120Torr.	63
Figure 4.20. Time evolutions of the spatially averaged densities of excited species versus gas pressure 90~120Torr.	64
Figure 4.21. Time evolutions of the spatially averaged powers of charged species versus gas pressure 90~120Torr.	65
Figure 4.22. The averaged quantities (a) charged species densities, (b) excited species densities, and (c) charged species powers versus gas pressure 90~120 Torr.	66
Figure 4.23. Time evolutions of the spatially averaged densities of charged species versus duty ratio 25~75%.	67
Figure 4.24. Time evolutions of the spatially averaged densities of excited species versus duty ratio 25~75%.	68

Figure 4.25. Time evolutions of the spatially averaged powers of charged species versus duty ratio 25~75%.	69
Figure 4.26. The averaged quantities (a) charged species densities, (b) excited species densities, and (c) charged species powers versus duty ratio 25~75%.	70
Figure 4.27. Time evolutions of the spatially averaged densities of charged species versus dielectric thickness 200~700 μm	71
Figure 4.28. Time evolutions of the spatially averaged densities of excited species versus dielectric thickness 200~700 μm	72
Figure 4.29. Time evolutions of the spatially averaged powers of charged species versus dielectric thickness 200~700 μm	73
Figure 4.30. Cycle averaged densities of charged species, e^- , Xe^+ , and Xe_2^+ versus dielectric thickness 200~700 μm	74
Figure 4.31. Cycle averaged densities of excited species, $\text{Xe}^*(^3\text{P}_1)$, $\text{Xe}^*(^3\text{P}_2)$, and Xe^{**} versus dielectric thickness 200~700 μm	75
Figure 4.32. Cycle averaged densities of excited species, $\text{Xe}^*(\text{O}_u^+)$, $\text{Xe}^*(^1\Sigma_u^+)$, and $\text{Xe}^*(^3\Sigma_u^+)$ versus dielectric thickness 200~700 μm	76
Figure 4.33. Cycle averaged powers of charged species, e^- , Xe^+ , and Xe_2^+ versus dielectric thickness 200~700 μm	77
Figure 4.34. The averaged quantities (a) charged species densities, (b) excited species densities, and (c) charged species powers versus dielectric thickness 200~700 μm	78

Symbols

A	area
A_{eff}	effective area
$A_{jk;lm}$	radiation transport matrix
d_{eff}	effective plasma size
D	diffusion constant
D_{die}	dielectric thickness
E	electric field
e	unsigned charge on an electron
f	pulse frequency
$f(\nu)$	Maxwellian velocity distribution
$g(\nu)$	line shape
g_1, g_2	degeneracy of lower and upper states respectively
$G(\mathbf{r}, \mathbf{r}')$	kernel function
h_L	center to axial edge density ratio
h_R	center to radial edge density ratio
K	rate coefficient for an electron impact collision
K_{el}	elastic scattering rate coefficient
K_{ex}	rate coefficient for excited state
K_{iz}	ionization rate coefficient
$k(\nu)$	absorption coefficient
k_0	peak absorption coefficient
L	length
l	cell length
l_E	protruded electrode length
m_e	electron mass
N	filled gas
$n^*(\mathbf{r}, t)$	resonant state density

N_x, N_y	number of cells in x and y direction
n_{lm}^*	constant density at the $(l, m)_{th}$ cell
n_0	plasma charged particles density
n_s	ion density at the plasma sheath edge
n_{sL}	the axial sheath density
n_{sR}	the radial sheath density
P	filled gas pressure
$P(\mathbf{r}, t)$	effective production rate
P_{abs}	power absorbed by the system
P_{ew}	electron energy loss to the walls
P_{ev}	electron energy loss due to all electron–neutral collision processes
P_{iw}	ion energy loss to the walls
R	radius
r	the position
r_d	duty ratio
r_{jk}	center position of the $(j, k)_{th}$ cell
S	source term
T	gas temperature
T_e	electron temperature
$T(\mathbf{r}, \mathbf{r}')$	probability of a resonance quantum traversing a distance R
T_{on}, T_{off}	periods of ‘on state’ and ‘off state’ of the pulse voltage
u_B	the Bohm velocity
V_{amp}	applied pulse voltage amplitude
V_s	sheath potential
w	cell width
w_E	protruded electrode width
w_g	electrode gap width
ν_0	frequency at the line center
σ	collision cross section



ε	permittivity
E	kinetic energy
E_c	collisional energy loss per electron–ion pair
E_e	mean kinetic energy lost per electron lost
E_{el}	mean energy lost per electron for a polarization scattering
E_{ex}	electron energy loss due to ionization
E_i	mean kinetic energy lost per ion lost
E_{iz}	ionization energy
E_T	total electron energy lost per ion lost
Γ	flux
$\Gamma(\mathbf{r}, t)$	resonant state particle flux
τ_v	vacuum radiative decay time
λ_0	wavelength at the line center
$\Delta\nu^L$	line width
Δt	time step
Δx	the distance between mesh points
μ	mobility
v	electron velocity
ϕ	electric potential



Chapter 1

Introduction

1.1. Motivation

The backlight module is one of the key parts of the liquid crystal display panel. The liquid crystal does not luminance, so the function of the backlight is to supply the sufficient brightness and uniform distribution light sources, to enable it to show the image normally. The TFT-LCD panel generally uses the cold cathode fluorescent lamp (Figure 1.1) as the backlight source, because of the advantage of long-lived and high luminous efficiency. It is suitable for the light source of the backlight module at present. The biggest drawbacks are: cold weather will reduce the light output by as much as 60%, they require an inverter to generate the 350VAC. The inverters do not function well at low temperatures, the light intensity cannot be varied, and vibration can reduce the life expectancy of up to 50%.

Recently, the environmental problem has been received considerable attention. It has become a serious issue. So, the mercury in fluorescent lamps should be eliminated. A mercury-free flat discharge fluorescent lamp has been developed for LCD backlighting. Table 1 summarized the advantages and disadvantages of CCFLs, LEDs, OLED, and plasma backlight as the LCD backlights [Kim, 2005]. Because plasma backlight has the advantages of extremely long service life, constant brightness over wide temperature range, instant light output, and mercury-free, we attempt to develop a two-dimensional fluid modeling code for plasma backlight module of TFT-LCD panel to find out the discharge phenomenon of a plasma backlight cell. Expect to improve the luminous efficiency and reduce the power consumption effectively by the simulation results.

Table 1. Comparison of LCD backlight options

Backlight requirement	CCFL	LED	OLED	Plasma backlight
High brightness/ good uniformity of brightness	Yes	Bright, but difficulty matching color of LEDs	Yes, although high brightness limits lifetime	Yes
Low power	Yes, but high voltage (1.5 kV to strike, 500 V to maintain plasma)	Efficiency need improvement, but low voltage	Efficiency need improvement, but low voltage	Efficiency need improvement, but low voltage
Long life	Yes- 50,000+ hours	Yes- 70,000+ hours	Not yet-materials limited to about 15,000 hours	Yes- 100,000+ hours
Temperature insensitivity	No- trouble at low T (Hg vapor pressure)	Yes	No- trouble at high T	Yes
Low cost	Yes- mature technology	Potentially low, but needs to improvement	Potentially low, but needs improvement	Potentially low, but needs improvement
Additional benefits		Mercury-free	Mercury-free, area light source	Mercury-free, area light source

1.2. Background

1.2.1. Numerical Models in Low-temperature Plasma Physics

Numerical modeling of plasmas is a valuable tool for understanding the physics involved in low-temperature discharges and optimizing plasma sources. The model used to simulate a certain plasma system, however, should be selected based on the plasma conditions that are expected to be encountered.

A brief introduction of the fluid, PIC-MCC and the hybrid models is presented. These are the models commonly used to simulate low- temperature plasmas.

1.2.1.1. Fluid Modeling

Fluid models describe the plasma based on the density, mean velocity and mean energy of the constituent species [Chen and Raja, 2004]. The values of these macroscopic quantities are obtained by solving the continuity, the flux and the energy equations for each species in the plasma. These fluid equations are obtained by taking velocity moments of the Boltzmann equation [Makabe, 2002]. Maxwell equations (or Poisson's equation in electrostatic

simulations) are coupled with fluid equations to obtain self-consistent electric/magnetic fields.

1.2.1.2. Particle Modeling (Particle-In-Cell Method)

Particle models are time and spatially dependent solutions of the Boltzmann equation which produces electron and ion velocity distributions either by direct integration of the equation or by applying statistical techniques. A typical flow diagram of PIC simulation is shown in Figure 1.2 [Kim et al, 2005].

The major limitation of PIC-MCC simulations is the computation time. This is proportional to the number of super-particles and it is therefore desirable to keep the number of super-particles as low as possible.

1.2.1.3. Hybrid Modeling

Hybrid models are a combination of fluid and PIC models [Kratzer et al, 2001]. Hybrid models have been developed in order to simulate rather complex chemistries of gas discharges. The transport coefficients and the rate of reactions of electrons with molecules are derived kinetically, while the density of species and the time and space variation of the electric field are calculated using the fluid flow approach. The end result is that hybrid codes run faster than PIC codes yet are slower than pure fluid codes, and describe some kinetics more precisely than fluid models.

1.2.2. The Plasma Backlight Technology

The plasma backlight technology has gained recognition as a backlight source for industrial and medical display applications [Fiegler et al, 2003] as well as for the LCD-TV consumer market, and has been described in server publications. At present, several display manufactures are involved in the development of plasma backlight source.

Figure 1.3 schematically depicts a plasma backlight unit. It is a mercury-free flat fluorescent lamp system. The discharge space filled with Xenon gas is sandwiched between two glass plates. The top glass is spread with phosphor, and the parallel electrodes covered with dielectric are on the bottom glass. The dielectric layer preserves the electrodes and slows the rate of wear on them, increasing lamp life.

The cathodes are the point-like tips and the anodes are the continuous lines (Figure 1.4). When the pulse voltage is applied between the electrodes, the discharge occurring between each electrode pair is triangular in shape (Figure 1.5). The cathodes exhibit arrays of perpendicular extensions to locally increase the electric field between the electrodes by shortening the distance between the anodes and cathodes.

The system generates light using pulsed voltages (Figure 1.6). The suitable voltage is applied to the electrode system of the lamp from outside. It excites Xenon atoms in the discharge space and enables the formation of the excited Xe_2^* molecules that produces UV radiation at 173 nm. Table 2 lists the important reactions and rate constants in Xe that have been used in this simulation [Eckstrom et al, 1988; Lo et al, 2005].

Table 2. The important reactions for discharge in Xe gas

Reaction	Threshold energy (eV)	Reaction rate
<u>Ionization by electron</u>		
$e^- + Xe \rightarrow Xe^+ + 2e^-$	12.12	EEDF
<u>Stepwise ionization</u>		
$e^- + Xe(^3P_1) \rightarrow Xe^+ + 2e^-$	3.68	EEDF
$e^- + Xe(^3P_2) \rightarrow Xe^+ + 2e^-$	3.8	EEDF
$e^- + Xe^{**} \rightarrow Xe^+ + 2e^-$	2.54	$1.56 \times 10^{-7} T_e^{-0.71} \times e^{\frac{2.63}{T_e}} cm^3 s^{-1}$
<u>Excited</u>		
$e^- + Xe \rightarrow Xe(^3P_1) + e^-$	8.44	EEDF
$e^- + Xe \rightarrow Xe(^3P_2) + e^-$	8.32	EEDF
$e^- + Xe \rightarrow Xe^{**} + e^-$	9.58	EEDF
$e^- + Xe_2(^3\Sigma_u^+) \rightarrow e^- + Xe_2(^1\Sigma_u^+)$	0.06	EEDF
$e^- + Xe_2(^3\Sigma_u^+) \rightarrow e^- + Xe(^3P_2) + Xe$	1.12	EEDF

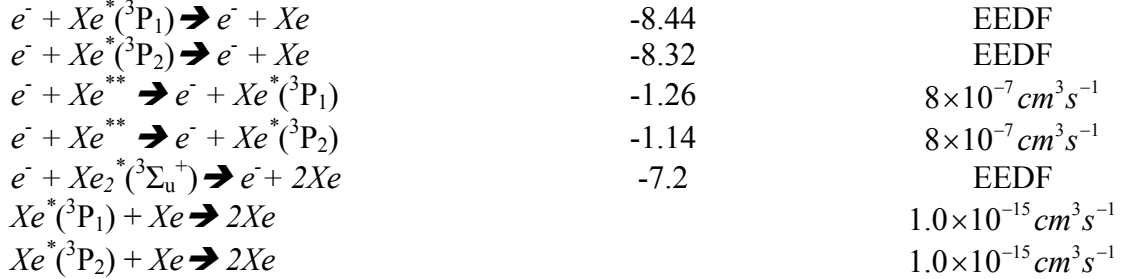
Ion conversion



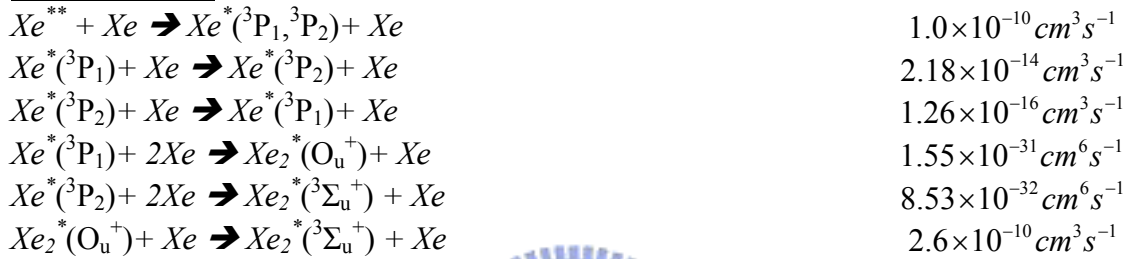
Recombination



De-excitation



Neutral kinetics



Spontaneous decay

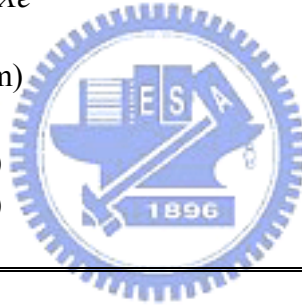


Figure 1.7 is an energy level diagram of these processes. The UV photons are emitted by the plasma and transformed into visible photons by phosphors, deposited on the glass plates. Owing to the absence of mercury the degeneration of the phosphor is slowed, the lamp reaches full light output almost immediately, panel luminance remains constant from -30°C to $+85^\circ\text{C}$, and disposal is simple.

1.3. Literature Survey

Plasma backlight is one type of dielectric barrier discharges arrangement originally used by Werner Siemens in 1857. A number of computational studies have been previously investigated the dielectric barrier discharges. DBDs have long been used for ozone syntheses

and are now being investigated for as excimer ultraviolet (UV) radiation sources [Falkenstein and Coogan 1997; Zhang and Boyd 1998]. To investigate the discharge in DBDs, zero-dimensional, one-dimensional, two-dimensional, and three-dimensional models have been developed. Shiga et al used a zero-dimensional positive column model to study the efficacy in a Hg-free discharge fluorescent lamp for application in LCD backlighting [Shiga et al 2003]. In the positive column, the efficiency of generation of VUV radiation depends on the mean electron energy influenced by discharge current.

A self-consistent one-dimensional model is applied to the study of a single DBD dynamic for power frequencies from 50 kHz to 1 MHz and gas pressures from 10 to 400 Torr [Oda et al 1999]. The present result suggested that the efficiencies of vacuum ultra-violet radiation from $\text{Xe}_2^*(^1\Sigma_u^+)$ and $\text{Xe}_2^*(^3\Sigma_u^+)$ are independent of the power source frequency. [Oda et al 2000] used the pulse voltages with trapezoidal and sinusoidal waveforms to simulate the Xe dielectric barrier discharges at different gap lengths. The higher light output power and efficiency are obtained in the narrower discharge gap in a certain input power range.

The dielectric barrier discharge Xenon excimer lamps have been simulated using two-dimensional fluid model [Akashi et al 2005]. The filamentary discharge was obtained fuzzy and the number of the filaments decreases while the secondary electron emission increases. Brauer et al used a model based on the solutions of electron and ion transport equations coupled with Poisson's equation in a 2D Cartesian geometry to simulate the self-organized filaments in a dielectric barrier glow discharge plasma. 2D and 3D fluid and kinetic models simulations of plasma display panel were presented [Yang et al 2004]. The simulation results show similar characteristics compared with experimentally measured data.

1.4. The Scope of this Thesis

The main purpose of this thesis is to obtain of a two-dimensional fluid model to help

understand the behavior of the plasma backlight source, and the model can be used as a tool for optimizing the micro-discharge operating conditions, geometry, and gas composition.

Chapter 2 presents the numerical methods that can be used for the simulation of plasma backlight. It discusses the basis of the global and fluid models. We use the models to investigate the discharge phenomena. Chapter 3 provides all the details of the parameters used in this simulation. In the Chapter 4, we present the results of global and fluid modeling studies of plasma backlight discharge, respectively. The modeling results presented in this chapter will help us understand the mechanism of discharge of plasma backlight.

There are large numbers of variables in discharge experiments, so numerical simulation is a good useful tool for understanding the discharge mechanism and designing new cell structure.

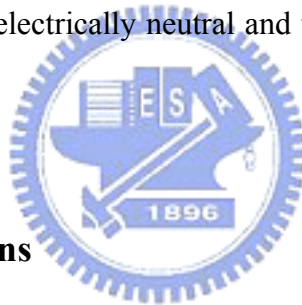


Chapter 2

Numerical Methods

2.1. Global Model

The Global model was developed by Lieberman and Gottscho in 1994. It is based on the steady state model for a cylindrical plasma discharge of radius R and length L . The model assumes uniform spatial distribution of plasma parameters over the volume of bulk plasma, with the plasma density n_e in the bulk dropping sharply to edge values n_{sL} and n_{sR} at the thin sheaths close to the axial and circumferential walls. Electron-ion pairs are assumed to be created by electron-impact ionization of background gas and are lost by diffusive flow to the walls. The plasma is assumed electrically neutral and that the ion and electron fluxes toward the walls balance at all time.



2.1.1. Modeling Equations

Two main sets of equations are used in the global model: power balance and particle balance for all species of interest. For a monatomic gas, the equations are straightforward, as discussed by Lieberman and Gottscho.

The electron temperature (T_e , in units of eV) is simply a function of the pressure and geometry of the system, the plasma density is proportional to the input power, and the collisional energy loss per electron-ion pair created (E_c , in units of eV) is a function of T_e only. For molecular gases, the situation is more complicated. As we will see, the plasma composition, i.e., ion and neutral densities, plays an important role in determining the electron temperature and E_c .

The total power balance has the general form of

$$P_{abs} = P_{ev} + P_{iw} + P_{ew} \quad (1)$$

where P_{abs} is the power absorbed by the system, P_{ev} is the electron energy loss due to all electron–neutral collision processes in the volume, P_{iw} is the ion energy loss to the walls, and P_{ew} is the electron energy loss to the walls.

The total surface particle loss to the total volume ionization,

$$n_0 u_B (2\pi R^2 h_L + 2\pi R L h_R) = K_{iz} n_g n_0 \pi R^2 L \quad (2)$$

2.1.2. Derivation of Rate Constants

The rate coefficient for an electron impact collision is obtained by integrating the cross sections over an assumed Maxwellian distribution

$$K = \langle \sigma(v) v \rangle_v = 4\pi \int_0^\infty \sigma(v) v^3 f(v) dv \quad (3)$$

where σ is the collision cross section, v is the electron velocity and

$$f(v) = \left(\frac{m_e}{2\pi k T_e} \right)^{3/2} \exp\left(-\frac{m_e v^2}{2k T_e} \right) \quad (4)$$

is the Maxwellian velocity distribution, m_e is the electron mass, e is the electron charge and T_e is the electron temperature. Using the relationship for the velocity and kinetic energy of a particle,

$$\mathbf{E} = \frac{m_e v^2}{2} \quad (5)$$

$$v = \sqrt{\frac{2\mathbf{E}}{m_e}} \quad (6)$$

$$dv = \left(\frac{2\mathbf{E}}{m_e} \right)^{-1/2} \frac{d\mathbf{E}}{m_e} \quad (7)$$

we find

$$f(\mathbf{E}) = \left(\frac{m_e}{2\pi kT}\right)^{3/2} \exp\left(-\frac{\mathbf{E}}{kT}\right) 4\pi \left(\sqrt{\frac{2\mathbf{E}}{m_e}}\right)^2 \quad (8)$$

$$f(\mathbf{E}) = \left(\frac{m_e}{2\pi kT}\right)^{3/2} \exp\left(-\frac{\mathbf{E}}{kT}\right) 4\pi \frac{2\mathbf{E}}{m_e} \quad (9)$$

to be the normalized Maxwellian energy distribution. Thus

$$K = \int_0^\infty \sigma(\mathbf{E}) \left(\sqrt{\frac{2\mathbf{E}}{m_e}}\right) \left(\frac{m_e}{2\pi kT}\right)^{3/2} \exp\left(-\frac{\mathbf{E}}{kT}\right) 4\pi \frac{2\mathbf{E}}{m_e} \left(\frac{2\mathbf{E}}{m_e}\right)^{-1/2} \frac{d\mathbf{E}}{m_e} \quad (10)$$

$$K = \int_0^\infty \sigma(\mathbf{E}) \left(\frac{8kT}{\pi m_e}\right)^{1/2} \frac{\mathbf{E}}{kT} \exp\left(-\frac{\mathbf{E}}{kT}\right) \frac{d\mathbf{E}}{kT} \quad (11)$$

is the rate coefficient.

2.1.3. Solution Procedures

The most important rate constants for electron collisions are K_{iz} , K_{ex} , K_{el} for electron-neutral ionization, excitation and momentum transfer. There are given as a function of electron temperature. The collisional energy loss per electron-ion pair created, $\mathbf{E}_c(T_e)$, which is defined as

$$K_{iz} \mathbf{E}_c = K_{iz} \mathbf{E}_{iz} + K_{ex} \mathbf{E}_{ex} + K_{el} \mathbf{E}_{el} \quad (12)$$

Where \mathbf{E}_{iz} is the ionization energy, K_{iz} is the ionization rate coefficient, K_{ex} is the rate coefficient for excited state and K_{el} is the elastic scattering rate coefficient. The terms of the RHS account for the loss of electron energy due to ionization, excitation, and elastic (polarization) scattering against neutral atoms. The quantity $\mathbf{E}_{el} \square (3m/M)T_e$ is the mean energy lost per electron for a polarization scattering. \mathbf{E}_c is a function of T_e only, depending on the electron-neutral species collisional energy loss process in the gas.

The total electron energy lost per ion lost from the system:

$$\mathbf{E}_T = \mathbf{E}_c + \mathbf{E}_e + \mathbf{E}_i \quad (13)$$

The quantity $\mathbf{E}_e \approx 2T_e$ is the mean kinetic energy lost per electron lost. \mathbf{E}_i represents the mean kinetic energy lost per ion when it bombards a wall surface. It is the sum of the ion energy entering the sheath and the energy gained as it traverse the sheath.

At pressures for which the ion loss velocity is the Bohm velocity u_B , the overall discharge power balance for a cylindrical plasma having radius R and length L can be written in terms of \mathbf{E}_T as

$$P_{abs} = en_s u_B A \mathbf{E}_T \quad (14)$$

where P_{abs} is the power absorbed by plasma, n_s is the ion density at the plasma sheath edge, and A is the area for particle loss. The Bohm velocity is relatively constant for a given ion mass and for the typical limited range of T_e 's of 2-5 V. Hence n_s is controlled by \mathbf{E}_T , A , and P_{abs} .

Godyak and Maximov have given heuristic equations for the axial sheath density n_{sL} and for the radial sheath density n_{sR} in the terms of dimensionless quantities h_L and h_R define as

$$h_L = \frac{n_{sL}}{n_e} \approx 0.86 \left(3.0 + \frac{L}{2\lambda_i} \right)^{-1/2} \quad (15)$$

at the axial sheath edge and

$$h_R = \frac{n_{sR}}{n_e} \approx 0.80 \left(4.0 + \frac{R}{\lambda_i} \right)^{-1/2} \quad (16)$$

at the radial sheath edge, assuming cylindrical reactor geometry having a radius R and length L .

We consider a simple cylindrical discharge model to estimate the plasma parameters and their variation with power, pressure, and source geometry. The electron temperature T_e , the

ion-bombarding energy \mathbf{E}_i , and the plasma density n_0 are the most significant quantities for plasma processing applications.

We first determine T_e by equating the total surface particle loss to the total volume ionization. Introducing an effective plasma size d_{eff} ,

$$d_{eff} = \frac{1}{2} \frac{RL}{Rh_L + Lh_R} \quad (17)$$

the particle balance equation can be written as :

$$\frac{K_{iz}(T_e)}{u_B(T_e)} = \frac{1}{n_g d_{eff}} \quad (18)$$

Using these parameters, T_e can be deduced as a function of neutral gas pressure and geometry of the system solely. The ion-bombarding energy \mathbf{E}_i is the sum of the ion energy entering the sheath and the energy gained by the ion as traverse the sheath. The potential over the sheath is taken to be equal to

$$V_s = \frac{T_e}{2} \ln\left(\frac{M}{2\pi m}\right) \quad (19)$$

The ion kinetic energy lost at a surface is then

$$\mathbf{E}_i = V_s + \frac{1}{2} T_e \quad (20)$$

Finally, we estimate the plasma charged particles density n_0 is proportional to the power dissipated by the discharge electrons according to

$$n_0 = \frac{P_{abs}}{eu_B A_{eff} \mathbf{E}_T} \quad (21)$$

where A_{eff} is an effective area defined by

$$A_{eff} = 2\pi R(Rh_L + Lh_R) \quad (22)$$

2.2. Fluid Model

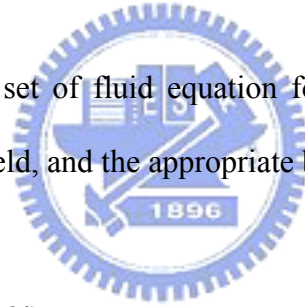
In fluid models the charged particle properties are characterized by macroscopic quantities such as density, mean velocity, and mean energy that are solutions of the first three moments of the Boltzmann equation in velocity space. Only two moments are used to describe electron and ion transport: continuity equations, and simplified momentum transfer equation, in the drift-diffusion approximation. The system is closed by assuming that the charged particle mobility and ionization and excitation coefficients depend only on the local reduced electric field ($\mathbf{E}(x,t) / N$ or $\mathbf{E}(x,t) / P$).

$E(x,t)$: electric field

N : filled gas

P : filled gas pressure

The model consists of a set of fluid equations for electron, ions, and excited species, Poisson equation for electric field, and the appropriate boundary conditions.



2.2.1. Modeling Equations

2.2.1.1. Continuity Equation

The governing equations for a plasma fluid model are based on Maxwell's equations coupled with moments of the Boltzmann equations describing the transport of the ion and electron component. For every plasma particle species, the time evolution of the density is described by a continuity equation

$$\frac{\partial n_\ell}{\partial t} + \nabla \cdot \Gamma_\ell = S_\ell \quad (23)$$

where n_ℓ , Γ_ℓ , and S_ℓ are the number density, flux, and source term including the creation and the destruction reaction of species ℓ , respectively.

The creations of electrons and ions include the ionization, step ionization, and Penning

ionization. We use the local field approximation (LFA) method to calculate the electron-driven rate coefficients. The LFA assumes that the electron energy distribution function at a given location and in time depends on $\mathbf{E}(x,t) / N$ or $\mathbf{E}(x,t) / P$ at this location. This is equivalent to assuming that the electron energy gain due to the field at a given location and time is exactly balanced by the collision loss at the same location and time. The model overestimates the rate in the sheath region near the peak of discharge because the electrons don't accomplish equilibrium with the field in high electric field region.

2.2.1.2. Momentum Equation with Drift-Diffusion Approximation

For the time scales of interest, the electrons are inertia-free, eliminating the electron momentum transfer equation, allowing invoking the drift-diffusion approximation. The flux is given by the momentum balance equation. Simplified momentum equation is followed.

$$\Gamma_p = -D_p \nabla n_p + \mu_p n_p E \quad (24)$$

$$\Gamma_e = -D_e \nabla n_e + \mu_e n_e E \quad (25)$$

$$\Gamma_{ex} = -D_{ex} \nabla n_{ex} \quad (26)$$

μ : mobility for charged particles

D : diffusion constant

p : ion

e : electron

ex : excited species

2.2.1.3. Poisson's Equation for Electrostatic Potential

The self-consistent treatment of the charged particle transport is ensured by coupling the above set of equations with Poisson's equation. The electric field profile is calculated by

solving Poisson's equation. The quantities obtained from Eqs. (23) and (24) are coupled with Poisson equation,

$$\nabla \cdot (\varepsilon \nabla \phi) = -\sum q_\ell n_\ell - \sigma \quad (27)$$

ε : permittivity

ϕ : electrical potential

σ : surface charge density on the dielectric surface

Integrating in time the electron and ion current densities arriving at the dielectric surface obtain the charge density σ on the dielectric surface.

2.2.1.4. Radiation Transport Equation

The model includes 6 excited states of Xe [i.e. Xe*(³P₁), Xe*(³P₂), Xe₂*(O_u⁺) Xe₂*(¹Σ_u⁺), Xe₂*(³Σ_u⁺), Xe**], and emission spectra from the radiative excited states (i.e. 147 nm, 150 nm, 173 nm, 828 nm). Collision between neutral species and Penning ionization included as well the electron impact ionizations and excitations.

The governing equation of the resonant state density is the modified Holstein equation [Holstein, 1947 and 1951],

$$\frac{\partial n^*(\mathbf{r}, t)}{\partial t} + \nabla \cdot \mathbf{\Gamma}(\mathbf{r}, t) = P(\mathbf{r}, t) - \frac{1}{\tau_v} n^*(\mathbf{r}, t) + \frac{1}{\tau_v} \int n^*(\mathbf{r}', t) G(\mathbf{r}, \mathbf{r}') d\mathbf{r}' \quad (28)$$

Here, $n^*(\mathbf{r}, t)$ is the resonant state density, $\mathbf{\Gamma}(\mathbf{r}, t)$ is the resonant state particle flux, and τ_v is the vacuum radiative decay time. $P(\mathbf{r}, t)$ is the effective production rate which includes the production rate by electron impact excitation, the depopulation of the excited states by step ionization, diffusion, and other collisions. The kernel function, $G(\mathbf{r}, \mathbf{r}')$, is the probability of radiation emitted at the position \mathbf{r}' being absorbed at the position \mathbf{r} . It is given by the expression,

$$G(\mathbf{r}, \mathbf{r}') = -\frac{\mathbf{R}}{4\pi R^3} \cdot \nabla_r T(\mathbf{r}, \mathbf{r}') \quad (29)$$

where $\mathbf{R} = \mathbf{r} - \mathbf{r}'$ and $R = |\mathbf{R}|$. $T(\mathbf{r}, \mathbf{r}')$ is the probability of a resonance quantum traversing a distance R without being absorbed.

For uniform ground state density, the transmission factor depends only on the distance between two positions \mathbf{r} and \mathbf{r}' , and therefore it is shift invariant and isotropic in Cartesian coordinate.

$$T(\mathbf{r}, \mathbf{r}') = T(R) = \int_0^\infty g(\nu) \exp[-k(\nu)R] d\nu \quad (30)$$

$$g(\nu): \text{lineshape} \quad g(\nu) = \frac{\Delta\nu^L/2\pi}{(\nu - \nu_0)^2 + (\Delta\nu^L/2)^2}$$

$$k(\nu): \text{absorption coefficient} \quad k(\nu) = \frac{\lambda_0^2}{8\pi\tau_\nu} \frac{g_2}{g_1} n_{Xe} g(\nu)$$

λ_0 : wavelength at the line center

g_1, g_2 : degeneracies of lower and upper states respectively

ν_0 : frequency at the line center

$\Delta\nu^L$: line width defined as the FWHM of the lineshape

The peak absorption coefficient k_0 at the line center is defined as

$$k_0 = \frac{\lambda_0^2}{8\pi\tau_\nu} \frac{g_2}{g_1} \frac{2}{\pi\Delta\nu^L} n_{Xe} \quad (31)$$

2.2.2. Discretization of Modeling Equations

2.2.2.1. Continuity Equation with Drift-Diffusion Approximation

As the gas pressure in the plasma backlight cells is usually high (~ 100 Torr), it was not found necessary to solve the conservation momentum equation per se. We instead used the drift-diffusion approximation, which considerably reduces the simulation time. The simulation geometry for two-dimensional plasma backlight cell is shown in Figure 2.1. We

calculate the electron density at the center of cell and potential at the grid point.

In order to calculate the density implicitly, we have to substitute a discretized expression for the drift-diffusion flux. We employ the Scharfetter-Gummel exponential [Scharfetter and Gummel, 1969] representation of the charged particle fluxes. The scheme supports large density gradients.

A standard different scheme of Eq. (25) would be lead to numerical instability whenever the voltage difference between grid point is of the order or larger than the characteristic energy D/μ . The basic idea of the Scharfetter-Gummel method is to assume that the flux is constant between half grid points and is calculated at the grid point. Flux is interpolated with adjacent two half-grid points shown in Figure 2.2. Consider one direction (X-direction). Integration is followed:

$$\begin{aligned}
 \Gamma_{m+\frac{1}{2}} &= (\text{sign}) \mu_m n_m E_m - \frac{\partial}{\partial x} n_m D_m \\
 &= n_m D_m \frac{z_{m+\frac{1}{2}}}{\Delta x} - \frac{\partial}{\partial x} n_m D_m \\
 \frac{\partial}{\partial x} n_m D_m &= n_m D_m \frac{z_{m+\frac{1}{2}}}{\Delta x} - \Gamma_{m+\frac{1}{2}}
 \end{aligned} \tag{32}$$

(sign): signature denoting 0 (neutral species), -1 (electron), and 1 (ions)

then analytic integration between m and $m+1$ lead to

$$\frac{\frac{1}{\Delta x} z_{m+\frac{1}{2}} n_{m+1} D_{m+1} - \Gamma_{m+\frac{1}{2}}}{\frac{1}{\Delta x} z_{m+\frac{1}{2}} n_m D_m - \Gamma_{m+\frac{1}{2}}} = e^{z_{m+\frac{1}{2}}} \tag{33}$$

where $x \rightarrow m$, $x + \Delta x \rightarrow m+1$, $z_{m+\frac{1}{2}} = -\frac{(\text{sign}) \mu_{m+\frac{1}{2}}}{D_{m+\frac{1}{2}}} (\phi_{m+1} - \phi_m)$

$$\Gamma_{m+\frac{1}{2}} = \frac{z_{m+\frac{1}{2}} n_m D_m e^{\frac{z_{m+\frac{1}{2}}}{2}} - n_{m+1} D_{m+1}}{e^{\frac{z_{m+\frac{1}{2}}}{2}} - 1} \tag{34}$$

$$= \alpha_m n_m - \beta_m n_m \quad (35)$$

$$\alpha_m = \frac{z^{m+\frac{1}{2}}}{\Delta x} \frac{D_m}{e^{\frac{z}{m+\frac{1}{2}} - 1}} e^{\frac{z}{m+\frac{1}{2}}}$$

$$\beta_m = \frac{z^{m+\frac{1}{2}}}{\Delta x} \frac{D_{m+1}}{e^{\frac{z}{m+\frac{1}{2}} - 1}}$$

$m + \frac{1}{2}$: mesh point located at grid point.

Δx : the distance between mesh points.

The continuity equation is discriminated as follow:

$$\frac{\tilde{n}_{m,n} - n_{m,n}^k}{\frac{\Delta t}{2}} + \frac{\tilde{\Gamma}_{m+1/2,n}^k - \tilde{\Gamma}_{m-1/2,n}^k}{\Delta x} = S_{m,n}^k - \frac{\Gamma_{m,n+1/2}^k - \Gamma_{m,n-1/2}^k}{\Delta y} \quad (36)$$

$$\frac{n_{m,n}^{k+1} - \tilde{n}_{m,n}^k}{\frac{\Delta t}{2}} + \frac{\Gamma_{m,n+1/2}^{k+1} - \Gamma_{m,n-1/2}^{k+1}}{\Delta y} = S_{m,n}^k - \frac{\tilde{\Gamma}_{m+1/2,n}^k - \tilde{\Gamma}_{m-1/2,n}^k}{\Delta x} \quad (37)$$

We use the Alternating Direction Implicit (ADI) method [Reale, 1995] to integrate the continuity equation. Two time steps are used in two dimensions to update the quantities between t and $t + \Delta t$. The continuity equation in X direction is replaced with Eq. (34) as follow,

$$A_{m,n} \tilde{n}_{m-1,n}^{\tilde{k}+1} + B_{m,n} \tilde{n}_{m,n}^{\tilde{k}+1} + C_{m,n} \tilde{n}_{m+1,n}^{\tilde{k}+1} = D_{m,n}^{\tilde{k}} \quad (38)$$

$$A_{m,n} = -\frac{\Delta t}{2\Delta x^2} \frac{z^{m-\frac{1}{2},n} D_{m-1,n}}{e^{\frac{z}{m-\frac{1}{2},n} - 1}} e^{\frac{z}{m-\frac{1}{2},n}}$$

$$B_{m,n} = 1 + \frac{\Delta t}{2\Delta x^2} D_{m,n} \left(\frac{z^{m+\frac{1}{2},n}}{e^{\frac{z}{m+\frac{1}{2},n} - 1}} e^{\frac{z}{m+\frac{1}{2},n}} + \frac{z^{m-\frac{1}{2},n}}{e^{\frac{z}{m-\frac{1}{2},n} - 1}} \right)$$

$$C_{m,n} = -\frac{\Delta t}{2\Delta x^2} \frac{z^{m+\frac{1}{2},n} D_{m+1,n}}{e^{\frac{z}{m+\frac{1}{2},n} - 1}} e^{\frac{z}{m+\frac{1}{2},n}}$$

$$D_{m,n} = n_{m,n}^k + \frac{\Delta t}{2} S_{m,n}^k + \frac{\Delta t}{\Delta y} (\Gamma_{m,n+1/2}^k - \Gamma_{m,n-1/2}^k)$$

The left side of Eq. (38) is calculated at time $t^{\tilde{k}+\tilde{1}}$ and the right side is obtained from present time t^k . The two adjacent grid points ($m+1$ and $m-1$) are needed to update the densities at the grid point m . Matrix representation of Eq. (38) forms a tridiagonal matrix that has non-zero value in diagonal and its adjacent two elements. The density $\tilde{n}_{m,n}^{\tilde{k}+\tilde{1}}$ can be obtained from the inversion of tridiagonal matrix. The update from $t^{\tilde{k}+\tilde{1}}$ to t^{k+1} is accomplished with Y direction integration similar to previous matrix solver.

2.2.2.2. Poisson's Equation

Poisson's equation is solved with a Successive Over-Relaxation (SOR) [Kinder and Kushner, 2001] method. The electric field is taken at time t when the continuity equations are integrated between t and $t + \Delta t$. The electric field in the integration of the continuity equation between t and $t + \Delta t$ is not the field at time t , but rather a prediction of the electric field at time $t + \Delta t$. The semi-implicit integration of Poisson's equation is followed as:

$$\nabla \cdot (\varepsilon \varepsilon_0 \nabla \phi) = -e(n_p - n_e) \quad (39)$$

$$\nabla \cdot (\varepsilon \nabla \phi^{k+1}) = -\frac{e}{\varepsilon_0} \left[(n_p^k - n_e^k) + \Delta t \frac{\partial (n_p - n_e)}{\partial t} \right] \quad (40)$$

The continuity equations and momentum transfer equations for ion and electron is shown

$$\begin{cases} \frac{\partial n_p}{\partial t} + \nabla \cdot (n_p \bar{v}_p) = S_p \\ \frac{\partial n_e}{\partial t} + \nabla \cdot (n_e \bar{v}_e) = S_e \\ n_p \bar{v}_p = -n_p \mu_p \nabla \phi - D_p \nabla n_p \\ n_e \bar{v}_e = n_e \mu_e \nabla \phi - D_e \nabla n_e \end{cases} \quad (41)$$

Continuity equations and momentum equations are coupled with Poisson's equation to obtain the quantities.

$$-\frac{e}{\varepsilon_0} \Delta t \frac{\partial(n_p - n_e)}{\partial t} = -\frac{e}{\varepsilon_0} \Delta t \nabla \cdot \left[(n_p^k \mu_p^k + n_e^k \mu_e^k) \nabla \phi^{k+1} - (D_e^k n_e^k + D_p^k n_p^k) \right]$$

$$\approx -\frac{e}{\varepsilon_0} \Delta t \nabla \cdot \left[\sum_l n_l^k \mu_l^k \nabla \phi^{k+1} \right]$$

$$\therefore \nabla \cdot (\varepsilon \nabla \phi^{k+1}) = -\frac{e}{\varepsilon_0} \sum_l (\text{sign}) n_l^k - \frac{e}{\varepsilon_0} \Delta t \nabla \cdot \left[\sum_l n_l^k \mu_l^k \nabla \phi^{k+1} \right] \quad (42)$$

$$\nabla \cdot \left[\left(\varepsilon + \frac{e}{\varepsilon_0} \Delta t \sum_l n_l^k \mu_l^k \right) \nabla \phi^{k+1} \right] = -\frac{e}{\varepsilon_0} \sum_l (\text{sign}) n_l^k \quad (43)$$

The Poisson's equation is discriminated x and y directions,

$$\frac{\partial}{\partial x} \left[\left(\varepsilon_x + \frac{e}{\varepsilon_0} \Delta t \sum_l n_{lx}^k \mu_{lx}^k \right) \nabla \phi_x^{k+1} \right] + \frac{\partial}{\partial y} \left[\left(\varepsilon_y + \frac{e}{\varepsilon_0} \Delta t \sum_l n_{ly}^k \mu_{ly}^k \right) \nabla \phi_y^{k+1} \right] = -\frac{e}{\varepsilon_0} \sum_l (\text{sign}) n_l^k \quad (44)$$

In x-direction:

$$\frac{\partial}{\partial x} \left[\left(\varepsilon_x + \frac{e}{\varepsilon_0} \Delta t \sum_\ell n_{\ell,x}^k \mu_{\ell,x}^k \right) \nabla \phi_x^{k+1} \right]$$

$$= \frac{1}{\Delta x} \left[\left(\varepsilon_{i+1/2,j} + \frac{e}{\varepsilon_0} \Delta t \sum_\ell n_{\ell,i+1/2,j} \mu_{\ell,i+1/2,j} \right) \nabla \phi_{i+1/2,j}^{k+1} - \left(\varepsilon_{i-1/2,j} + \frac{e}{\varepsilon_0} \Delta t \sum_\ell n_{\ell,i-1/2,j} \mu_{\ell,i-1/2,j} \right) \nabla \phi_{i-1/2,j}^{k+1} \right] \quad (45)$$

We define the dielectric constant ε , number n , and mobility μ at the center of cell in our code (Figure 2.3).

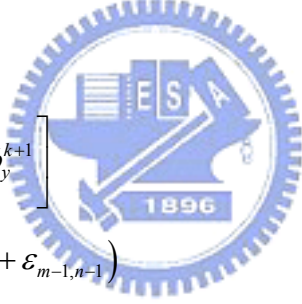
$$\varepsilon_{i+1/2,j} = \frac{\varepsilon_{m,n} + \varepsilon_{m,n-1}}{2}, n_{i+1/2,j} = \frac{n_{m,n} + n_{m,n-1}}{2}, \mu_{i+1/2,j} = \frac{\mu_{m,n} + \mu_{m,n-1}}{2}$$

For the calculation of the electric field, we make use of the electric potential and substitute the difference. ϕ is defined at the grid point.

$$E_{i+1/2,j} = \nabla \phi_{i+1/2,j} = \frac{\phi_{i+1,j} - \phi_{i,j}}{\Delta x}$$

$$\begin{aligned}
& \frac{\partial}{\partial x} \left[\left(\varepsilon_x + \frac{e}{\varepsilon_0} \Delta t \sum_{\ell} n_{\ell,x}^k \mu_{\ell,x}^k \right) \nabla \phi_x^{k+1} \right] \\
&= \frac{1}{\Delta x} \left[\left(\frac{\varepsilon_{m,n} + \varepsilon_{m,n-1}}{2} + \frac{e}{\varepsilon_0} \Delta t \sum_{\ell} \frac{n_{m,n} + n_{m,n-1}}{2} \frac{\mu_{m,n} + \mu_{m,n-1}}{2} \right) \frac{\phi_{i+1,j}^{k+1} - \phi_{i,j}^{k+1}}{\Delta x} \right. \\
&\quad \left. - \left(\frac{\varepsilon_{m-1,n} + \varepsilon_{m-1,n-1}}{2} + \frac{e}{\varepsilon_0} \Delta t \sum_{\ell} \frac{n_{m-1,n} + n_{m-1,n-1}}{2} \frac{\mu_{m-1,n} + \mu_{m-1,n-1}}{2} \right) \frac{\phi_{i,j}^{k+1} - \phi_{i-1,j}^{k+1}}{\Delta x} \right] \\
&= -\frac{1}{2\Delta x^2} \left\{ (\varepsilon_{m,n} + \varepsilon_{m,n-1} + \varepsilon_{m-1,n} + \varepsilon_{m-1,n-1}) \right. \\
&\quad \left. + \frac{e}{2\varepsilon_0} \Delta t \sum_{\ell} \left[(n_{m,n} + n_{m,n-1})(\mu_{m,n} + \mu_{m,n-1}) + (n_{m-1,n} + n_{m-1,n-1})(\mu_{m-1,n} + \mu_{m-1,n-1}) \right] \right\} \phi_{i,j} \\
&\quad + \frac{1}{2\Delta x^2} \left\{ (\varepsilon_{m,n} + \varepsilon_{m,n-1}) + \frac{e}{2\varepsilon_0} \Delta t \sum_{\ell} \left[(n_{m,n} + n_{m,n-1})(\mu_{m,n} + \mu_{m,n-1}) \right] \right\} \phi_{i+1,j} \\
&\quad + \frac{1}{2\Delta x^2} \left\{ (\varepsilon_{m-1,n} + \varepsilon_{m-1,n-1}) + \frac{e}{2\varepsilon_0} \Delta t \sum_{\ell} \left[(n_{m-1,n} + n_{m-1,n-1})(\mu_{m-1,n} + \mu_{m-1,n-1}) \right] \right\} \phi_{i-1,j}
\end{aligned} \tag{46}$$

and



$$\begin{aligned}
& \frac{\partial}{\partial y} \left[\left(\varepsilon_y + \frac{e}{\varepsilon_0} \Delta t \sum_{\ell} n_{\ell,y}^k \mu_{\ell,y}^k \right) \nabla \phi_y^{k+1} \right] \\
&= -\frac{1}{2\Delta y^2} \left\{ (\varepsilon_{m-1,n} + \varepsilon_{m,n} + \varepsilon_{m,n-1} + \varepsilon_{m-1,n-1}) \right. \\
&\quad \left. + \frac{e}{2\varepsilon_0} \Delta t \sum_{\ell} \left[(n_{m-1,n} + n_{m,n})(\mu_{m-1,n} + \mu_{m,n}) + (n_{m,n-1} + n_{m-1,n-1})(\mu_{m,n-1} + \mu_{m-1,n-1}) \right] \right\} \phi_{i,j} \\
&\quad + \frac{1}{2\Delta y^2} \left\{ (\varepsilon_{m-1,n} + \varepsilon_{m,n}) + \frac{e}{2\varepsilon_0} \Delta t \sum_{\ell} \left[(n_{m-1,n} + n_{m,n})(\mu_{m-1,n} + \mu_{m,n}) \right] \right\} \phi_{i,j+1} \\
&\quad + \frac{1}{2\Delta y^2} \left\{ (\varepsilon_{m,n-1} + \varepsilon_{m-1,n-1}) + \frac{e}{2\varepsilon_0} \Delta t \sum_{\ell} \left[(n_{m,n-1} + n_{m-1,n-1})(\mu_{m,n-1} + \mu_{m-1,n-1}) \right] \right\} \phi_{i,j-1}
\end{aligned} \tag{47}$$

On this substitution Poisson's equation becomes a five-point equation for the potential

$$a_{i,j} \phi_{i+1,j}^{k+1} + b_{i,j} \phi_{i-1,j}^{k+1} + c_{i,j} \phi_{i,j+1}^{k+1} + d_{i,j} \phi_{i,j-1}^{k+1} + e_{i,j} \phi_{i,j}^{k+1} = \Delta t S_{i,j}^k + \phi_{i,j}^k = f_{i,j} \tag{48}$$

$$\begin{aligned}
a_{i,j} &= \frac{1}{2\Delta x^2} \left\{ (\varepsilon_{m,n} + \varepsilon_{m,n-1}) + \frac{e}{2\varepsilon_0} \Delta t \sum_{\ell} [(n_{m,n} + n_{m,n-1})(\mu_{m,n} + \mu_{m,n-1})] \right\} \\
b_{i,j} &= \frac{1}{2\Delta x^2} \left\{ (\varepsilon_{m-1,n} + \varepsilon_{m-1,n-1}) + \frac{e}{2\varepsilon_0} \Delta t \sum_{\ell} [(n_{m-1,n} + n_{m-1,n-1})(\mu_{m-1,n} + \mu_{m-1,n-1})] \right\} \\
c_{i,j} &= \frac{1}{2\Delta y^2} \left\{ (\varepsilon_{m-1,n} + \varepsilon_{m,n}) + \frac{e}{2\varepsilon_0} \Delta t \sum_{\ell} [(n_{m-1,n} + n_{m,n})(\mu_{m-1,n} + \mu_{m,n})] \right\} \\
d_{i,j} &= \frac{1}{2\Delta y^2} \left\{ (\varepsilon_{m,n-1} + \varepsilon_{m-1,n-1}) + \frac{e}{2\varepsilon_0} \Delta t \sum_{\ell} [(n_{m,n-1} + n_{m-1,n-1})(\mu_{m,n-1} + \mu_{m-1,n-1})] \right\} \\
e_{i,j} &= -(a_{i,j} + b_{i,j} + c_{i,j} + d_{i,j}) \\
f_{i,j} &= -\sum_{\ell=1}^N \frac{q_{\ell}}{\varepsilon_0} - (\sigma_{diek})
\end{aligned} \tag{49}$$

(σ_{diek}) : The surface charge density accumulating on intersection between plasma region and dielectric is obtained from boundary condition.

The classical SOR technique is often used in two-dimensional discharge modeling. We can calculate the plasma densities at time with the electric potential at a given location and time. Updated plasma densities have the electric potential redistributed using Poisson equation. The plasma densities are assumed updated in this method, the electric potential is frozen, and vice versa. There is a time limitation to valid the assumptions of the frozen plasma densities and electric potential.

2.2.2.3. Radiation Transport Equation

We use the piecewise constant approximation (PCA), the last term in Eq. (28) becomes

$$\int n^*(\mathbf{r}', t) G(\mathbf{r}_{jk}, \mathbf{r}') d\mathbf{r}' = \sum_{l=1}^{N_x} \sum_{m=1}^{N_y} n_{lm}^*(t) \int_{lm} G(\mathbf{r}_{jk}, \mathbf{r}') d\mathbf{r}' \tag{50}$$

r_{jk} : is the center position of the $(j, k)_{th}$ cell

N_x, N_y : the number of cells in x and y directions

n_{lm}^* : constant density at the $(l, m)_{th}$ cell

The radiation transport matrix $A_{jk;lm}$ (Figure 2.4) is defined as the spatial integral of the kernel function over the volume of the $(j, k)_{th}$ cell,

$$A_{jk;lm} = \int_{lm} G(\mathbf{r}_{jk}, \mathbf{r}') d\mathbf{r}' \quad (51)$$

$A_{jk;lm}$ is the probability for a photon emitted within the $(l, m)_{th}$ cell to be reabsorbed at the center of the $(j, k)_{th}$ cell. The equation is simplified by analytic calculation,

$$A_{jk;lm} = \delta_{jl}\delta_{km} + A_{|j-l|,|k-m|}^{(a)} + A_{|j-l|,|k-m|}^{(b)} + A_{|j-l|,|k-m|}^{(c)} + A_{|j-l|,|k-m|}^{(d)} \quad (52)$$

$$A_{|j-l|,|k-m|}^{(a)} = -\frac{\Delta y \left(|k-m| + \frac{1}{2} \right)}{12\pi^2 \sqrt{2k_0}} \Gamma^2 \frac{1}{4} \int_{(|j-l|-1/2)\Delta x}^{(|j-l|+1/2)\Delta x} \left[x^2 + \Delta y^2 \left(|k-m| + \frac{1}{2} \right)^2 \right]^{-\frac{5}{4}} dx$$

$$A_{|j-l|,|k-m|}^{(b)} = -\frac{\Delta x \left(|j-l| + \frac{1}{2} \right)}{12\pi^2 \sqrt{2k_0}} \Gamma^2 \frac{1}{4} \int_{(|k-m|-1/2)\Delta x}^{(|k-m|+1/2)\Delta x} \left[x^2 + \Delta y^2 \left(|j-l| + \frac{1}{2} \right)^2 \right]^{-\frac{5}{4}} dy$$

$$A_{|j-l|,|k-m|}^{(c)} = -\frac{\Delta y \left(|k-m| - \frac{1}{2} \right)}{12\pi^2 \sqrt{2k_0}} \Gamma^2 \frac{1}{4} \int_{(|j-l|-1/2)\Delta x}^{(|j-l|+1/2)\Delta x} \left[x^2 + \Delta y^2 \left(|k-m| - \frac{1}{2} \right)^2 \right]^{-\frac{5}{4}} dx$$

$$A_{|j-l|,|k-m|}^{(d)} = -\frac{\Delta x \left(|j-l| - \frac{1}{2} \right)}{12\pi^2 \sqrt{2k_0}} \Gamma^2 \frac{1}{4} \int_{(|k-m|-1/2)\Delta x}^{(|k-m|+1/2)\Delta x} \left[x^2 + \Delta y^2 \left(|j-l| - \frac{1}{2} \right)^2 \right]^{-\frac{5}{4}} dy$$

$A_{|j-l|,|k-m|}^{(a)}$, $A_{|j-l|,|k-m|}^{(b)}$, $A_{|j-l|,|k-m|}^{(c)}$, and $A_{|j-l|,|k-m|}^{(d)}$: surface segments at the top, the right hand side, the left side, and the bottom surfaces of the $(l, m)_{th}$ cell.

2.2.2.4. Boundary Condition

The boundary conditions for the above equations are an essential part of the description of the problem. The flux form at the left dielectric surface shown in Figure 2.5 is

$$\left(\Gamma_{x, m+\frac{1}{2}, n} \right)_{left-diel} = -\beta_{m,n} n_{m,n} \quad (53)$$

From the previous equation, we can find the coefficient $\beta_{m,n}$. We calculated the flux at the grid point, is ahead $(\Delta x/2)$ than the position of densities. The $m-1$ (behind dielectric surface) and m (plasma region) are needed to calculate flux $(m-1/2)$ at the boundary. Because plasma densities are zero at m , only $\beta_{m,n}$ coefficient remains. With the same reason, $\alpha_{m,n}$ coefficient remains at the right dielectric surface.

The boundary condition of the surface charging equation at the interface between the dielectric surface and the plasma region is followed:

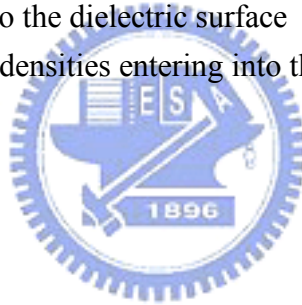
$$(\varepsilon_0 E_0 - \varepsilon_1 E_1) \cdot n_s = \sigma \quad (54)$$

E_0 : Electric field in the plasma region

E_1 : Electric field at the dielectric surface

n_s : Unit vector perpendicular to the dielectric surface

σ : Time integration of charge densities entering into the dielectric surface



Chapter 3

Simulation of Plasma Backlight

In this chapter we use two numerical models: the global model and fluid model presented in Chapter 2 to simulate the micro-discharge in a plasma backlight unit. The aim is to find out the actual improvements of the plasma backlight technology.

3.1 Global simulation

Here presents a simple analysis, for plasma applied to display panel backlight, by the global model which is introduced in Lieberman's book. For the Xenon plasma, electron impact reaction rate from the integration of cross-section. The simulation cross sections for several reactions with respect to electron energy are shown in Figure 3.1.

is complex to calculate. There are some parameters for the analysis,

- ✧ Whole domain is a cylinder structure with radius 0.783 cm and height 0.28 cm
- ✧ Input power is 0.1 W , which is reduced by assuming panel size $32 \times 30 \times 0.28\text{ cm}^3$ and power 50 W to a unit volume.

3.2 Fluid simulation

Table 3 outlines the characteristic properties of the micro-discharges considered in this section. We use the fluid model to simulate the micro-discharges in plasma backlight module. All calculations presented here are based on the standard geometry in Figure 3.2. Figure 3.2 shows the electrode structure on bottom plate. In this approach, we solve the continuity equations for the species number density, using the drift-diffusion approximation for the species flux. The electron transport coefficients (Figure 3.5~3.8) (mobility, μ_e , diffusion

coefficient, D_e , Electron energy, and Ionization coefficient) are from the BOLSIG, a user friendly code for the numerical solution of the Boltzmann equation for electrons in weakly ionized gases and in steady-state, uniform fields.

Table 3. Plasma backlight unit details and operating parameters.

	Symbol (unit)	Value
Gas		Pure Xe
Gas pressure	p (Torr)	90
Gas temperature	T (K)	350
Cell length	l (mm ²)	20.5
Cell width	w (mm)	9.4
Protruded electrode length	l_E (mm)	1.5
Protruded electrode width	w_E (mm)	4
Electrode gap width	w_g (mm)	5.4
Pulse frequency	f (kHz)	55
Applied pulse voltage amplitude	V_{amp} (V)	1740
Dielectric thickness	D_{die} (μm)	400
Dielectric relative permittivity		12

3.2.1. Applied Pulse Voltage

A plasma backlight discharge is generated by AC voltage pulses on the electrodes. Figure 3.7 is the waveform of the applied pulse voltage examined in this work. V_a is the voltage amplitude. The duty ratio is defined as $r_d = T_{on} / (T_{on} + T_{off})$, where T_{on} and T_{off} are the periods of 'on state' and 'off state' of the pulse voltage. Figure 3.8 shows the pulse shapes of the applied voltages biased at the electrodes. Because the power supply is restrained unable to provide sufficient energy singly, so it uses two smaller voltages to build bigger one.

Unipolar-pulsed excitation of Xenon excimer lamps has been proved to be able to improve dramatically the energy efficiency of DBDs in producing VUV excimer radiation [Liu and Neiger 2003]. The occurrence of the secondary discharge improves the performance of DBD technology. The VUV spectra of Xenon excimer radiation under unipolar pulse

excitation is identical to that under sine wave excitation. So we use unipolar-pulsed voltage in this simulation.

3.2.2. Parametric Studies

Simulation domain configuration is presented as Figure 2.1. The y -direction, w , between the cathode and anode is 9.4mm, the thickness of the dielectric lay $D_{die} = 400\mu m$ and the relative permittivity of the dielectric is 12. At the center of electron 2 builds a tip with 4 mm height.

The grid dimensions used here were 165 points in the X -direction and 95 points in the Y -direction, for a total of 15,675. Applied voltage on electrode 1 is from -100 to 815 V while electrode 2 is from 300 to -525 V, with working frequency 55 kHz, duty ratio 35%, and two pulse voltages are the at same phase. Background gas pressure is 90 Torr. Gas and ions temperature are assumed 350 K.



Chapter 4

Results and Discussion

4.1 Global model

The variation of the plasma parameters, plasma density, sheath potential, electron temperature, mean free path, and debye length, with discharge pressure are shown in Figure 4.1~4.5. We assume a cylindrical stainless steel chamber with length $L = 2.8$ mm and radius $R = 7.83$ mm with absorbed power 0.1W.

While pressure rising, the probability of ionization of Xenon will increase, so the electron density (Figure 4.1) increases gradually. Plasma density was varied between 6×10^{12} and $5.5 \times 10^{13} \text{ cm}^{-3}$.

Sheath potential (Figure 4.2) is the voltage difference between bulk and boundary, which will affect material of edge. Figure 4.3 shows the electron temperature dependence on pressure for pure Xe discharges. The trends are with T_e decreasing with increase pressure. This variation in the electron temperature and sheath potential with pressure is due to the change in the electronegativity ratio with pressure. The electron energy reduced will influence the ionization rate. Mean free path, the average distance the particle travels between collisions with other particles, is shown with increasing pressure (Figure 4.4). Debye length, named after the Dutch physical chemist Peter Debye, is the scale over which mobile charge carriers (e.g. electrons) screen out electric fields in plasmas and other conductors. It is about 10^{-4} cm.

4.2 Fluid model

The simulations of the discharge were performing with a two-dimensional fluid model to study the evolution of the plasma. The model is based on solutions of electron and ion transport equations coupled with Poisson's equation for the electric field in a 2D Cartesian

geometry.

4.2.1 Typical Test Case

The gas and driving pulse are fixed as 90 Torr of Xe gas and amplitude 1740V with frequency 55 kHz and duty ratio 35 %. Applied voltage on electrode 1 is from -100 to 815 V while electrode 2 is from 300 to -525 V. Figure 4.6 shows the positions of the following results. Figure 4.7 is the contour plot of potential and related electric field distribution in different phase of pulse. Plasma potential stably sustains despite the changes of applied power. Electric field, notability, is high in the sheath region, especially at tip edge, which has sharp shape and close to cathode. Figure 4.8~4.10 show the electron, ions, and excited species densities in different phase of pulse. During pulse rising, the electrons are mainly generated by ionization near the tip of Electron 2 where the electric field is the largest. Figure 4.11 is the power absorptions of charged species.

Figure 4.12 shows the time evolutions of the spatially averaged quantities at f 55kHz, V_a 1740V, duty ratio 35%, and gas pressure 90Torr. Double discharges are obtained in the simulation results. The first discharge occurs at the rising front or at the top of the applied voltage pulse; the second discharge with reversed polarity occurs at the falling flank or at the end of the falling flank. The primary discharge is energized directly by the external circuit and extinguished by charge accumulation on the dielectric. The secondary discharge is completely energized by the energy stored by memory charges deposited by the primary discharge and ceases after the stored energy of memory charges is consumed. During the secondary discharge there is no energy injection from the external circuit. During pulse-off, the potential changes litter in bulk region and almost all the gradient occur near the electrodes. The densities are quickly dissipated by the charging of the dielectric layers which creates a voltage across the gas gap opposing the voltage across the electrodes.

During pulse raising or falling, a great deal of ions bump into electrodes and induce secondary electron back to plasma, where more ions and electron will be generated. High electric field at edge of tip collects ions, also comes along with higher secondary electron density and excited species. Excited species Xe^* and Xe_2^* , which are increased by electron impact excitation reaction, are closely bound up with ultraviolet light 147 nm and 173 nm, relatively. Even $\text{Xe}_2^*(^3\Sigma_u^+)$ density is considerably smaller than $\text{Xe}^*(^3P_1)$ density, $\text{Xe}_2^*(^3\Sigma_u^+)$ contributes more strongly to the visible light emission through excitation of the phosphor. The time dependence of powers absorbed in the plasma were shown. Since most reactions depend on the electron impact reaction, we can observe that electron absorbs most energy. Because of lower excited energy and heavier particle, Xe_2^+ absorbs most energy while during pulse-off.

The cycle averaged spatial density distributions are presented in Figure 4.13 and Figure 4.14. The plasma was seen to extend over the area between the electrodes. The triangular discharge patterns were made between tipped cathode and anode by pulsed voltage operation. The density distribution of Xe_2^+ is much uniform. Simulated dominant UV radiation is 173nm, which is consistent with experimental observation. The power absorption of Xe_2^+ is much uniform compared with Xe^+ .

4.2.2 Efforts of Pulse Frequency

The different appearances of the discharge are shown for the pressure range 45~85 kHz and pulse width 5.38 μs , in which all the other input parameters keep the same. Figure 4.15 and 4.16 show the time evolutions of the spatially averaged densities versus pulse frequency. Double discharges are also obtained in the results. As the pulse frequency increases, the number of residual ions and electrons increases because of the length of non-discharge period. These increases in the number of residual ions and electrons reduced the electron temperature during a discharge. Figure 4.17 shows the time evolutions of the spatially averaged power of

charged species versus pulse frequency. Power absorption of Xe^+ is sensitive to pulse frequency. Figure 4.18 shows the variations of each species in different pulse frequency. The detailed set of results showing the temporal averaged of the main parameters during the period of active is shown in Table 4. $\text{Xe}^*(^3\text{P}_2)$ is the dominated excited species sensitive to pulse frequency. The power absorption of Electron is the highest. The efficiency of power absorption is higher at high pulse frequency.

4.2.3 Effects of Gas Pressure

Figure 4.19~4.20 show the time evolutions of the spatially averaged densities of charged and excited species at the pulse frequency of 65kHz and the duty ratio of 35%. The Xenon pressures are 90~120Torr. The calculated population densities of the species considered $\text{Xe}^*(^3\text{P}_1)$, $\text{Xe}^*(^3\text{P}_2)$, Xe^{**} , $\text{Xe}_2^*(\text{O}_u^+)$, $\text{Xe}_2^*(^1\Sigma_u^+)$, and $\text{Xe}_2^*(^3\Sigma_u^+)$, against time was presented. The second peak is weaker in the high pressure. Power absorption of each charged species is shown in Figure 4.21. Figure 4.22 is the averaged quantities versus gas pressure 90~120Torr. The averaged quantities decrease with increased gas pressure up to 110 Torr, then increase slightly with increased pressure. Averaged plasma density (Table 5) has high value at pressure 90 Torr, comes up with more excited species. $\text{Xe}^*(^3\text{P}_2)$ has peak value at pressure 90 Torr, and minimum value at 110 Torr. The advantage of pulse power at pressure 90 Torr, which presents effective power absorption, is clearly shown that higher plasma density comes with higher excited species, as well as luminance.

4.2.4 Effects of Duty Ratio

The time evolutions of the spatially averaged quantities at voltage amplitude 1740 V, pulse frequency 65 kHz, gas pressure 90 Torr, duty ratio 25~75 % are shown in Figure 4.23~4.25.

At the operation with duty ratio 75%, the maximum of the first peaks of charged and excited species densities decrease comparing with the case of 25 %. The second peak of the excited species density becomes strong as the duty ratio increases. The primary and second discharges can be separated by increasing the voltage pulse width. Figure 4.25 is the time evolutions of the power of charged species versus duty ratio.

The averaged densities of charged and excited species versus duty ratio were shown in Figure 4.26. The luminance decreases with increasing duty ratio. A small duty ratio reduces the power absorption. This is the reason why the efficacy is improved with shorter pulse width operation. Detail data lists in Table 6.

4.2.5 Effects of Dielectric Thickness

The electrode gap width, w , between the cathode and anode is 6.4 mm, the thickness of the dielectric layer D_{die} 200 μm ~700 μm , and the relative permittivity of the dielectric is 12. Figure 4.27~4.29 show the time evolutions of the spatially averaged quantities versus dielectric thickness. During pulse-on or pulse-off, electric field violently changing, charged particles gain power from the sheath, therefore, more charged particle and excited particles generate. After pulse-on or pulse-off, the sheath reform and discharge sustain by the plasma potential. The integral characteristics are not very sensitive to dielectric thickness. Figure 4.30~4.33 show the cycle averaged quantities versus dielectric thickness. We can observe the quantities broadening increasing with increasing the dielectric layer thickness. Figure 4.34 is the averaged quantities include the densities of charged and excited specie, and power absorption of charged species. Detail data list in Table 7. Xe^* , is the dominated excited species, which ($^3\text{P}_2$) has peak value at thickness 200 μm and ($^3\text{P}_1$) at 700 μm . Averaged plasma density has high value at thickness 200 μm , comes up with more excited species. Effective power absorption is at thickness 700 μm .

Chapter 5

Conclusions

5.1 Summary

Two-dimensional fluid simulation of plasma backlight has been used to study a plasma backlight lamp for application in LCD backlighting, which consists of series of paired and protruded electrode lines of same shape for AC driving. It was shown that spatiotemporal profiles of the concentration of electrons, ions, and excited species in different simulation conditions. A unipolar-pulsed voltage is used to improve the energy efficiency in producing VUV excimer radiation. This type of discharge generally traces emissions have two peaks per pulse. We qualitatively present physical properties of potential and electric field, as well as densities comparable with experiment.

The main conclusions of this study can be briefly summarized as follows:

1. Obtained and fully understood a 2-D fluid modeling code using Cartesian mesh, which shall help us to speed up the code development.
2. Plasma backlight simulations
 - (1). Typical test case
 - i. Double discharges are obtained
 - ii. The discharge occurring between each electrode pair is triangular in shape
 - iii. The mainly emitted 173 nm ultraviolet light is well conformed to the experiment data
 - (2). Effect of pulse frequency
 - i. As pulse frequency increases, the intensity of VUV emissions increases
 - ii. The density of Xe^+ increases 50%, and $\text{Xe}_2^*(^3\Sigma_u^+)$ density increases 48%, while frequency varies from 45 kHz to 85 kHz.

(3). Effect of gas pressure

- i. Better luminance is at 90 Torr and minimum at 110 Torr

(4). Effects of duty ratio

- i. As the duty ratio decreases, higher intensity of VUV emissions is obtained, while luminance and efficacy also increase.
- ii. Low duty ratio reduces the power consumption

(5). Effect of dielectric thickness

- i. The densities of charged and excited species have the peak value at dielectric thickness 200 μm
- ii. Better power absorption is at 700 μm and minimum at 300 μm
- iii. The density broadening increases with increasing the dielectric layer thickness

5.2 Recommendations of the Future Work

Based on this study, future work is suggested as follows:

1. To fully understand the radiation trapping factor.
2. Parametric study
 - (1). Structure
 - (2). Mixture of gases
 - (3). Dielectric constant
3. Consider the electron energy equation in fluid model
4. Three dimensional code development
5. Parallelization of 2-D and 3-D fluid codes

References

- [1]. Akahi, H., Oda, A., and Sakai, Y., "Effect of secondary electron emission on filament discharge in dielectric barrier discharge Xe excimer lamp", XXVI ICPIG, Eindhoven, the Netherlands, 18-22 July 2005.
- [2]. Brauer, I., Punset, C., Purwins, H. G., and Boeuf, J. P., "Simulations of self-organized filaments in a dielectric barrier glow discharge plasma", J. Appl. Phys., 85, pp. 7569-7572, 1999.
- [3]. Chen, G. and Raja, L. L., "Fluid modeling of electron heating in low-pressure, high-frequency capacitively coupled plasma discharges", J. Appl. Phys., 96, pp. 6073-6081, 2004.
- [4]. Eckstrom, D. J., Nakano, H. H., Lorents, D. C., Rothem, T., Betts, J. A., Lainhart, M. E., Dakin, S. A., and Maenchen, J.E., "Characteristics of electron-beam-excited Xe₂* at low pressures as a vacuum ultraviolet source", J. Appl. Phys., 64, pp. 1679-1690, 1988.
- [5]. Falkenstein, Z and Coogan, J. J., "The development of a silent discharge-driven XeBr* excimer UV light source", J. Phys. D: Appl. Phys., 30, pp. 2704-2710, 1997.
- [6]. Fiegler, M., Ziemssen, K., Homberg, B., "13.1: A high resolution 5 mega pixel LCD display for medical applications with mercury-free flat panel lamp backlighting (PLANON[®])", SID, 2003.
- [7]. Holstein, T, "Imprisonment of resonance radiation in gas", Phys. Rev. 72, 1947.
- [8]. Holstein, T, "Imprisonment of resonance radiation in gas. II", Phys. Rev. 83, 1951.
- [9]. Kim, Allen, "Emerging display technologies: solid-state light source brighten up the display market", FID, 2, pp. 5-6, 2005.
- [10]. Kim, H. C., Iza, F., Yang, S. S., Radmilovi'c-Radjenovi'c, M., and Lee, J. K., "Particle and fluid simulations of low-pressure plasma discharges: benchmarks and kinetic effects", J. Phys. D: Appl. Phys., 38, pp. R283-R301, 2005.

- [11]. Kinder, R. L. and Kushner, M. J., "Wave propagation and power deposition in magnetically enhanced inductively coupled and helicon plasma sources", J. Vac. Sci. Technol. A, 19, pp. 76-86, 2001.
- [12]. Kratzer, M., Brinkmann, R. P., Sabisch, W., and Schmidt, H., "Hybrid model for the calculation of ion distribution functions behind a direct current or radio frequency driven plasma boundary sheath", J. Appl. Phys., 90, pp. 2169-2179, 2001.
- [13]. Lieberman, M. A. and Gottscho, R. A., "Design of high density plasma sources for material processing", Physics of Thin Films, 18, ed. by Francombe, M. and Vossen, J., Academic Press, New York, pp. 1-119, 1994.
- [14]. Lo, D., Shangguan, C., Kochetov, I. K., and Napartovich, A. P., "Experimental and numerical studies on Xe_2^* VUV emission in the fast electric discharge afterglow", J. Phys. D: Appl. Phys., 38, pp. 3430-3437, 2005.
- [15]. Makabe, T., Advances in Low Temperature RF Plasmas: Basis for Process Design, Elsevier science, 2002.
- [16]. Oda, A., Sakai, Y., Akashi, H., and Sugawara, H., "One-dimensional modeling of low-frequency and high-pressure Xe barrier discharges for the design of excimer lamps", J. Phys. D: Appl. Phys., 32, pp. 2726-2736, 1999.
- [17]. Oda, A., Sugawara, H., Sakai, Y., and Akashi, H., "Estimation of the light output power and efficiency of Xe barrier discharge excimer lamps using a one-dimensional fluid model for various voltage waveform", J. Phys. D: Appl. Phys., 33, pp. 1507-1513, 2000.
- [18]. Reale, F., "Thermal conduction in a 2-D FCT plasma hydrodynamic code", Comp. Phys. Comm., 86, pp. 13-24, 1995.
- [19]. Scharfetter, D. L. and Gummel, H. K., "Large-signal analysis of a silicon read diode oscillator", IEEE Trans. Electron Devices ED, 16, pp. 64-77, 1969.
- [20]. Shiga, T., Pitchford, L. C., Boeuf, J. P., and Mikoshiba, S., "Study of efficiency in a

mercury-free flat discharge fluorescent lamp using a zero-dimensional positive column model", J. Phys. D: Appl. Phys., 36, pp. 512-521, 2003.

[21]. Yang, S. S., Lee, J. K., Ko, S. W., Kim, H. C., and Shon, J. W., "Two-dimensional kinetic and three-dimensional fluid-radiation transport simulation of plasma display panel", Contrib. Plasma Phys., 44, pp. 536-541, 2004.

[22]. Zhang, J. Y. and Boyd, I. W., "Efficient XeI* excimer ultraviolet sources from a dielectric barrier discharge", J. Appl. Phys., 84, pp. 1174-1178, 1998.



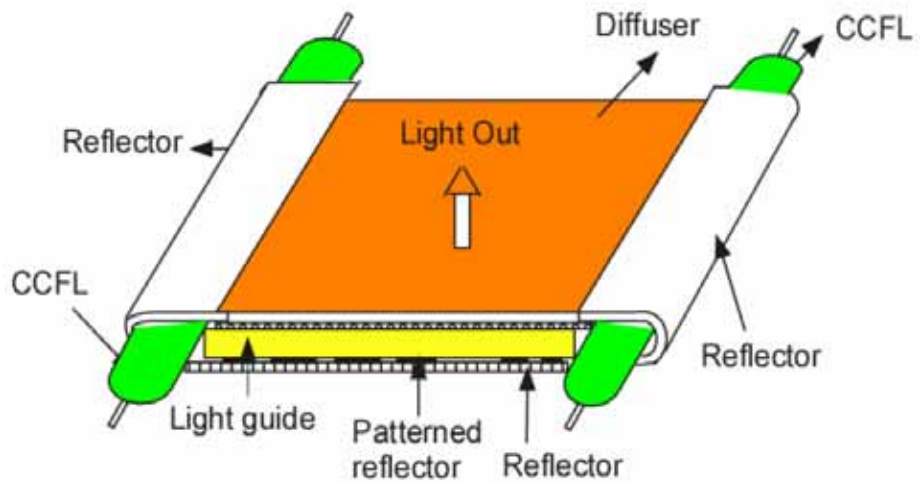


Figure 1.1. Schematic drawing of a cold cathode fluorescent lamp (CCFL).

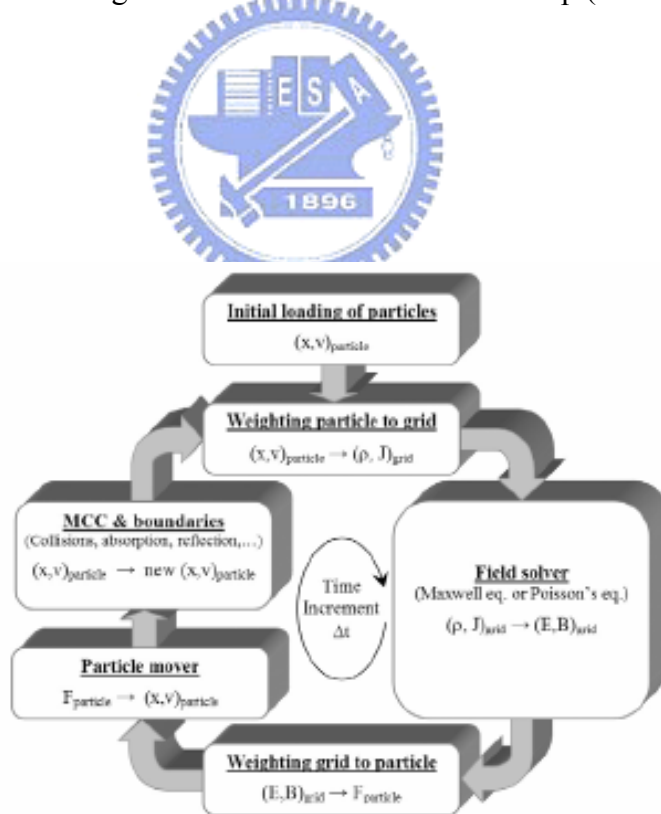


Figure 1.2. Flow diagram of a PIC-MCC model.

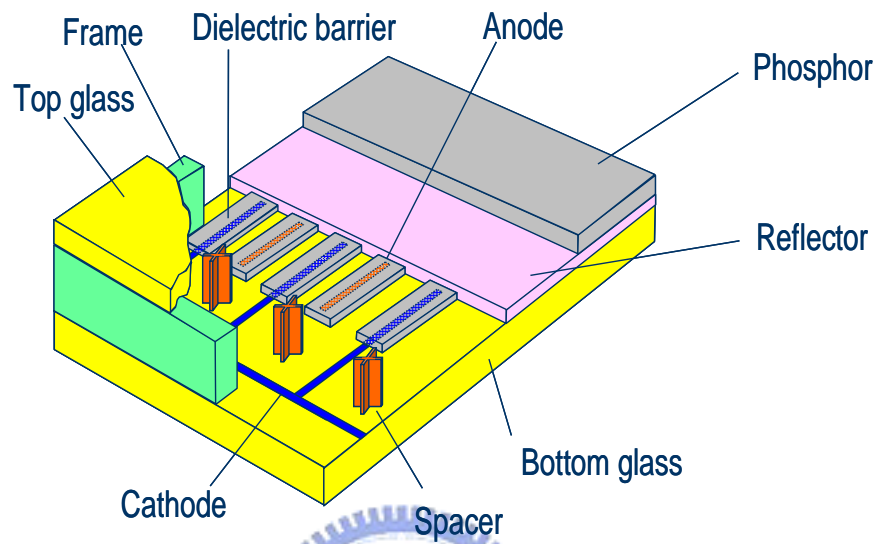


Figure 1.3. Schematic drawing of a plasma backlight unit.

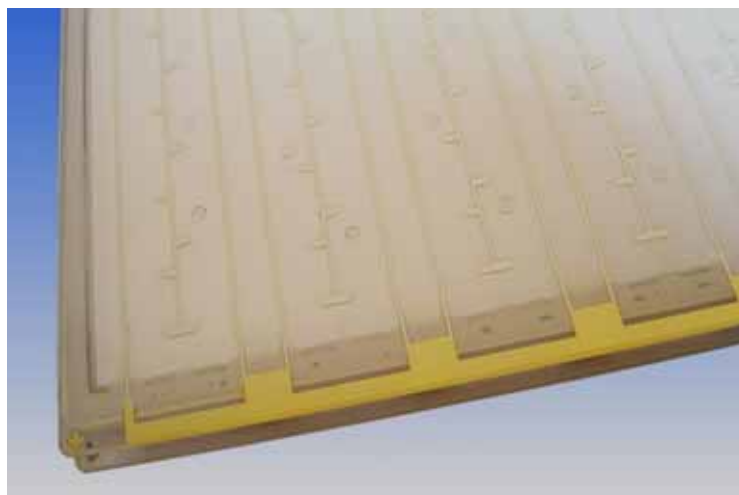


Figure 1.4. Schematic of electrode shape.

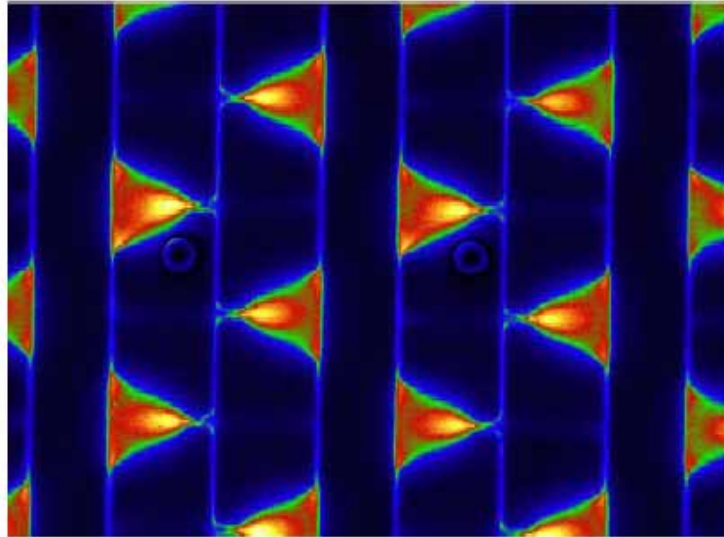


Figure 1.5. Plasma backlight micro-discharges

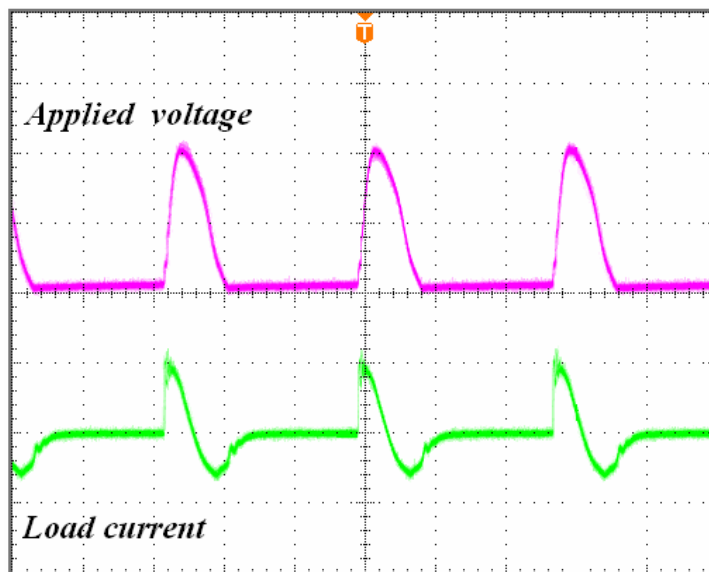


Figure 1.6. The waveform of applied voltage and load current.

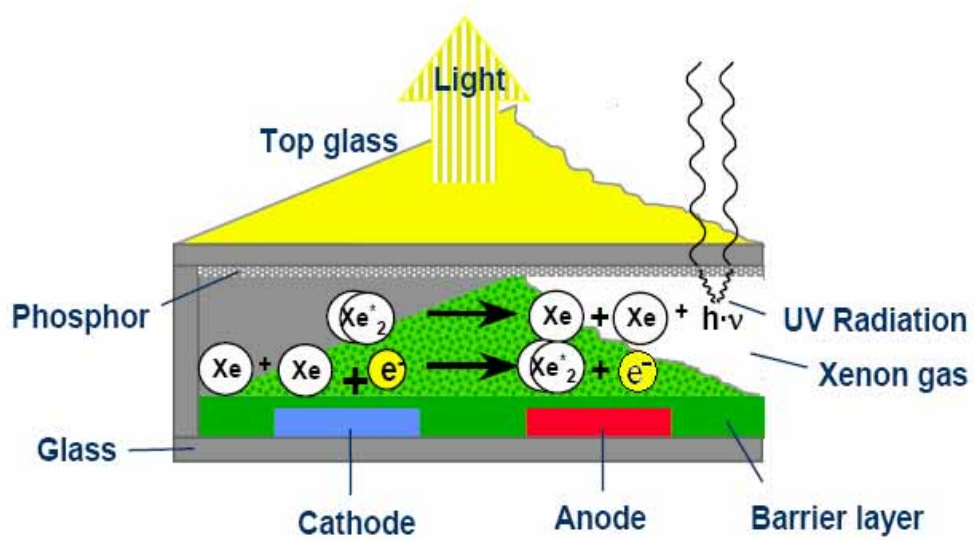


Figure 1.7. Plasma backlight operating principle.

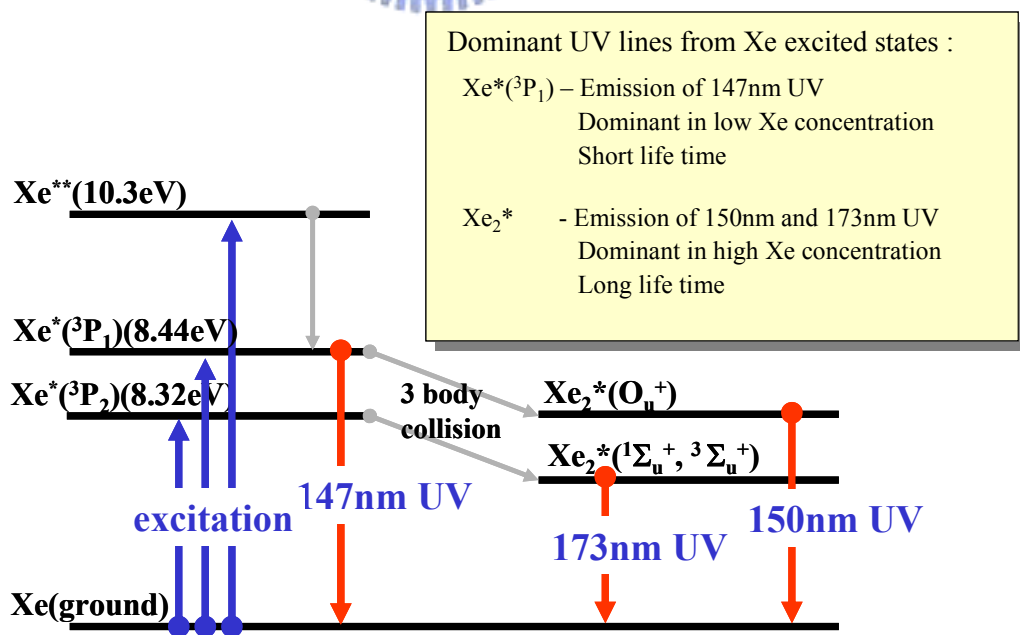


Figure 1.8. Energy level diagram of Xe

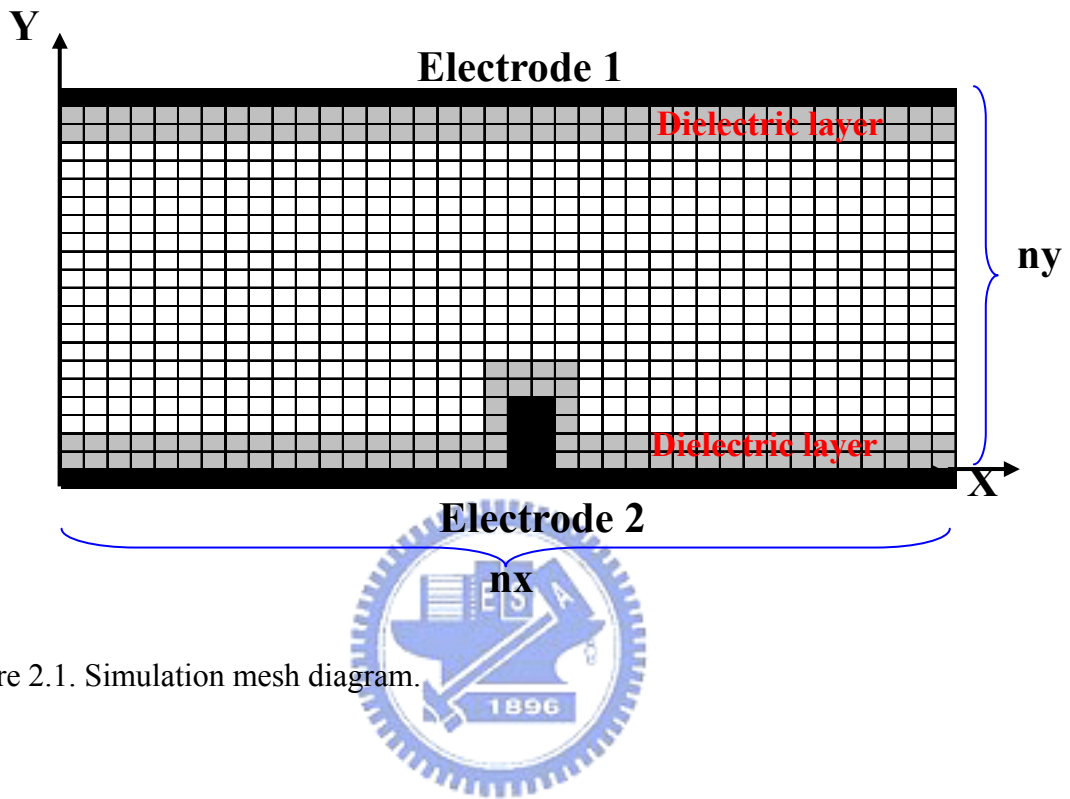


Figure 2.1. Simulation mesh diagram.

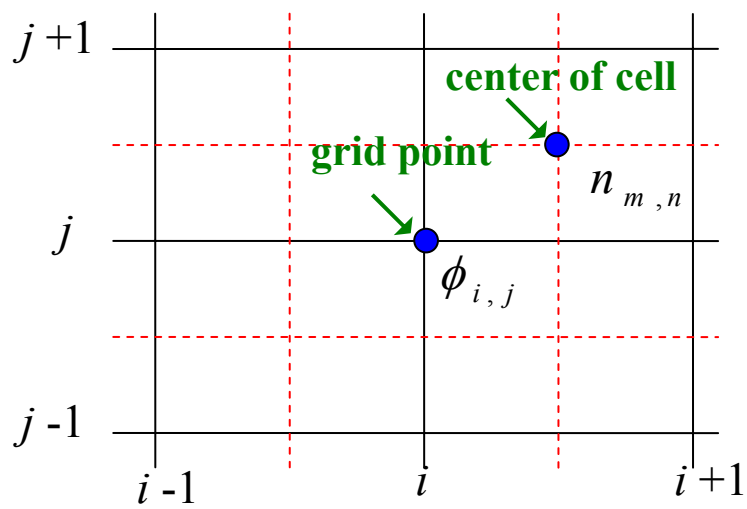


Figure 2.2. Computation cell geometry.

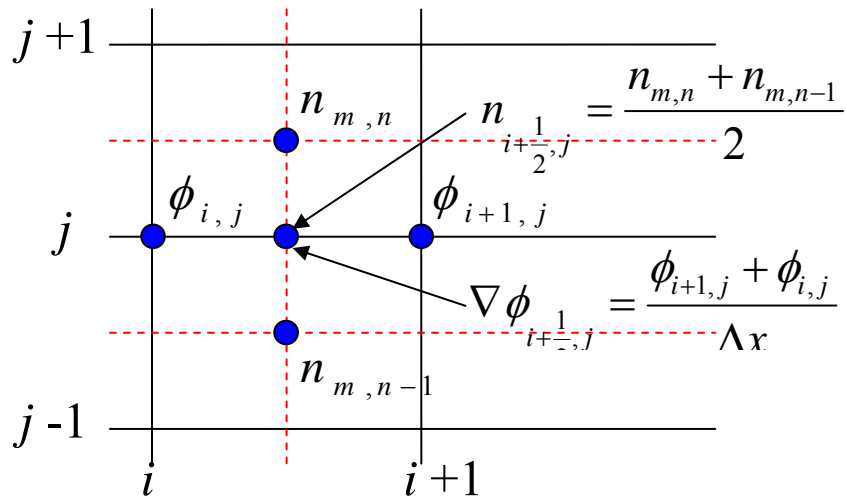


Figure 2.3. Dielectric constant ϵ , number n , and mobility μ weight the grid point.

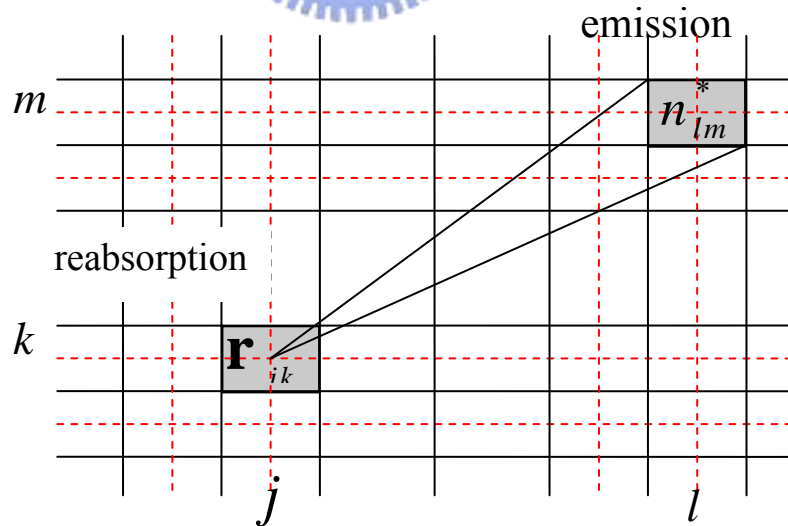


Figure 2.4. Simulation mesh diagram of radiation transport.

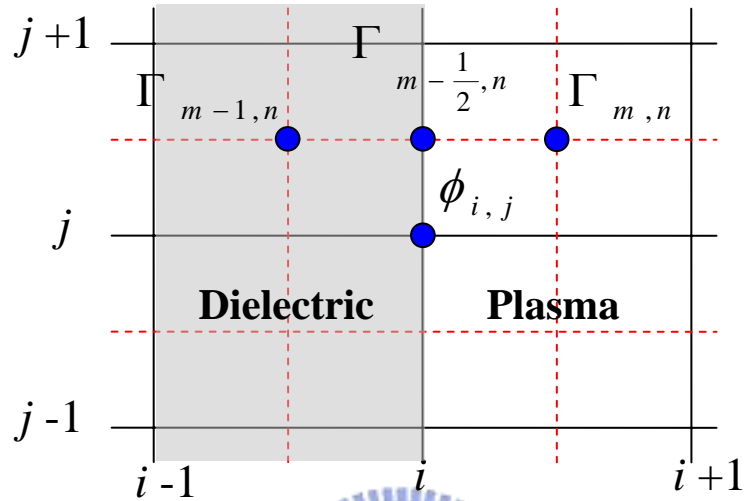


Figure 2.5. Neuman boundary condition used on the side boundary.

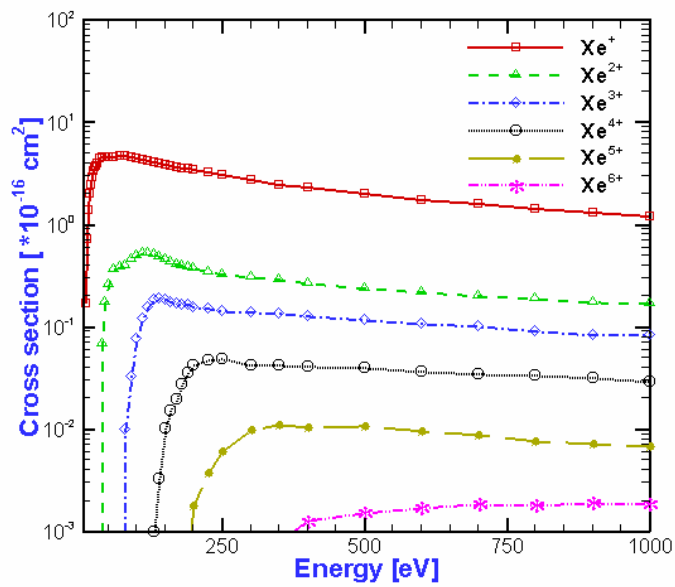


Figure 3.1. Neutral Xenon ionization cross-section

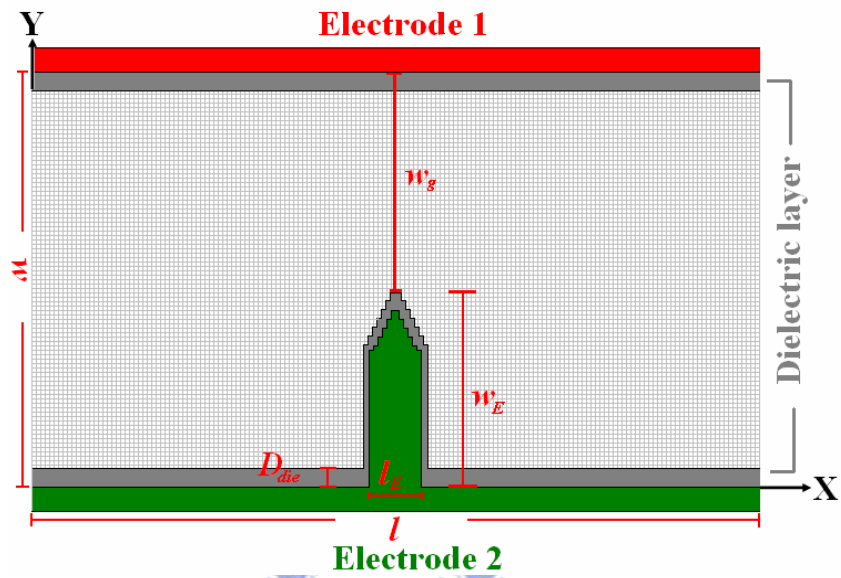


Figure 3.2. Schematic of the simulated geometry.

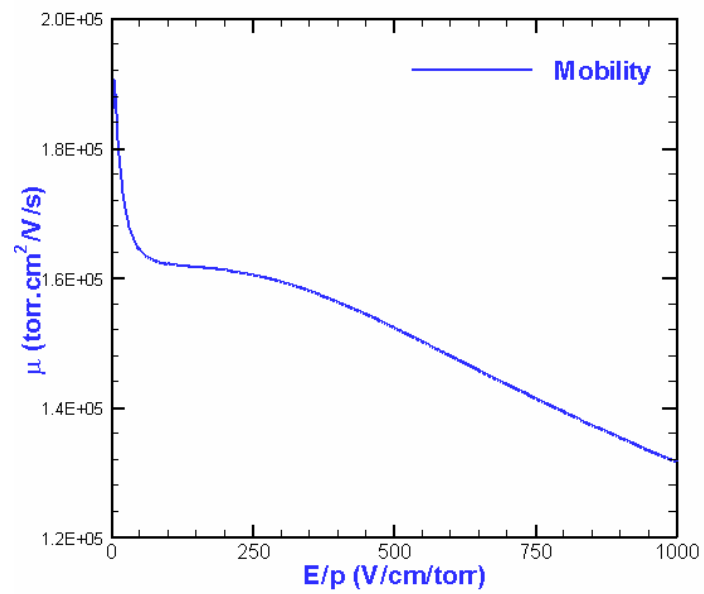


Figure 3.3. Mobility in various E/p .

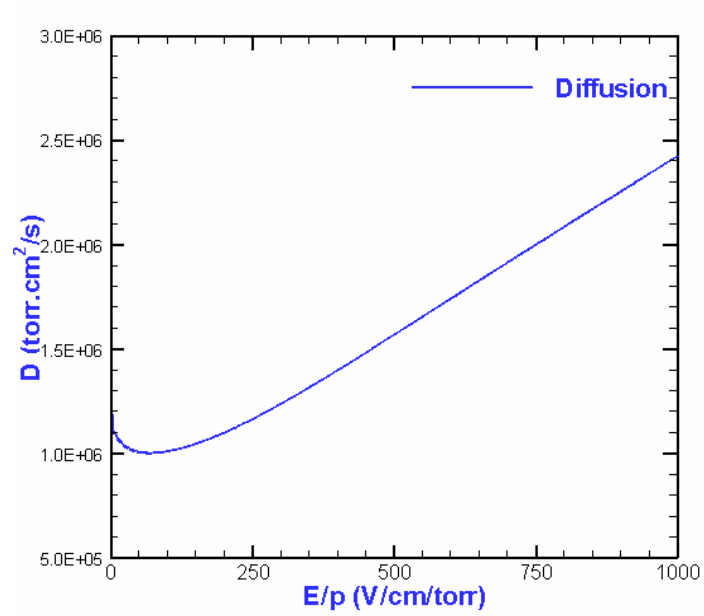


Figure 3.4. Diffusion in various E/p.

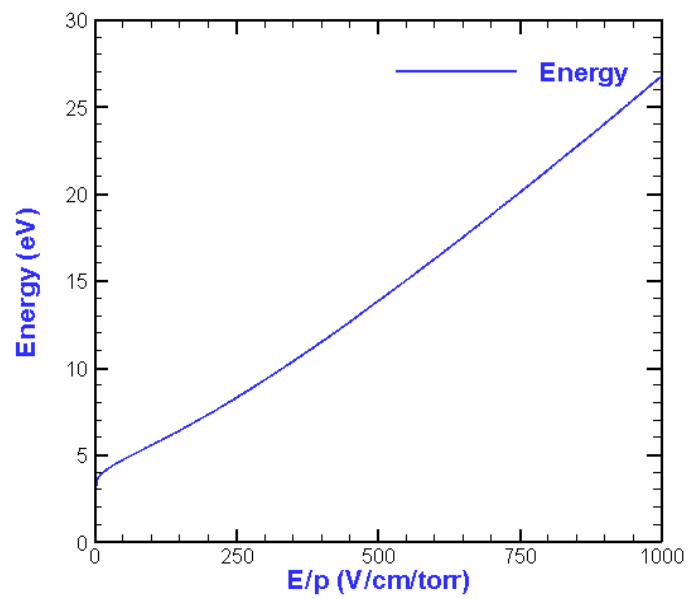


Figure 3.5. Energy in various E/p.

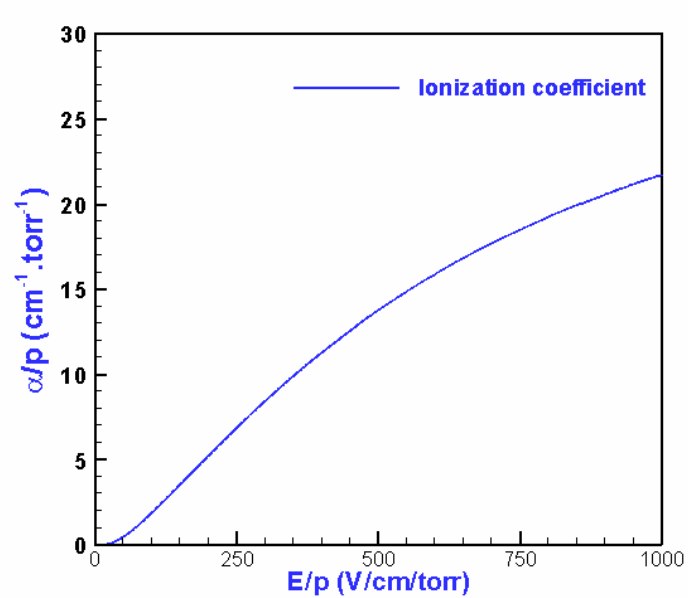


Figure 3.6. Ionization coefficient in various E/p .

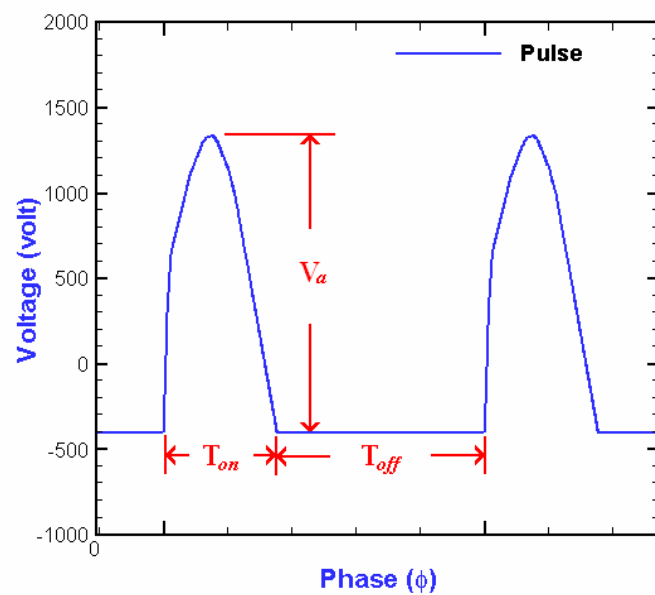


Figure 3.7. The waveform of the applied pulse voltage.

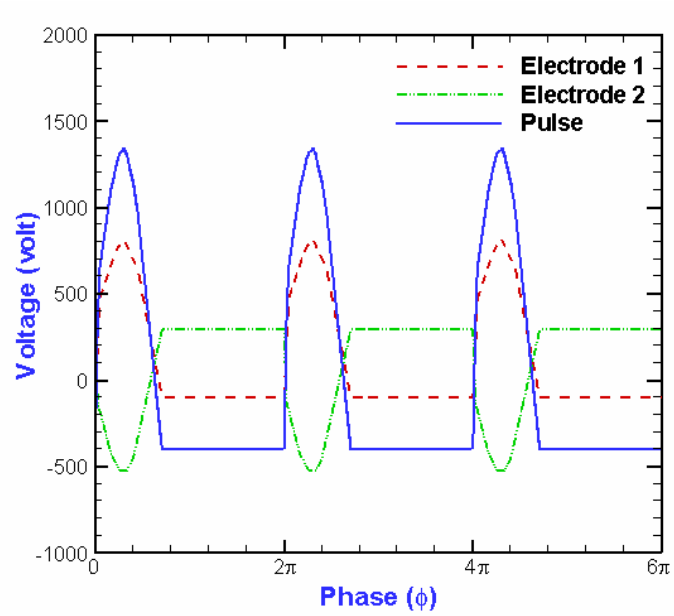


Figure 3.8. Pulse shapes of the applied voltages biased at the electrodes.

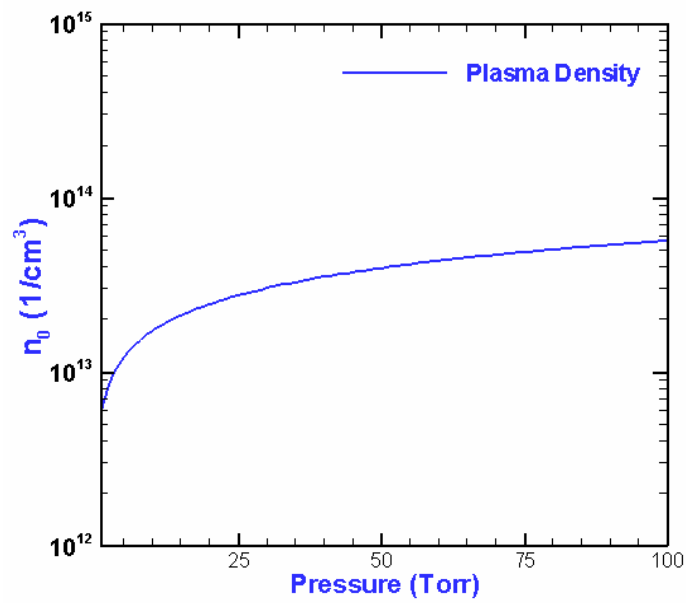
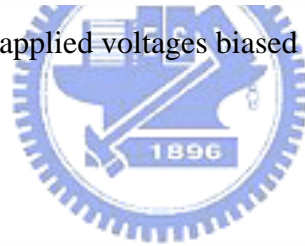


Figure 4.1. Plasma density versus frequency.

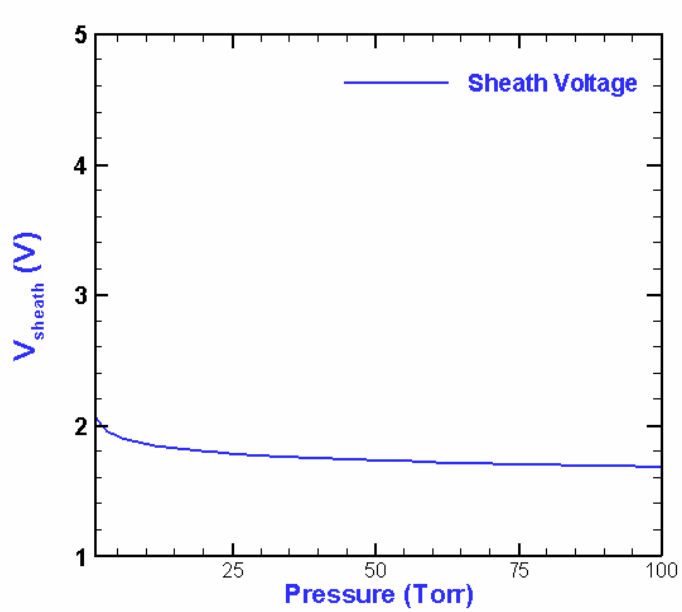


Figure 4.2. Sheath voltage versus frequency.

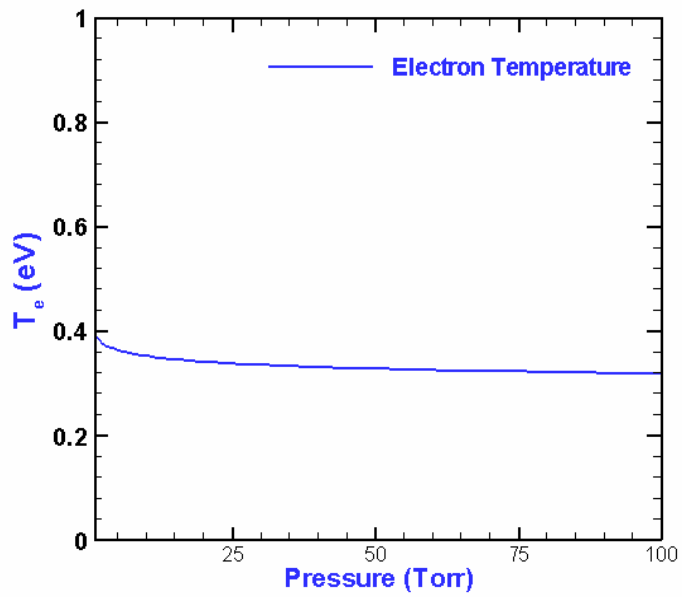


Figure 4.3. Electron temperature versus frequency.

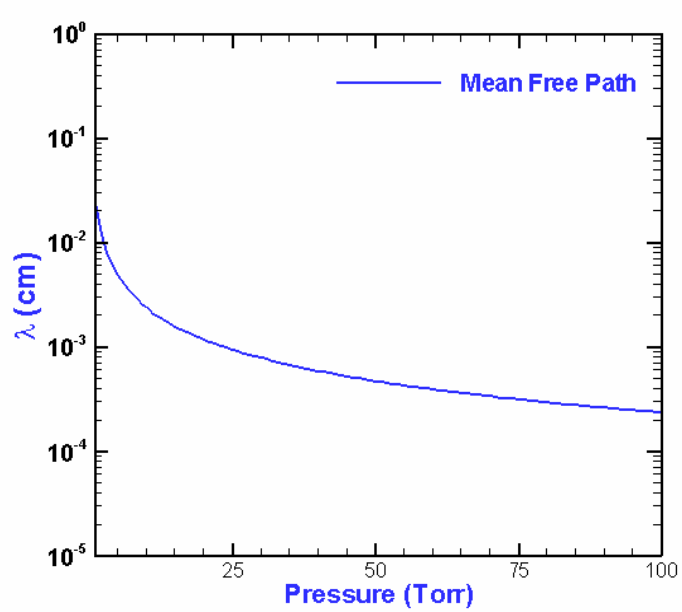


Figure 4.4. Mean free path versus frequency.

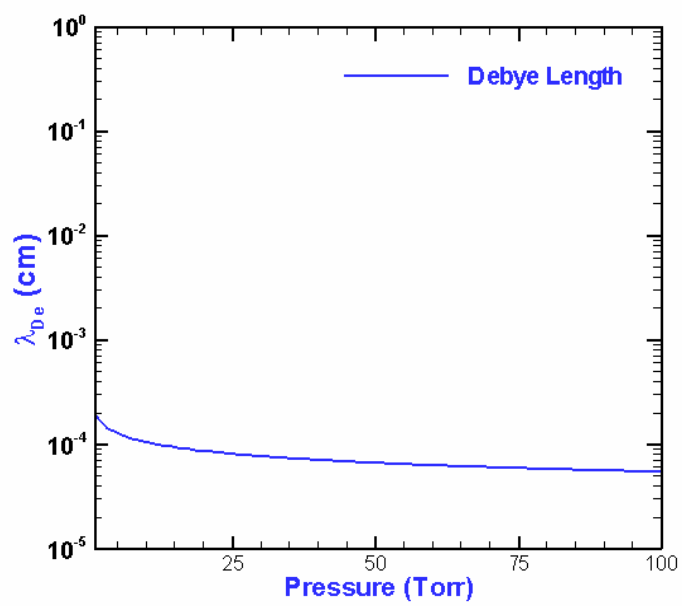


Figure 4.5. Debye length versus frequency.

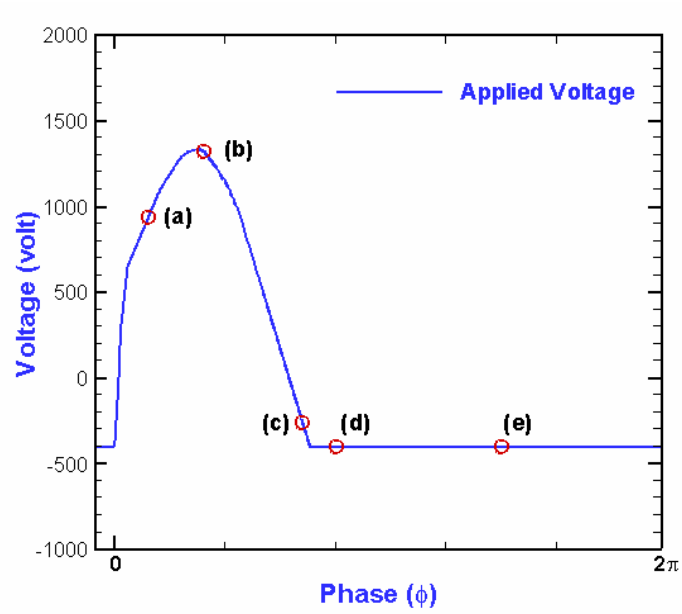
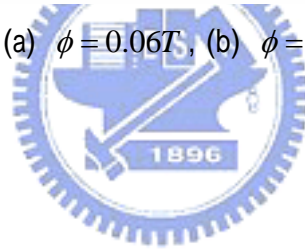


Figure 4.6. Applied voltage in (a) $\phi = 0.06T$, (b) $\phi = 0.16T$, (c) $\phi = 0.34T$, (d) $\phi = 0.40T$, (e) $\phi = 0.70T$.



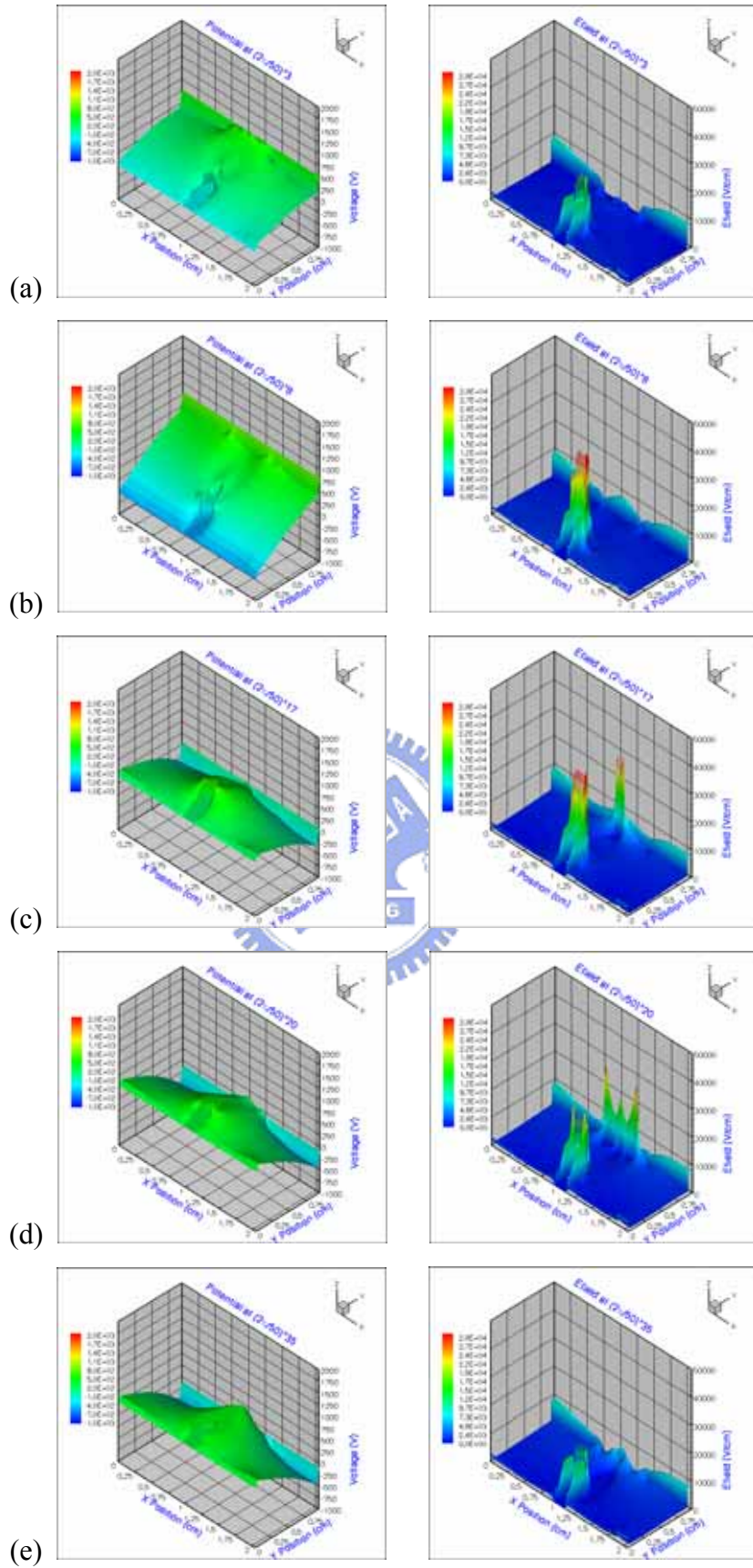


Figure 4.7. Potential and electric field in (a) $\phi = 0.06T$, (b) $\phi = 0.16T$, (c) $\phi = 0.34T$, (d) $\phi = 0.40T$, (e) $\phi = 0.70T$.

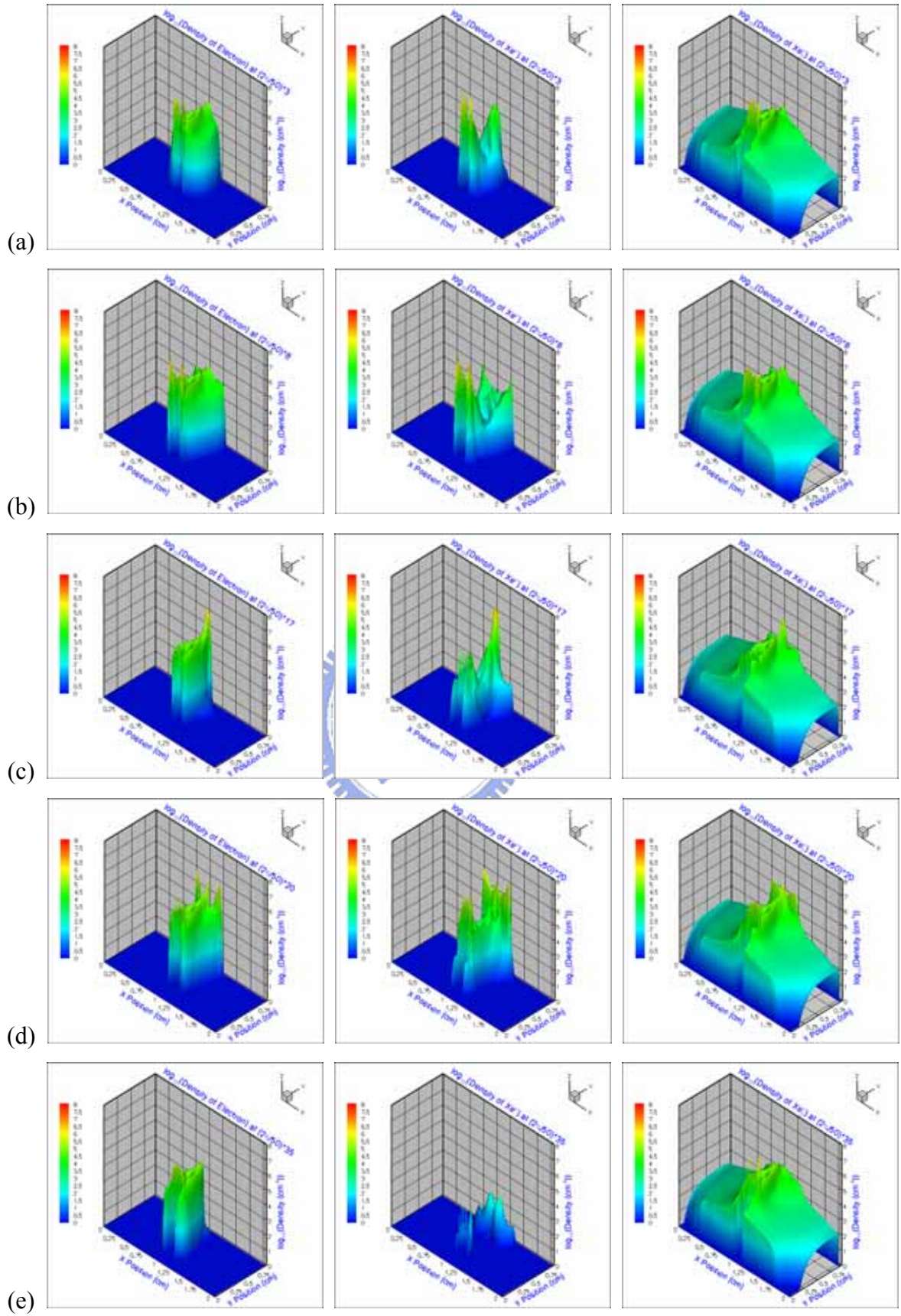


Figure 4.8. Densities of charged species, e^- , Xe^+ , and Xe_2^+ in (a) $\phi = 0.06T$, (b) $\phi = 0.16T$, (c) $\phi = 0.34T$, (d) $\phi = 0.40T$, (e) $\phi = 0.70T$.

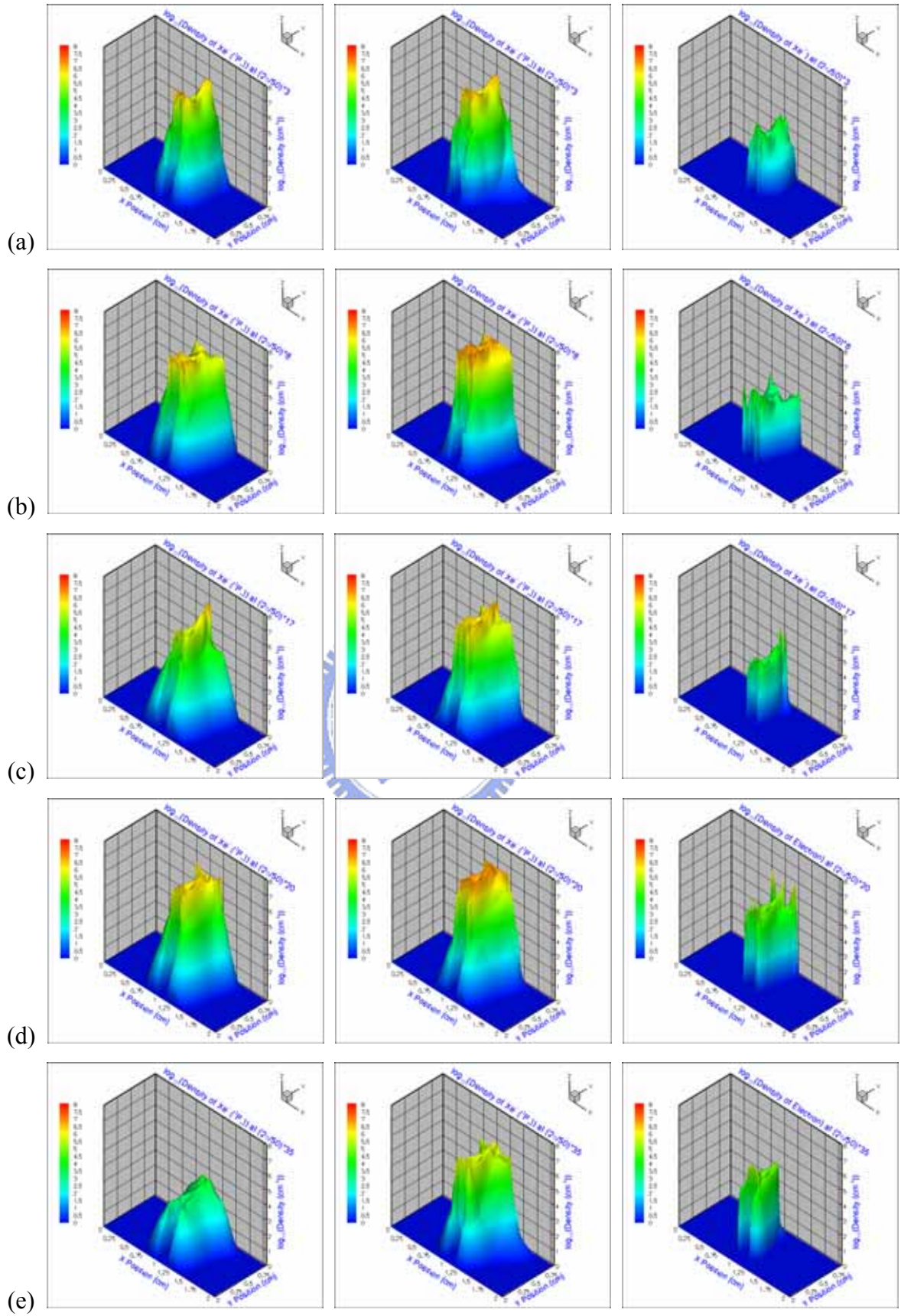


Figure 4.9. Densities of excited species , $\text{Xe}^*(^3\text{P}_1)$, $\text{Xe}^*(^3\text{P}_2)$, and Xe^{**} , in (a) $\phi = 0.06T$, (b) $\phi = 0.16T$, (c) $\phi = 0.34T$, (d) $\phi = 0.40T$, (e) $\phi = 0.70T$.

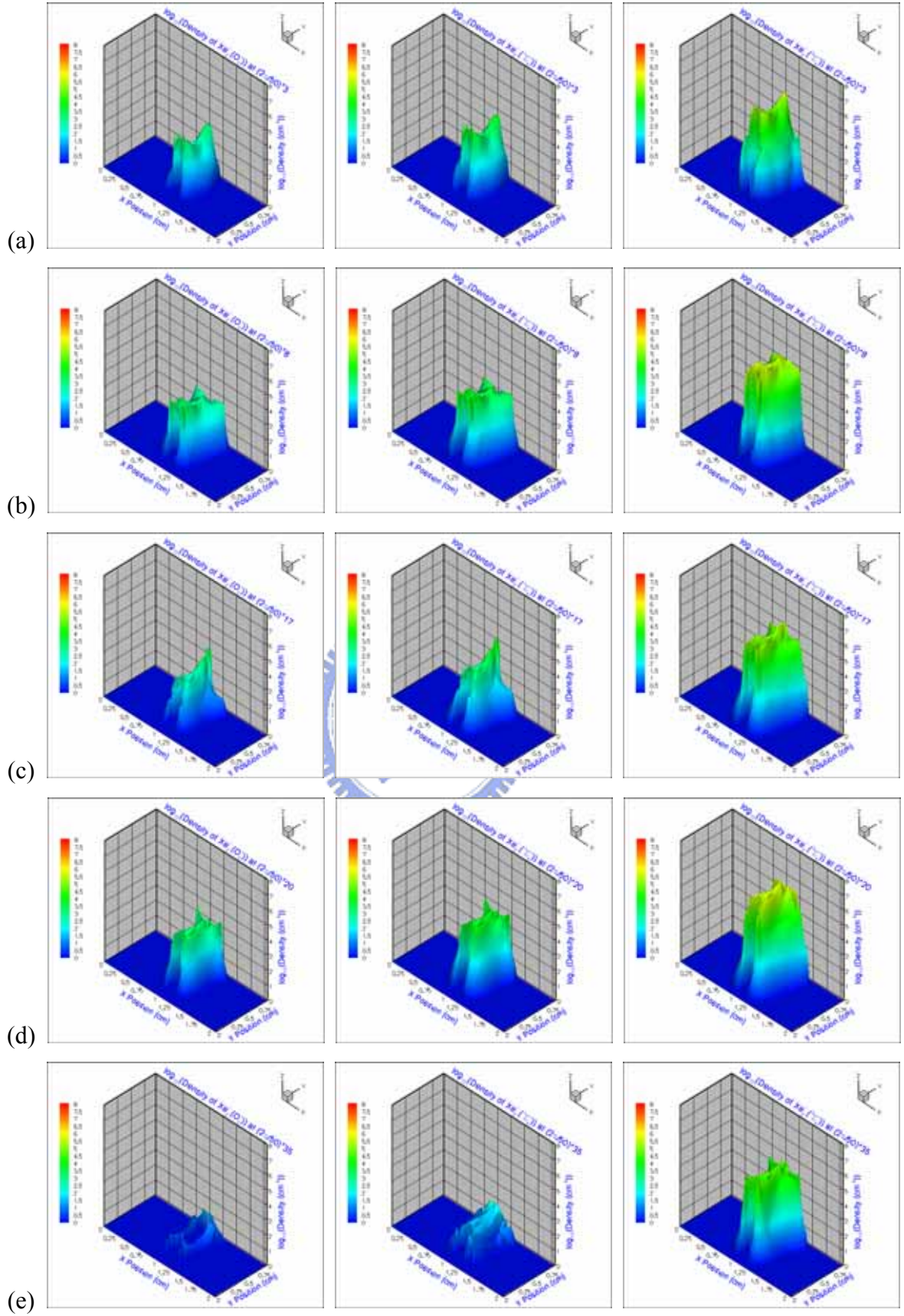


Figure 4.10. Densities of excited species, $\text{Xe}_2^*(O_u^+)$, $\text{Xe}_2^*({}^1\Sigma_u^+)$, and $\text{Xe}_2^*({}^3\Sigma_u^+)$ in (a) $\phi = 0.06T$, (b) $\phi = 0.16T$, (c) $\phi = 0.34T$, (d) $\phi = 0.40T$, (e) $\phi = 0.70T$.

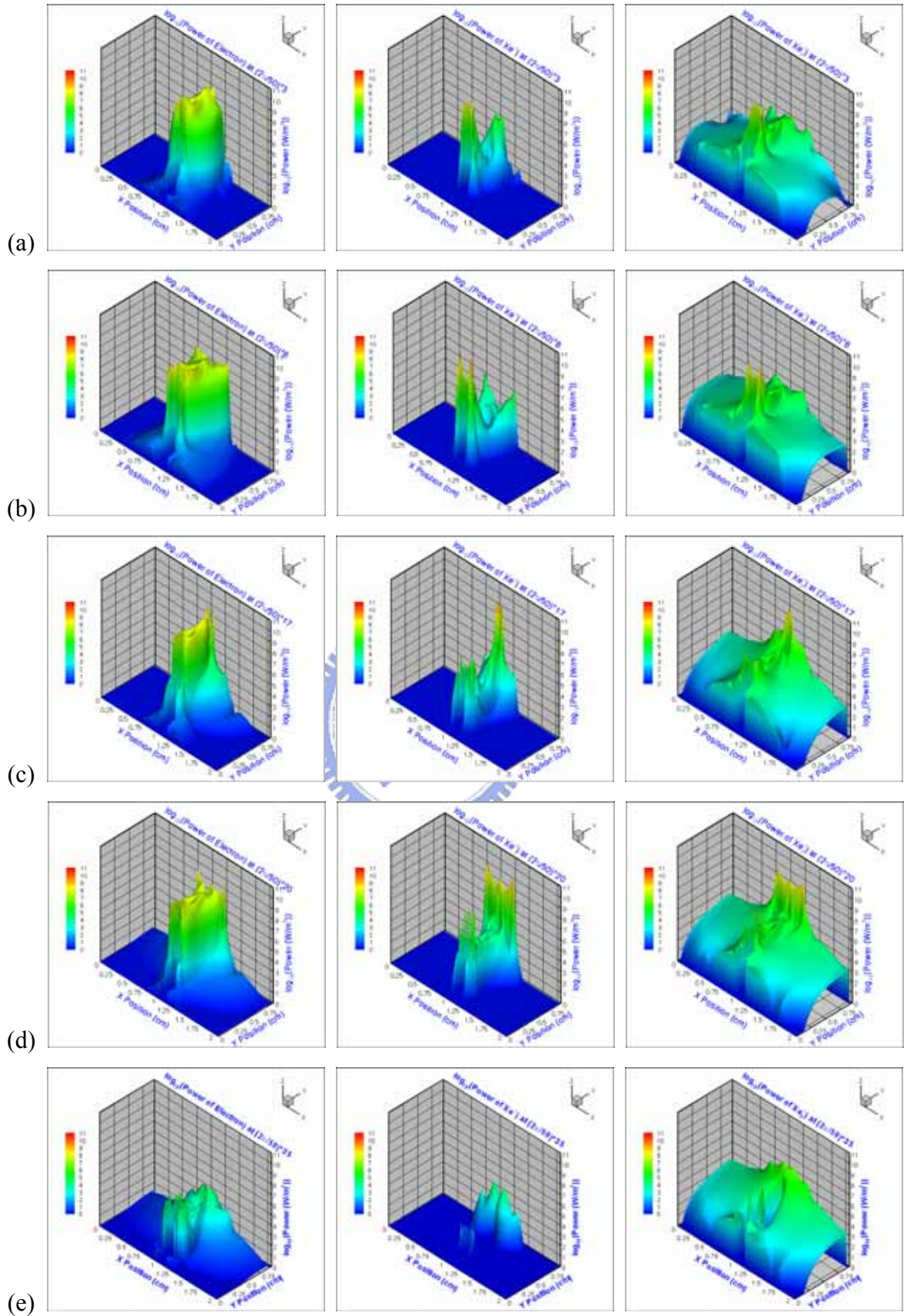


Figure 4.11. Powers of charged species in (a) $\phi = 0.06T$, (b) $\phi = 0.16T$, (c) $\phi = 0.34T$, (d) $\phi = 0.40T$, (e) $\phi = 0.70T$.

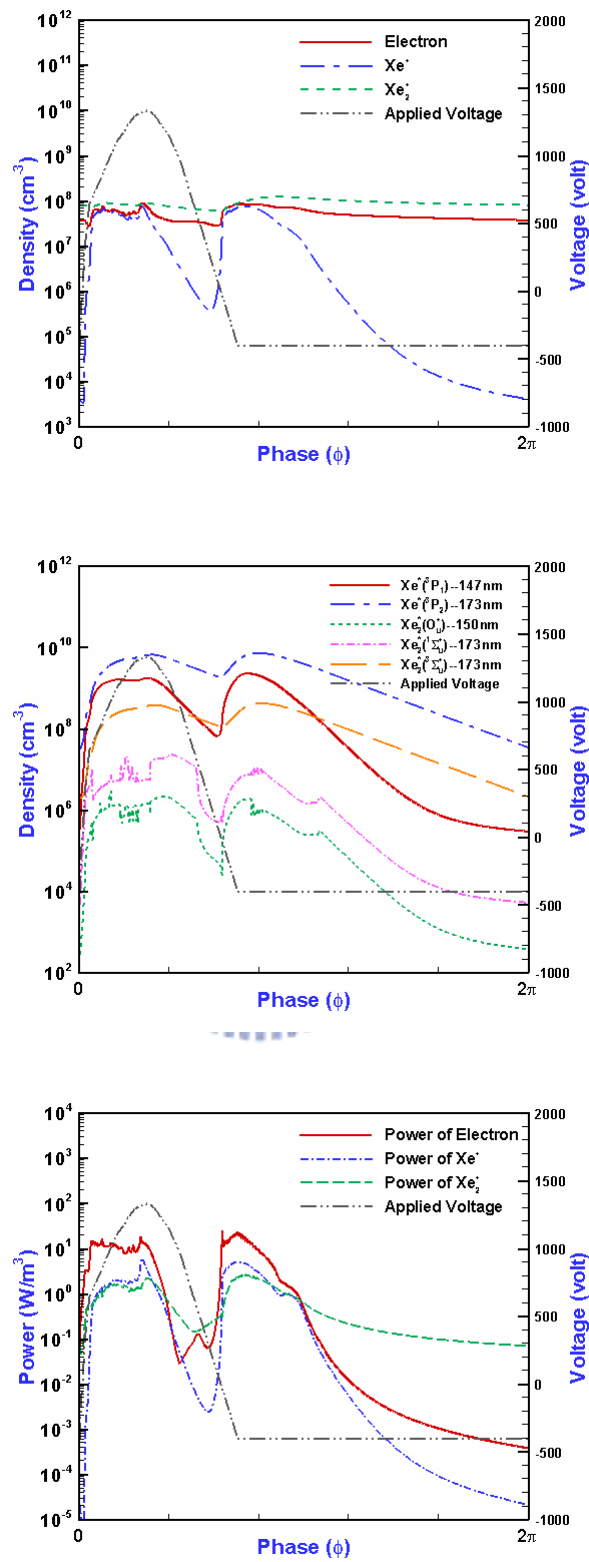


Figure 4.12. Time evolutions of the spatially averaged quantities @ $f=55\text{kHz}$, $V_a = 1740\text{V}$, duty ratio=35%, $P=90\text{torr}$, $T=350\text{K}$

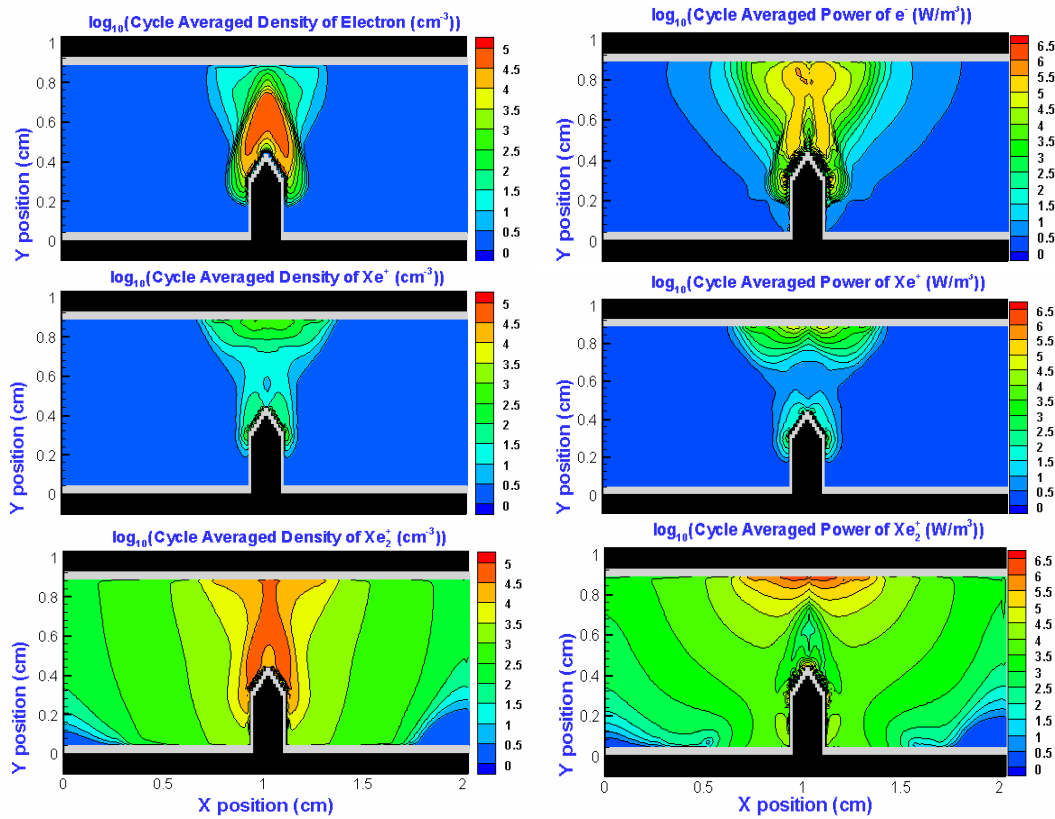


Figure 4.13. Cycle averaged quantities of charged species @ $f=55\text{kHz}$, $V_a=1740\text{V}$, duty ratio=35%, $P=90\text{torr}$, $T=350\text{K}$

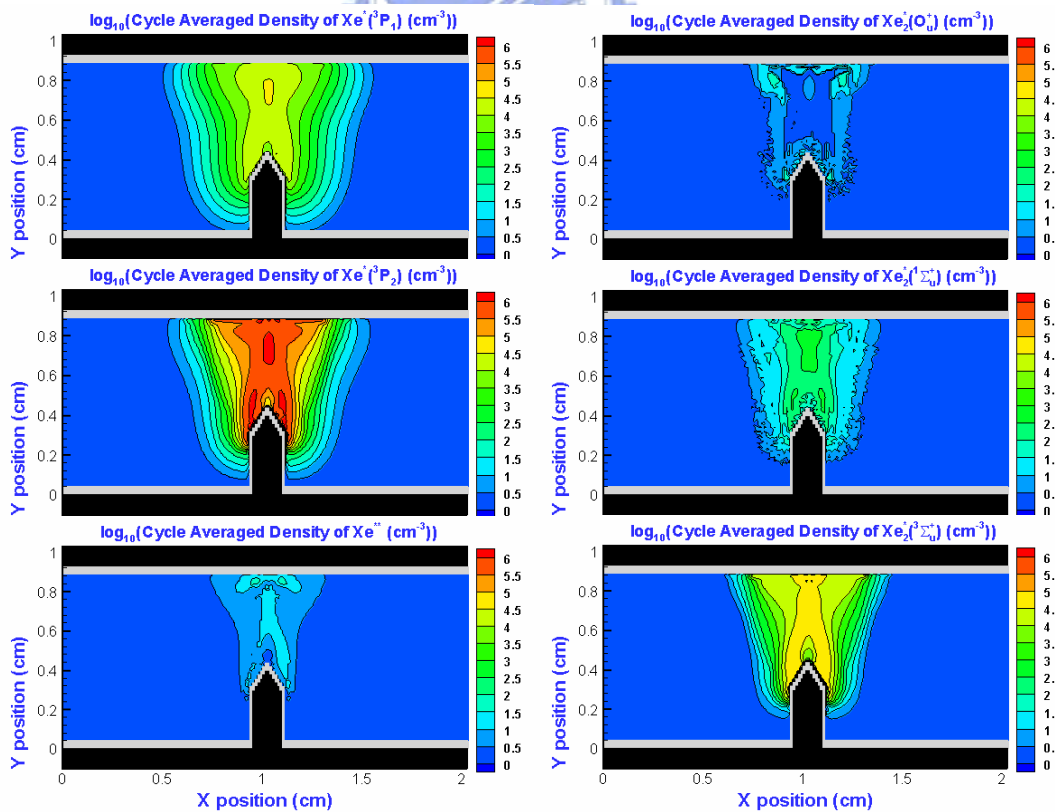


Figure 4.14. Cycle averaged quantities of excited species @ f 55kHz, V_a 1740V, duty ratio 35%, P 90torr, T 350K.

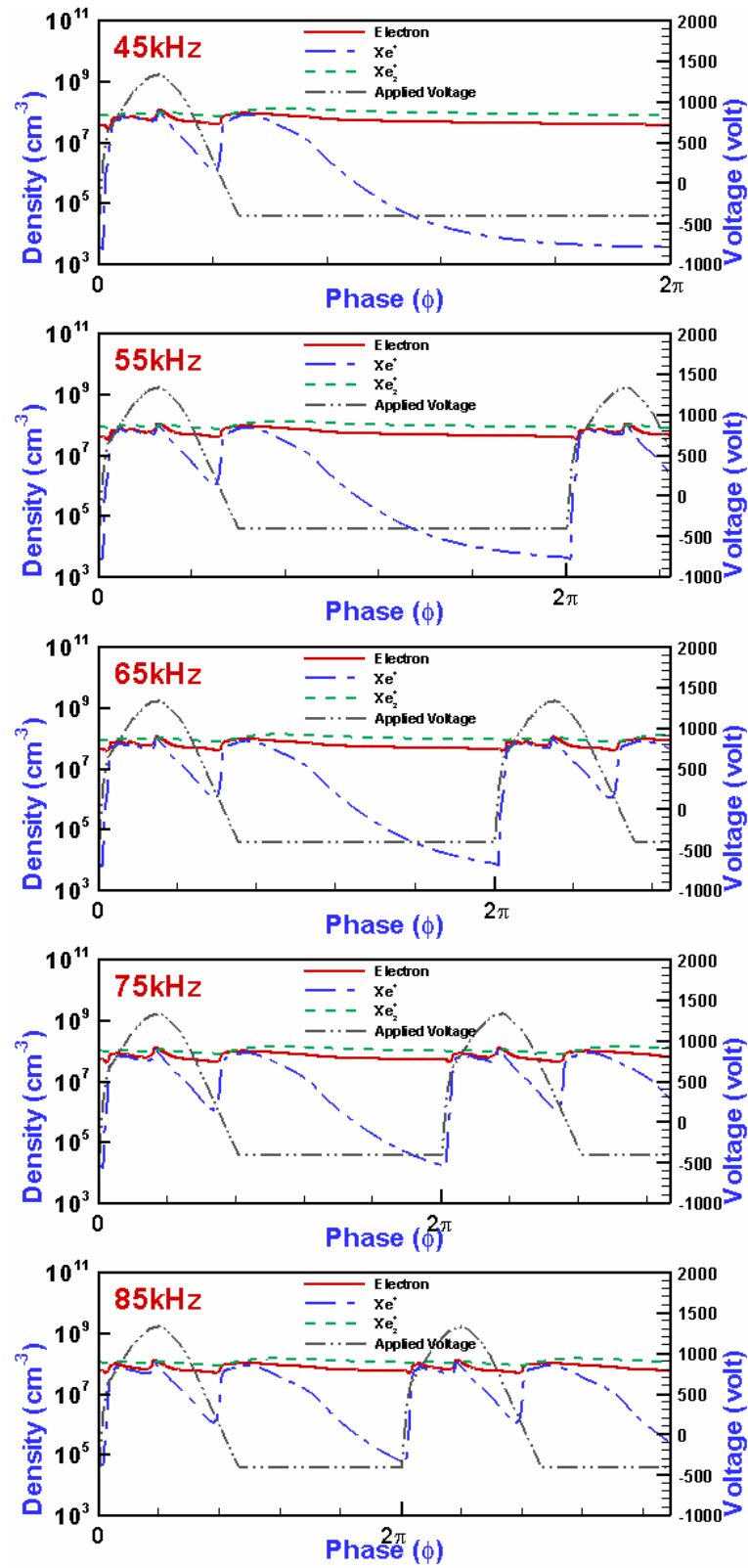


Figure 4.15. Time evolutions of the spatially averaged densities of charged species versus pulse frequency 45~85kHz.

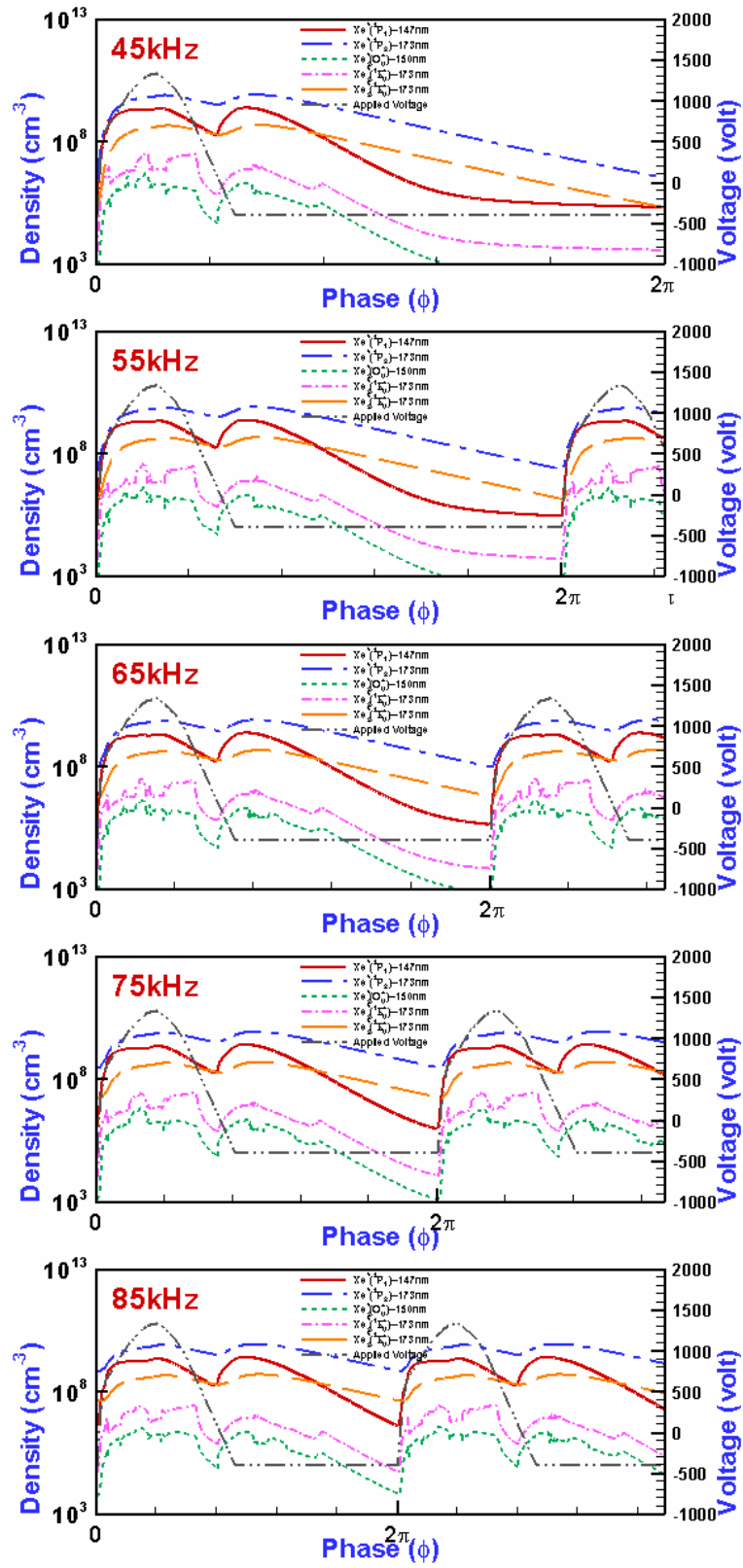


Figure 4.16. Time evolutions of the spatially averaged densities of excited species versus pulse frequency 45~85kHz.

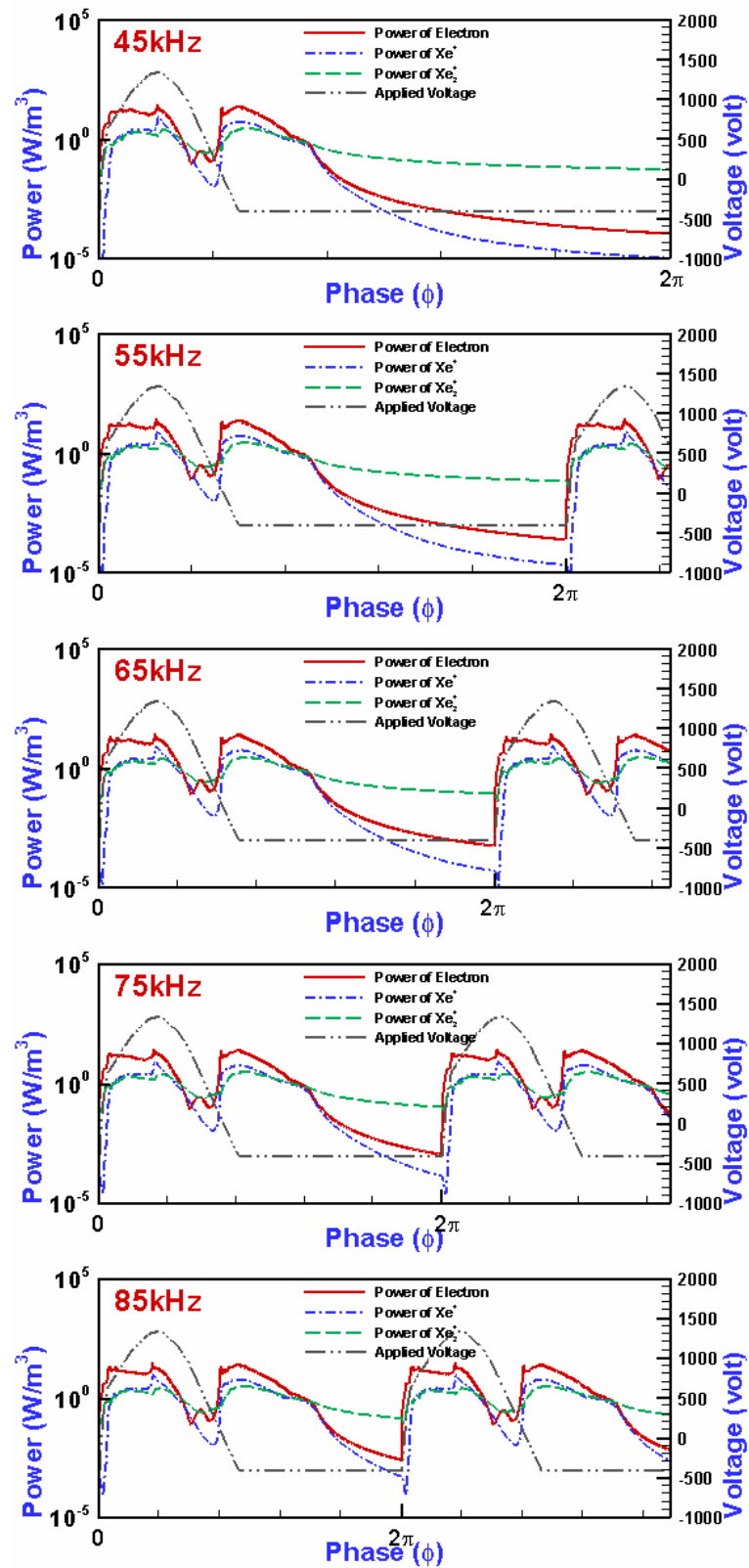


Figure 4.17. Time evolutions of the spatially averaged powers of charged species versus pulse frequency 45~85kHz.

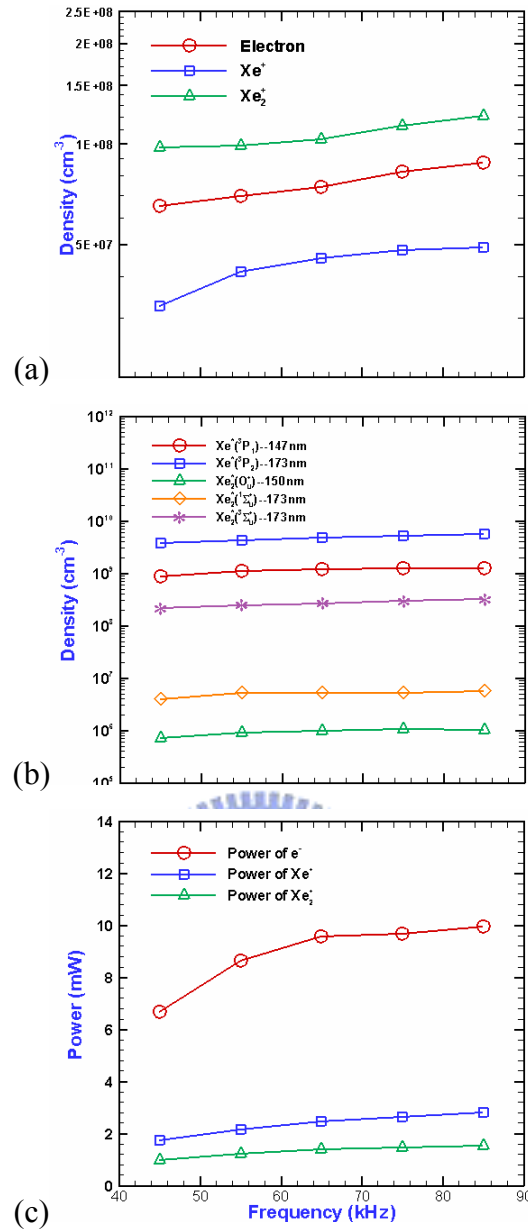


Figure 4.18. The averaged quantities (a) charged species densities, (b) excited species densities, and (c) charged species powers versus pulse frequency 45~85kHz.

Table 4. Details of averaged quantities versus pulse frequency 45~85kHz.

f (kHz)	e ⁻ (%)	Xe ⁺ (%)	Xe ₂ ⁺ (%)	Xe ⁺ (³ P ₁) (%)	Xe ⁺ (³ P ₂) (%)	Xe ₂ ⁺ (³ O _u ⁺) (%)	Xe ₂ ⁺ (³ Σ _u ⁺) (%)	Xe ₂ ⁺ (³ Σ _u ⁺) (%)	Power of e ⁻ (%)	Power of Xe ⁺ (%)	Power of Xe ₂ ⁺ (%)
45	100.00	100.00	100.00	100.00	100.00	100.00	100.00	100.00	100.00	100.00	100.00
55	107.01	127.15	100.86	126.11	116.50	129.58	130.99	115.32	129.01	125.15	121.44
65	114.19	139.56	105.24	134.89	127.74	136.12	132.89	126.43	142.98	143.10	138.14
75	127.08	147.28	116.04	138.45	140.59	152.80	133.45	140.29	144.65	152.23	146.29
85	134.63	150.21	123.82	140.54	148.55	146.76	144.23	148.61	148.37	162.02	153.61
Quantity at 45 kHz	6.52E+07 (cm ⁻³)	3.26E+07 (cm ⁻³)	9.80E+07 (cm ⁻³)	9.05E+08 (cm ⁻³)	3.82E+09 (cm ⁻³)	7.24E+05 (cm ⁻³)	4.03E+06 (cm ⁻³)	2.18E+08 (cm ⁻³)	6.71 (mW)	1.75 (mW)	1.02 (mW)

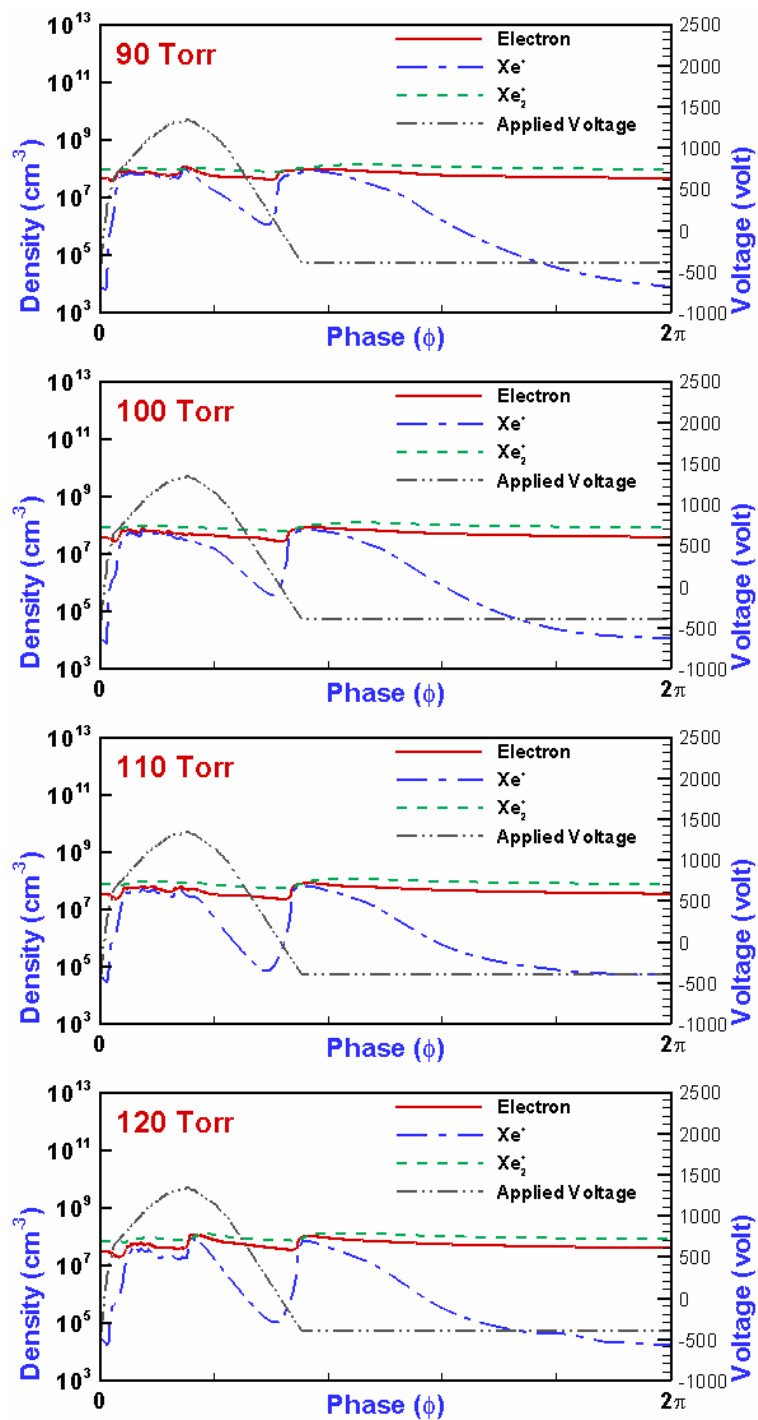


Figure 4.19. Time evolutions of the spatially averaged densities of charged species versus gas pressure 90~120Torr.

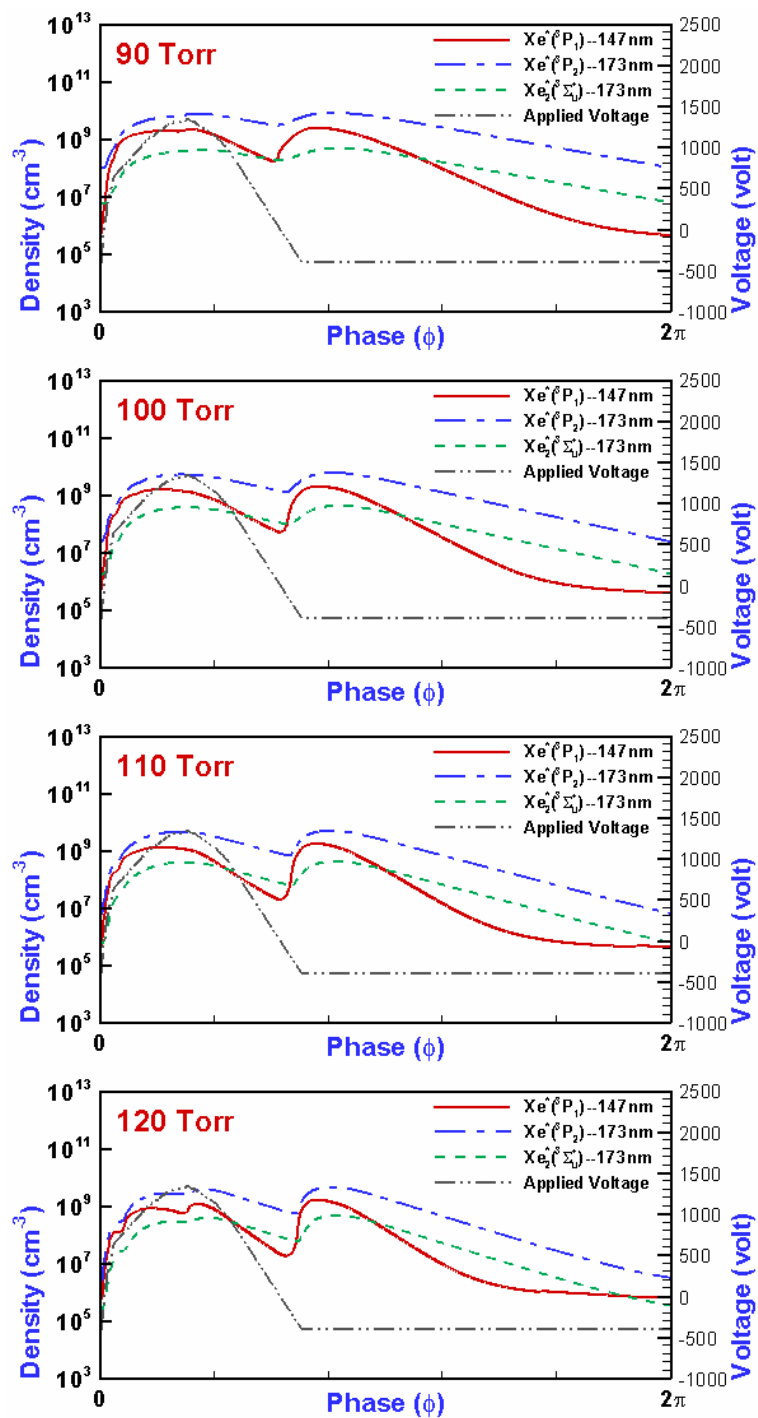


Figure 4.20. Time evolutions of the spatially averaged densities of excited species versus gas pressure 90~120Torr.

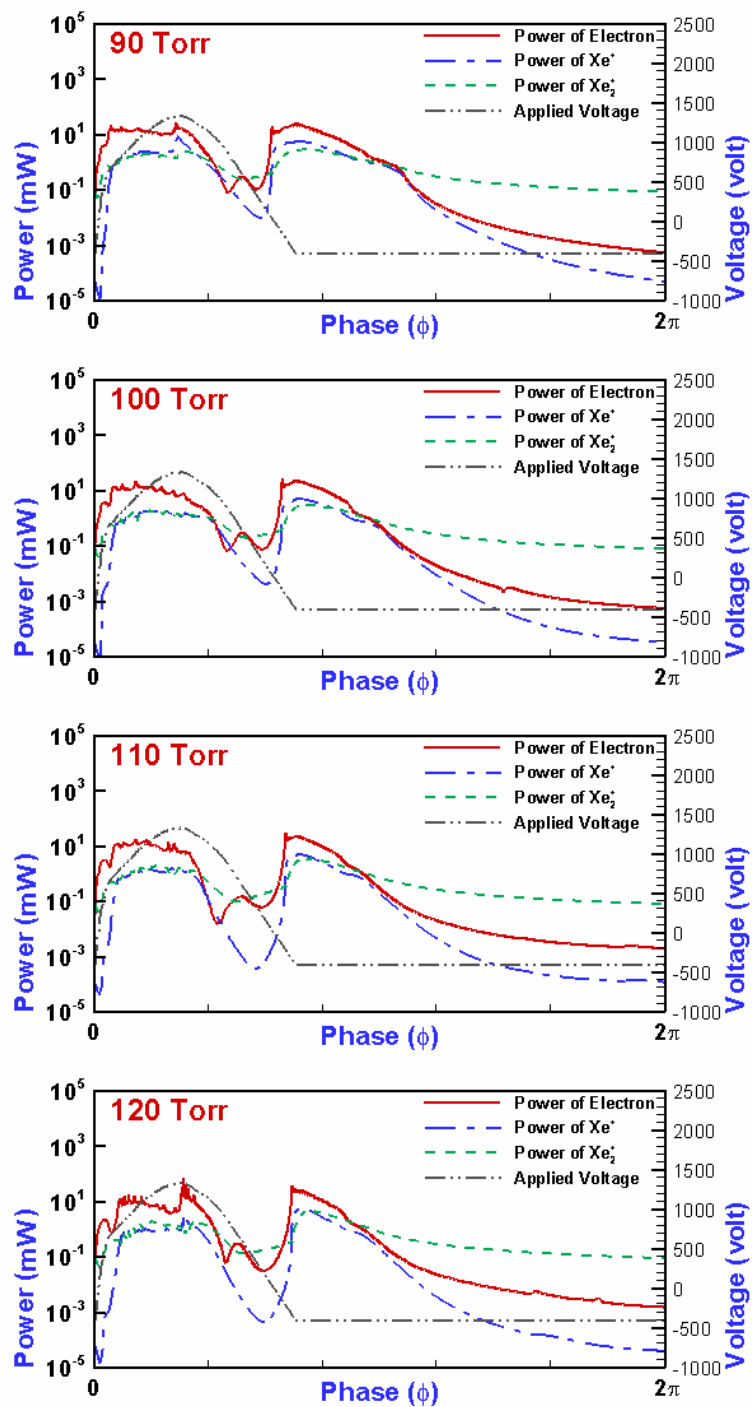


Figure 4.21. Time evolutions of the spatially averaged powers of charged species versus gas pressure 90~120Torr.

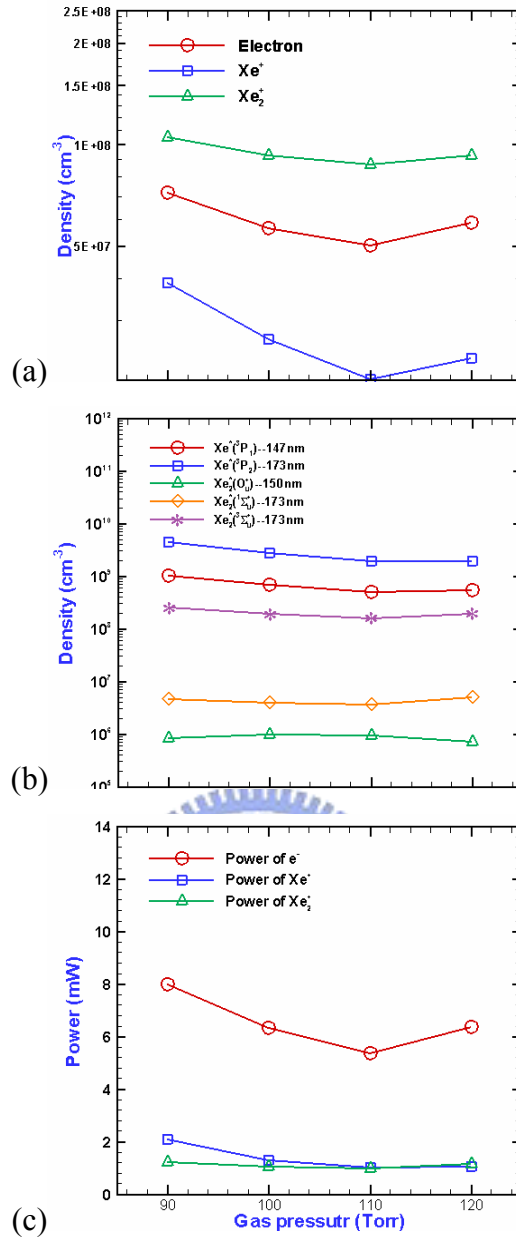


Figure 4.22. The averaged quantities (a) charged species densities, (b) excited species densities, and (c) charged species powers versus gas pressure 90~120 Torr.

Table 5. Details of averaged quantities versus gas pressure 90~120 Torr.

Pressure (Torr)	e ⁻ (%)	Xe ⁺ (%)	Xe ₂ ⁺ (%)	Xe [*] (P ₁) (%)	Xe [*] (P ₂) (%)	Xe ₂ [*] (O _u ⁺) (%)	Xe ₂ [*] (Σ _u ⁺) (%)	Xe ₂ [*] (Σ _u ⁺) (%)	Power of e ⁻ (%)	Power of Xe ⁺ (%)	Power of Xe ₂ ⁺ (%)
90	163.11	194.40	120.31	205.53	232.23	88.35	125.30	158.01	148.38	207.22	126.33
100	136.88	132.09	106.67	134.42	142.96	102.68	106.70	119.09	117.70	128.93	107.34
110	129.96	100.00	100.00	100.00	100.00	100.00	100.00	100.00	100.00	100.00	100.00
120	115.12	116.01	106.72	105.70	102.58	75.29	139.01	121.02	118.52	104.02	120.11
Quantity at 110 Torr	5.03E+07 (cm ⁻³)	2.01E+07 (cm ⁻³)	8.75E+07 (cm ⁻³)	5.17E+08 (cm ⁻³)	1.95E+09 (cm ⁻³)	9.60E+05 (cm ⁻³)	3.72E+06 (cm ⁻³)	1.64E+08 (cm ⁻³)	5.40 (mW)	1.02 (mW)	0.98 (mW)

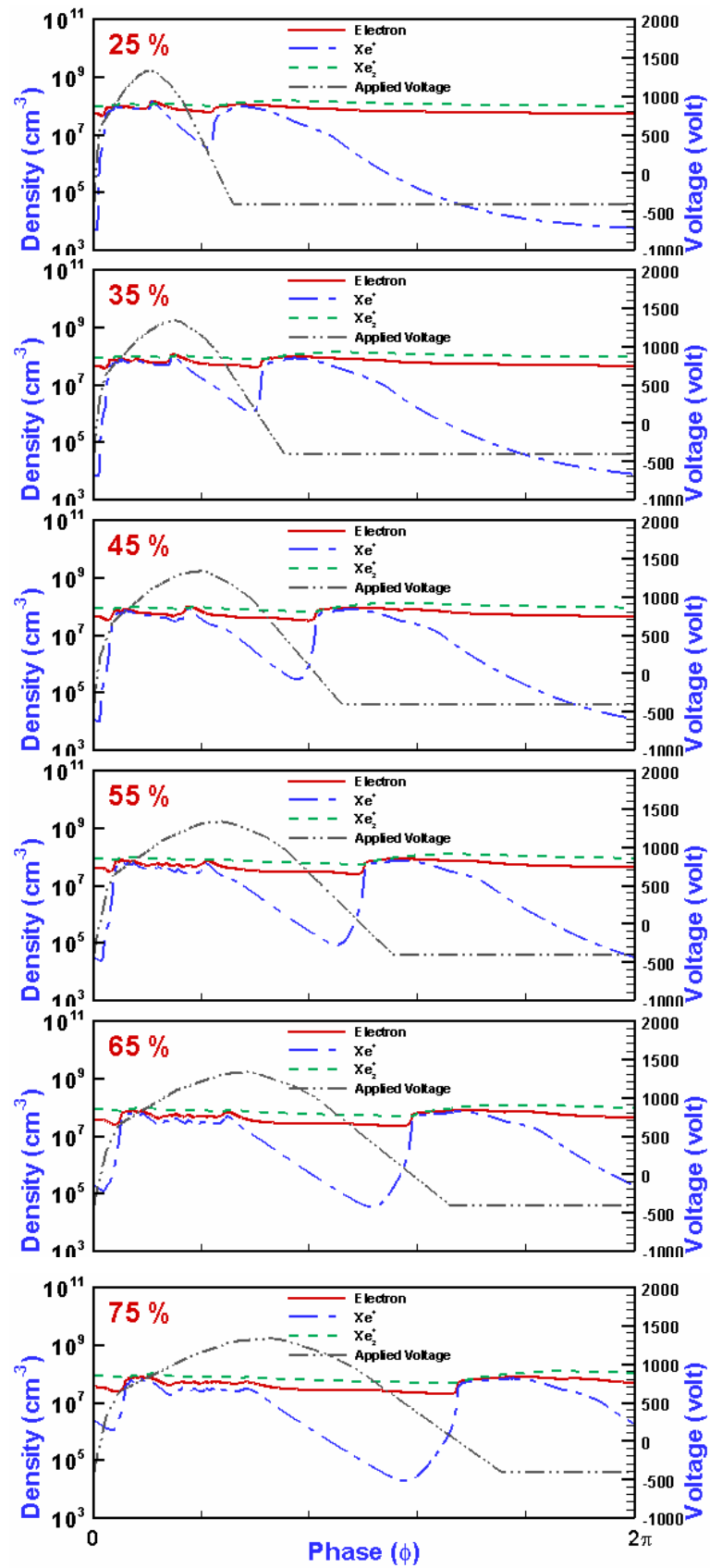


Figure 4.23. Time evolutions of the spatially averaged densities of charged species versus duty ratio 25~75%.

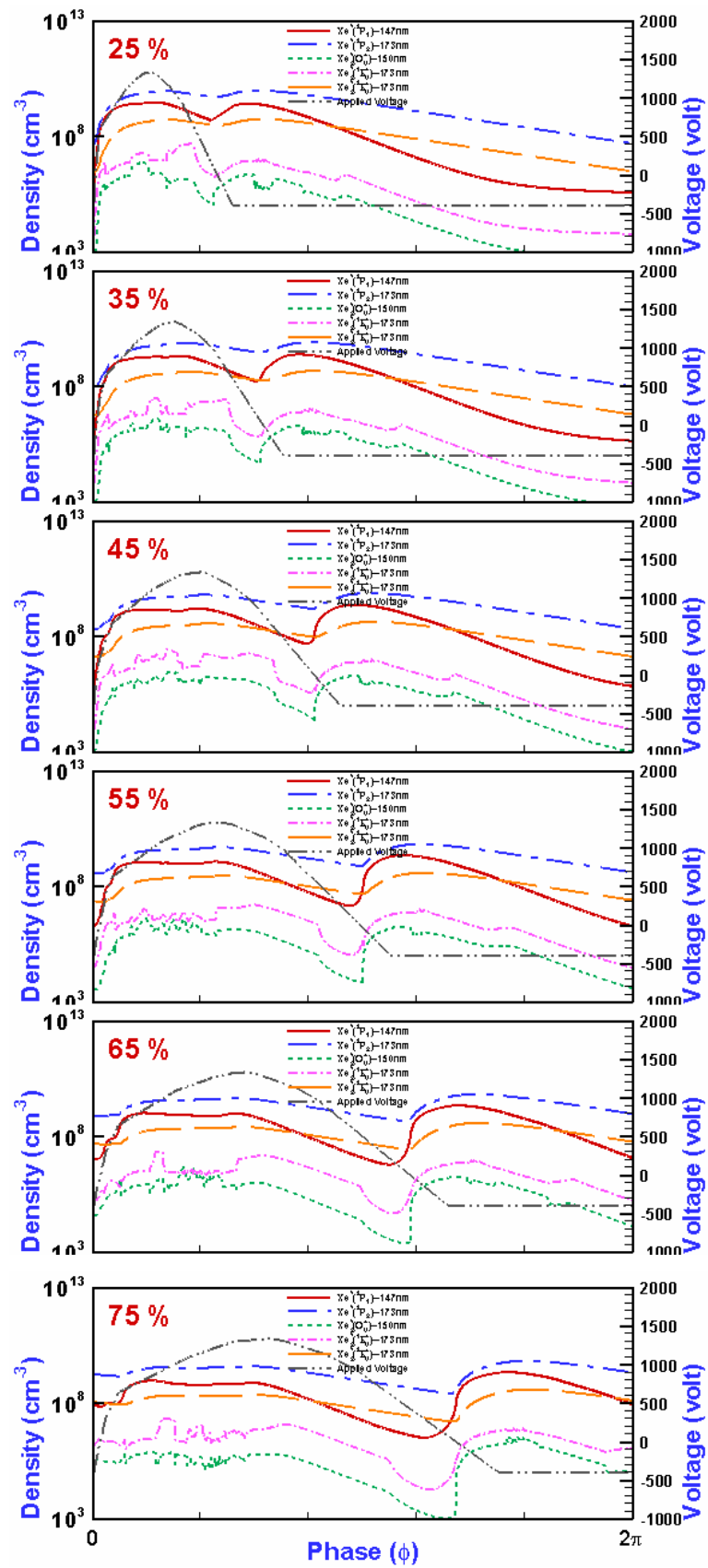


Figure 4.24. Time evolutions of the spatially averaged densities of excited species versus duty ratio 25~75%.

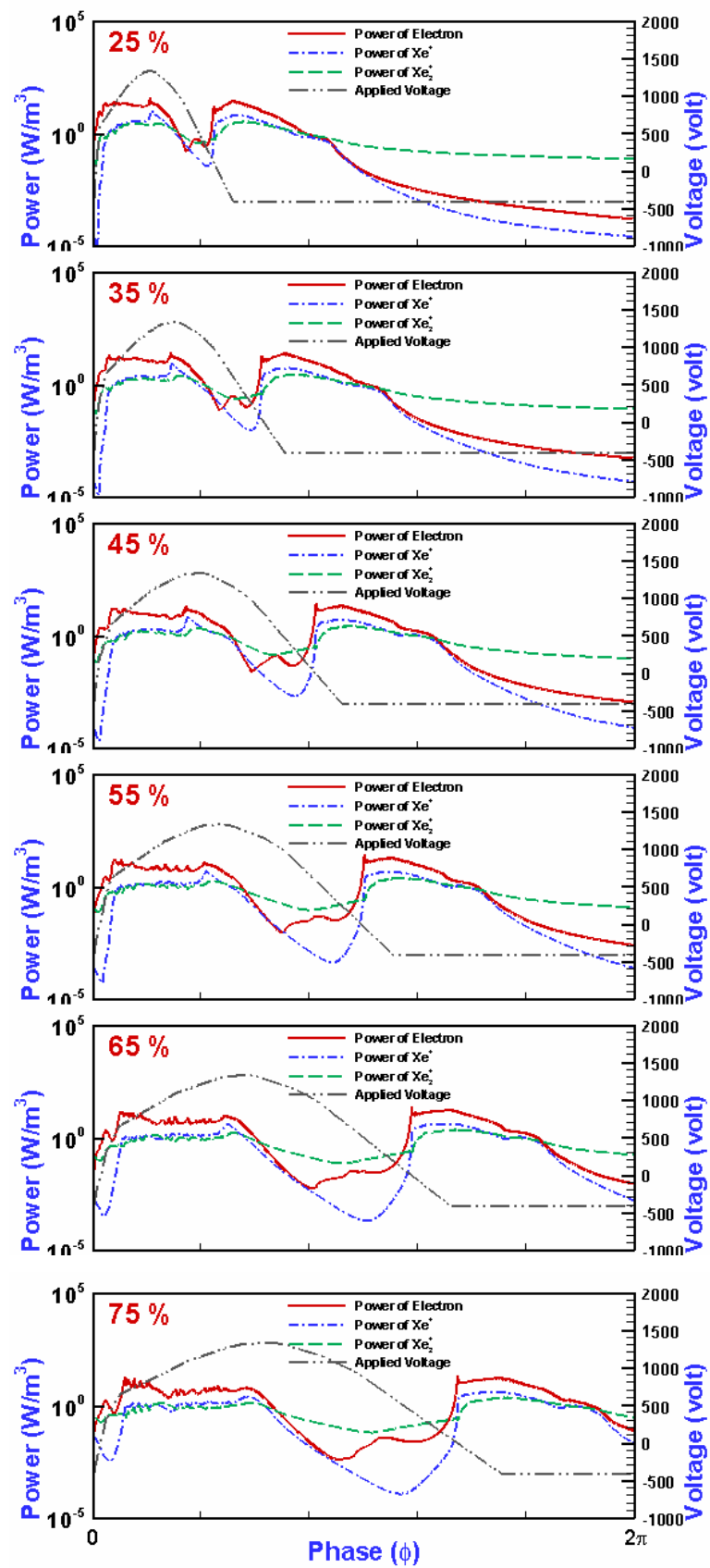


Figure 4.25. Time evolutions of the spatially averaged powers of charged species versus duty ratio 25~75%.

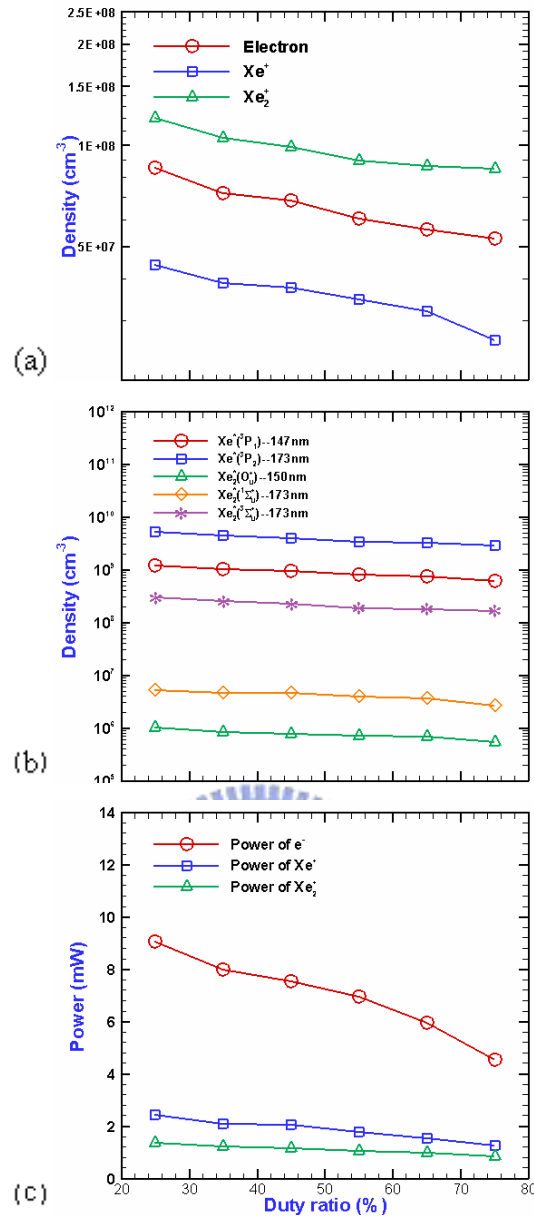


Figure 4.26. The averaged quantities (a) charged species densities, (b) excited species densities, and (c) charged species powers versus duty ratio 25~75%.

Table 6. Details of averaged quantities versus duty ratio 25~75%.

Duty ratio (%)	e ⁻ (%)	Xe ⁺ (%)	Xe ₂ ⁺ (%)	Xe ⁺ (³ P ₁) (%)	Xe ⁺ (³ P ₂) (%)	Xe ₂ ⁺ (O _u ⁺) (%)	Xe ₂ ⁺ (¹ Σ _u ⁺) (%)	Xe ₂ ⁺ (³ Σ _u ⁺) (%)	Power of e ⁻ (%)	Power of Xe ⁺ (%)	Power of Xe ₂ ⁺ (%)
25	163.11	167.36	141.96	198.80	178.66	188.74	195.15	177.10	199.57	194.56	158.23
35	136.88	147.96	123.85	169.90	154.40	152.95	173.99	152.97	176.08	167.17	142.06
45	129.96	143.15	116.70	151.85	137.96	142.81	174.46	136.28	166.73	162.77	134.84
55	115.12	132.27	105.74	133.18	115.60	130.98	149.94	113.25	153.57	142.84	122.83
65	106.43	121.37	102.36	123.11	111.04	127.20	140.23	109.66	131.44	123.09	114.19
75	100.00	100.00	100.00	100.00	100.00	100.00	100.00	100.00	100.00	100.00	100.00
Quantity at 75 %	5.28E+07 (cm-3)	2.64E+07 (cm-3)	8.51E+07 (cm-3)	6.26E+08 (cm ⁻³)	2.94E+09 (cm ⁻³)	5.58E+05 (cm ⁻³)	2.67E+06 (cm ⁻³)	1.69E+08 (cm ⁻³)	4.54 (mW)	1.27 (mW)	0.88 (mW)

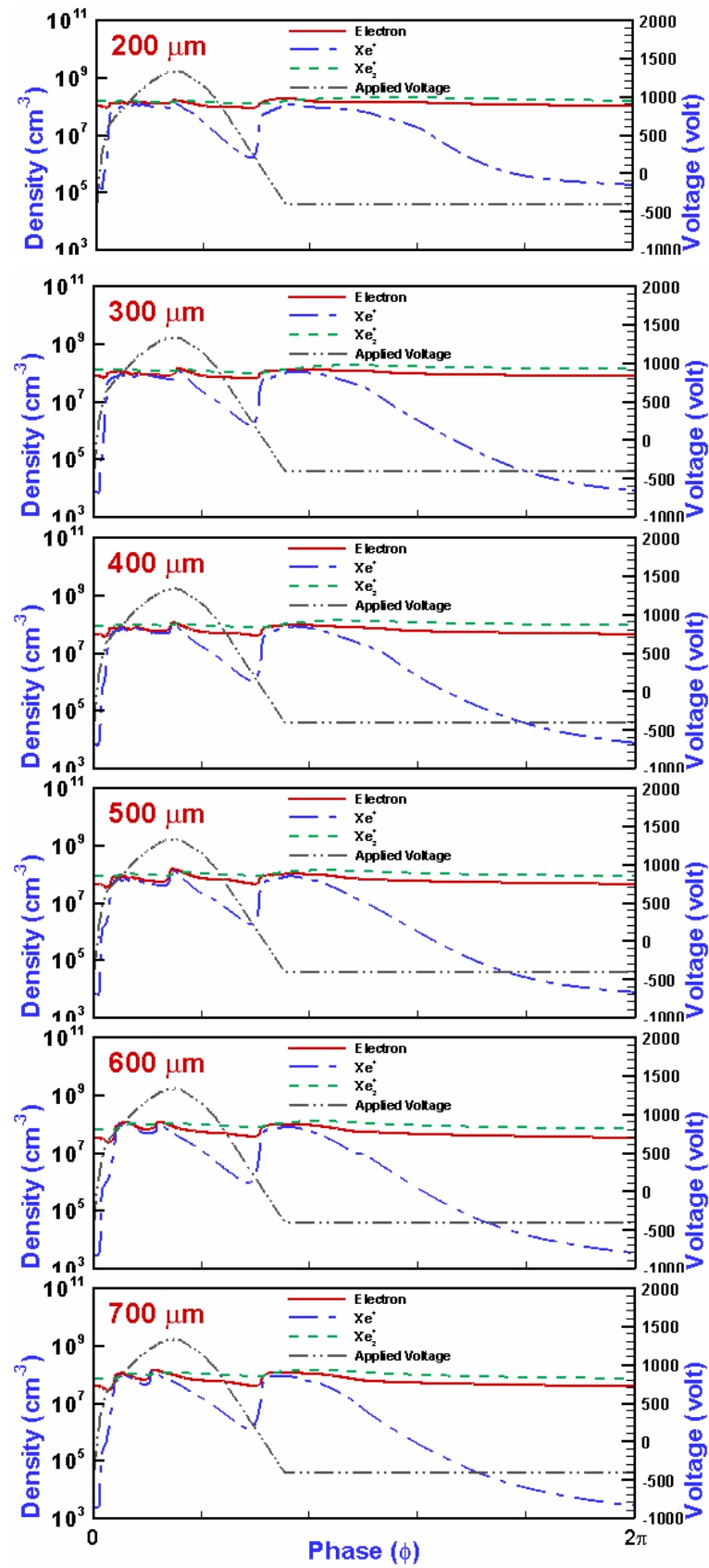


Figure 4.27. Time evolutions of the spatially averaged densities of charged species versus dielectric thickness 200~700 μm .

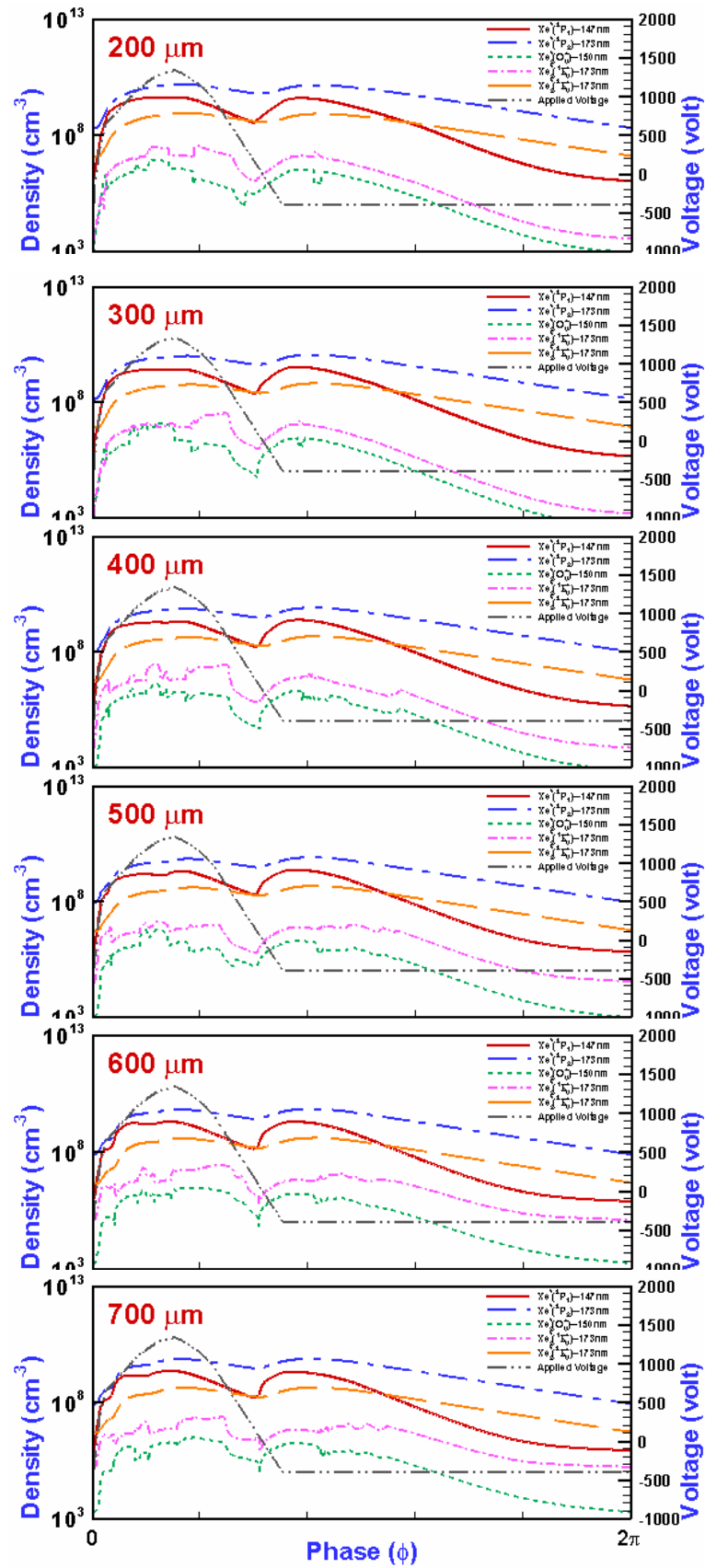


Figure 4.28. Time evolutions of the spatially averaged densities of excited species versus dielectric thickness 200~700μm

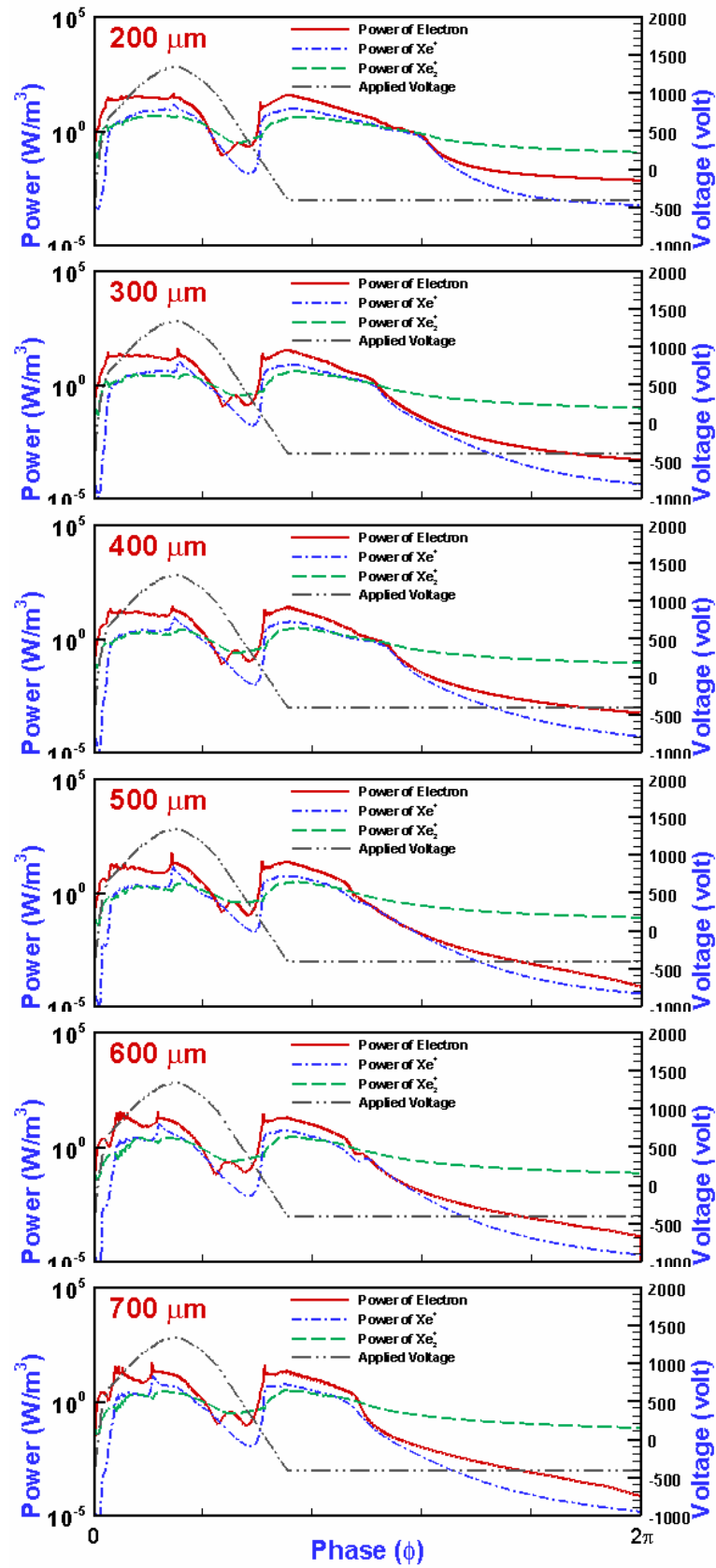


Figure 4.29. Time evolutions of the spatially averaged powers of charged species versus dielectric thickness 200~700 μm .

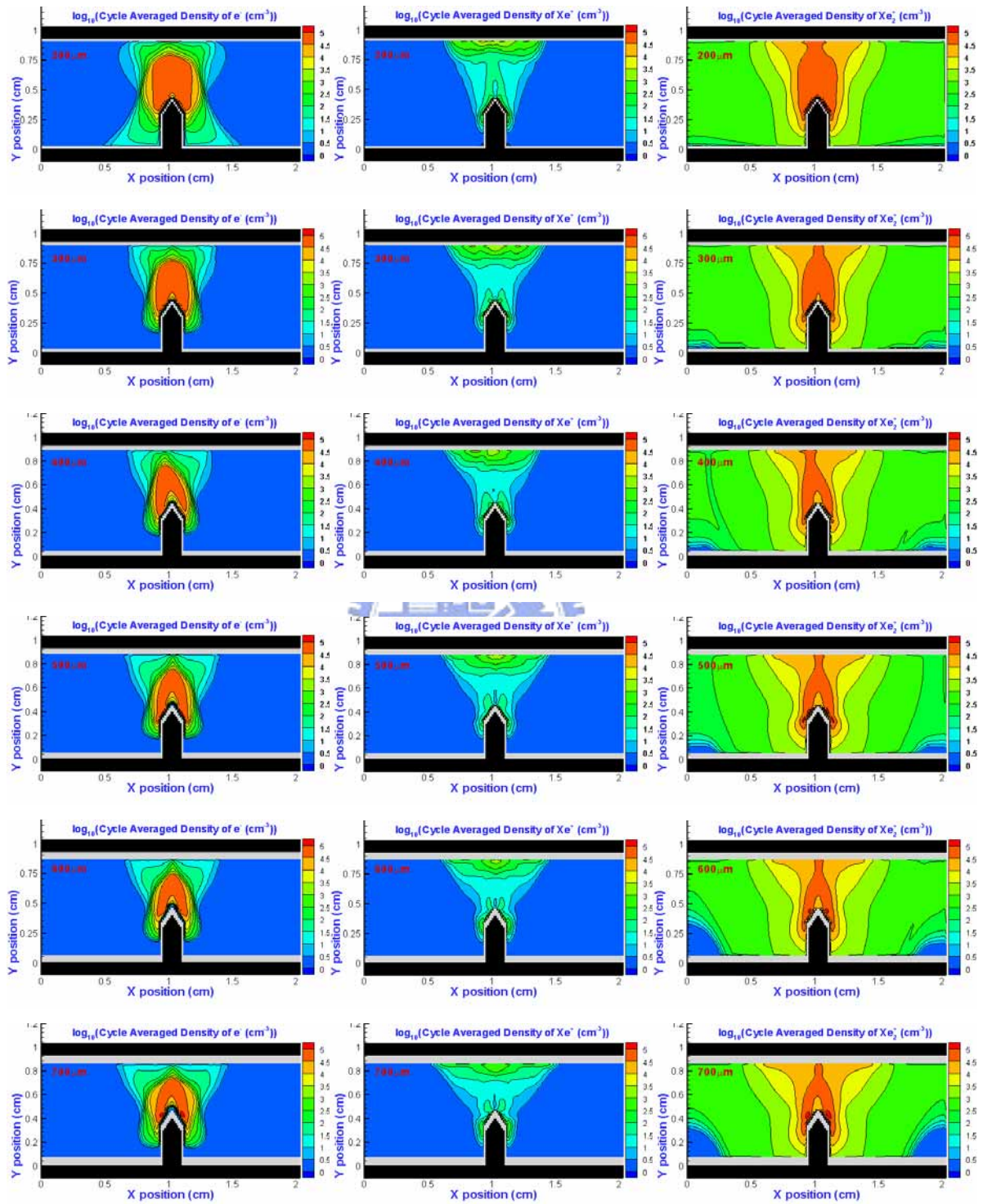


Figure 4.30. Cycle averaged densities of charged species, e^- , Xe^+ , and Xe_2^+ versus dielectric thickness 200~700 μm .

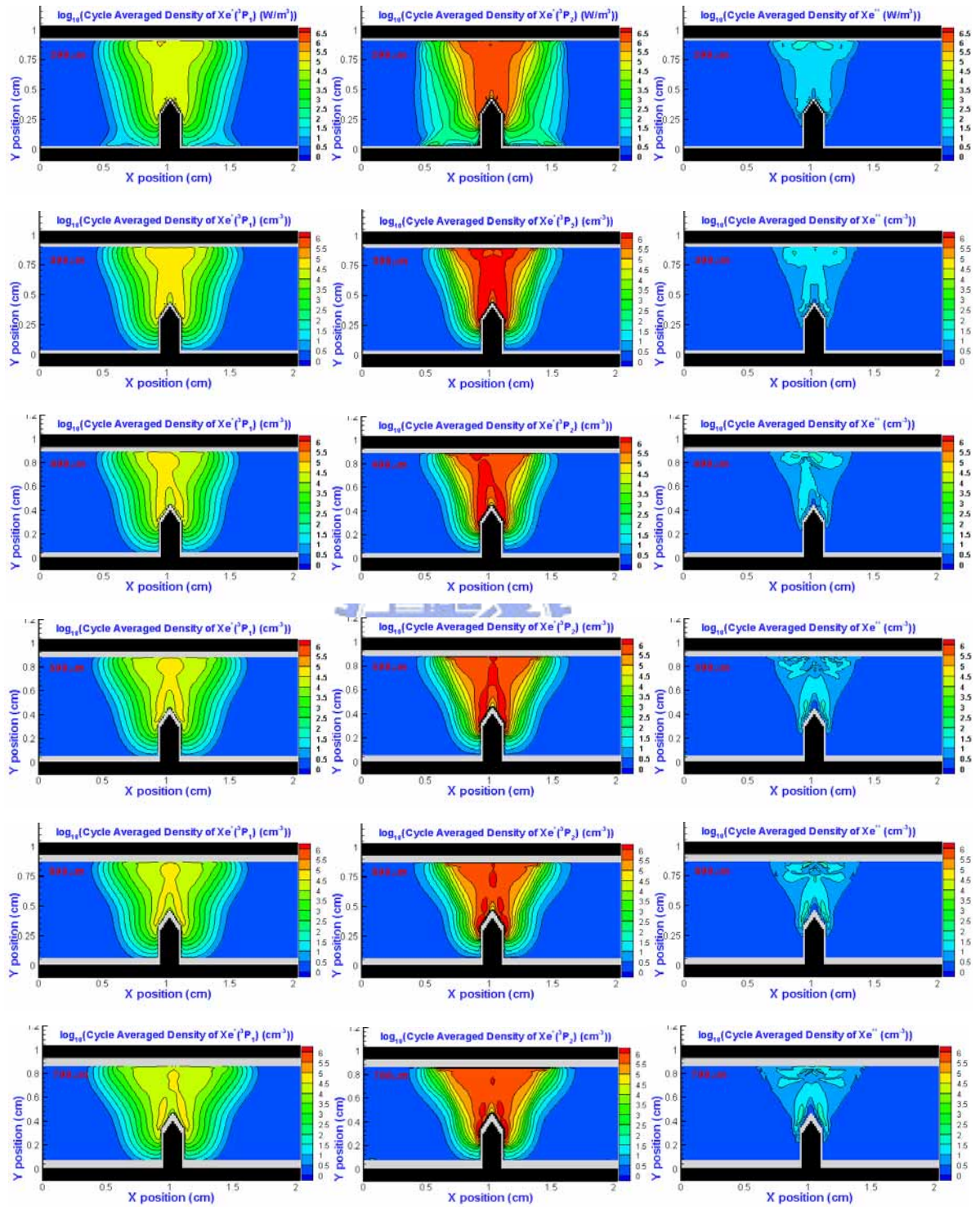


Figure 4.31. Cycle averaged densities of excited species, $\text{Xe}^*(^3\text{P}_1)$, $\text{Xe}^*(^3\text{P}_2)$, and Xe^{**} versus dielectric thickness 200~700 μm .

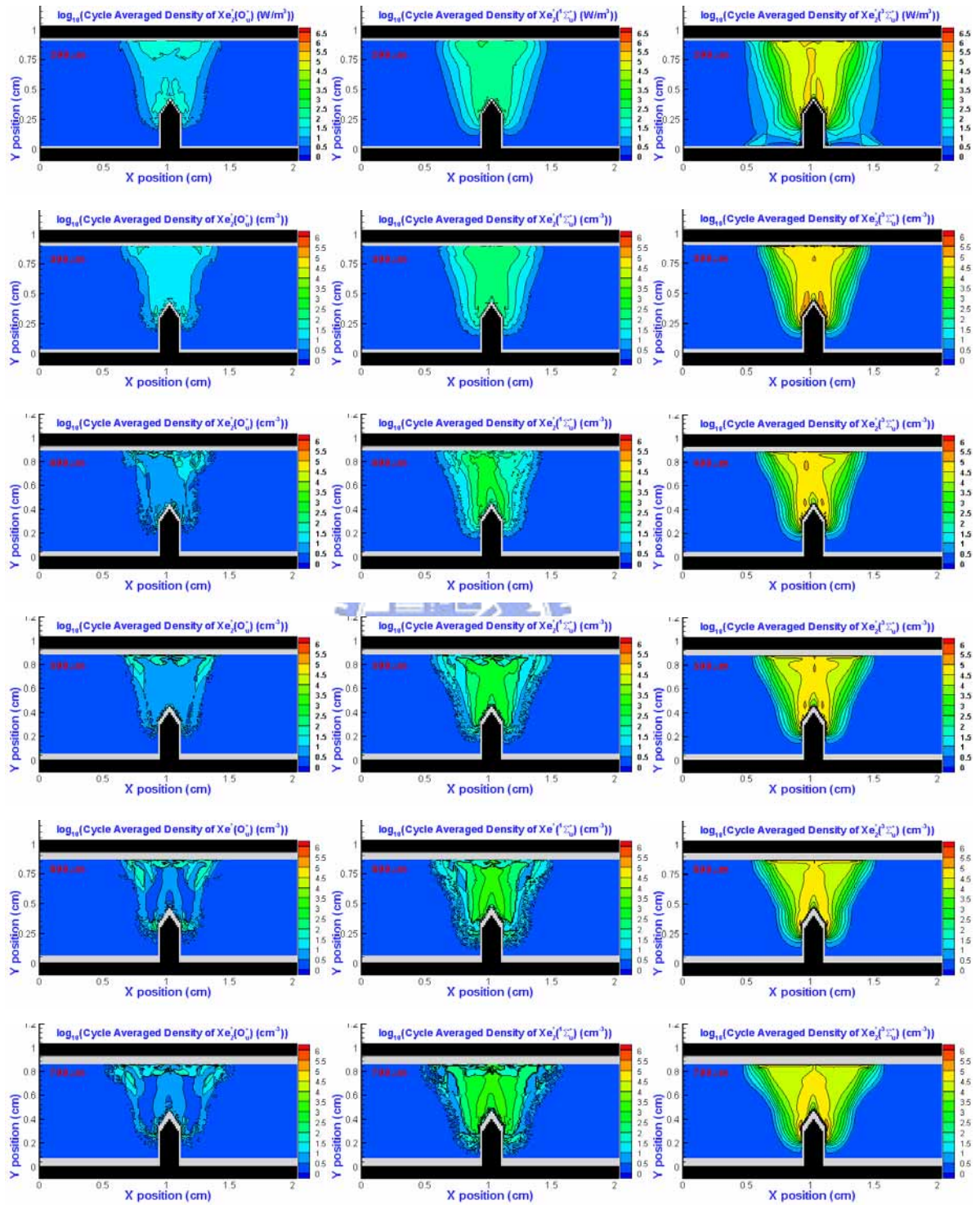


Figure 4.32. Cycle averaged densities of excited species, $\text{Xe}^*(O_u^+)$, $\text{Xe}^*(^1\Sigma_u^+)$, and $\text{Xe}^*(^3\Sigma_u^+)$ versus dielectric thickness 200~700 μm .

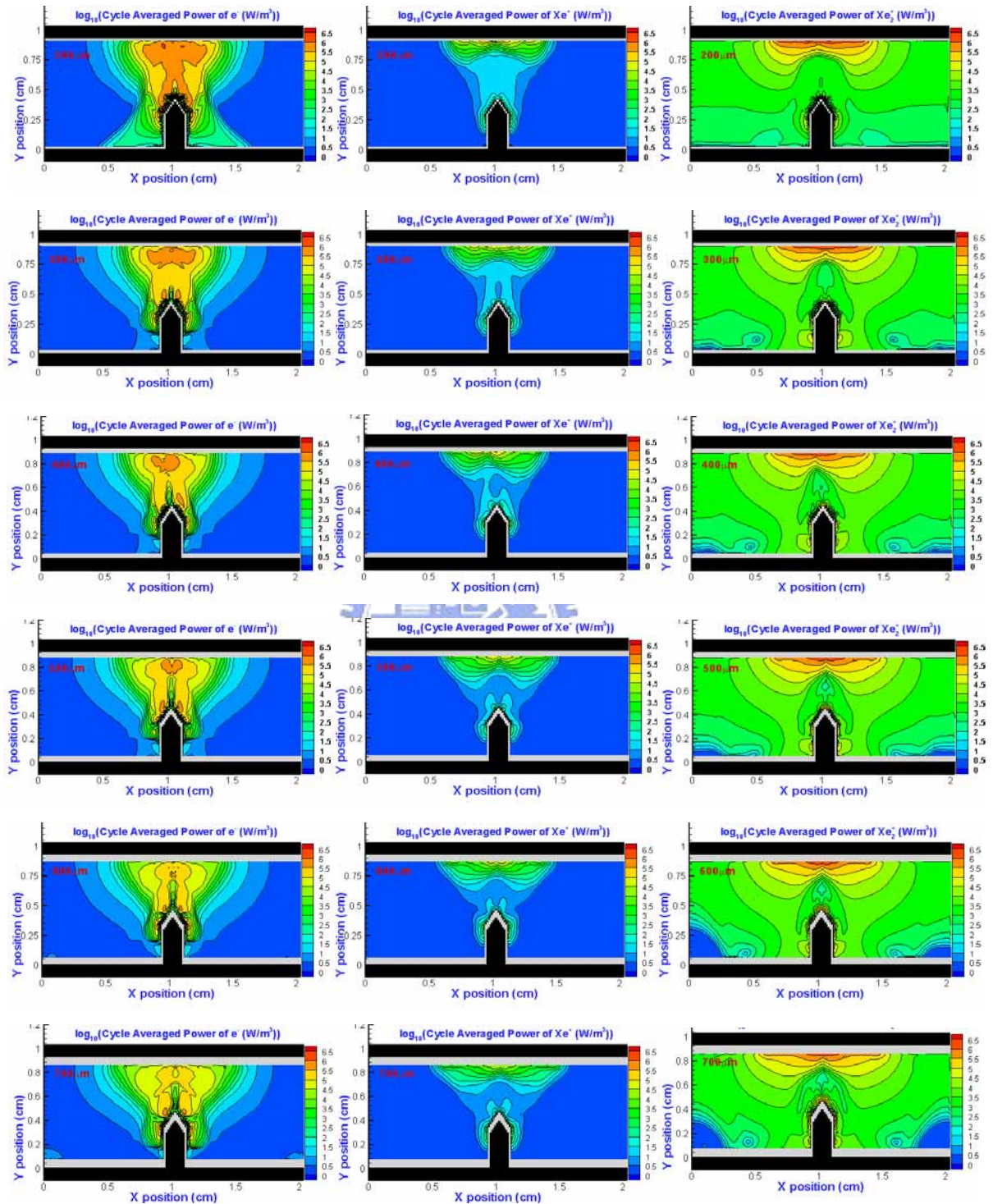


Figure 4.33. Cycle averaged powers of charged species, e^- , Xe^+ , and Xe_2^+ versus dielectric thickness 200~700 μm .

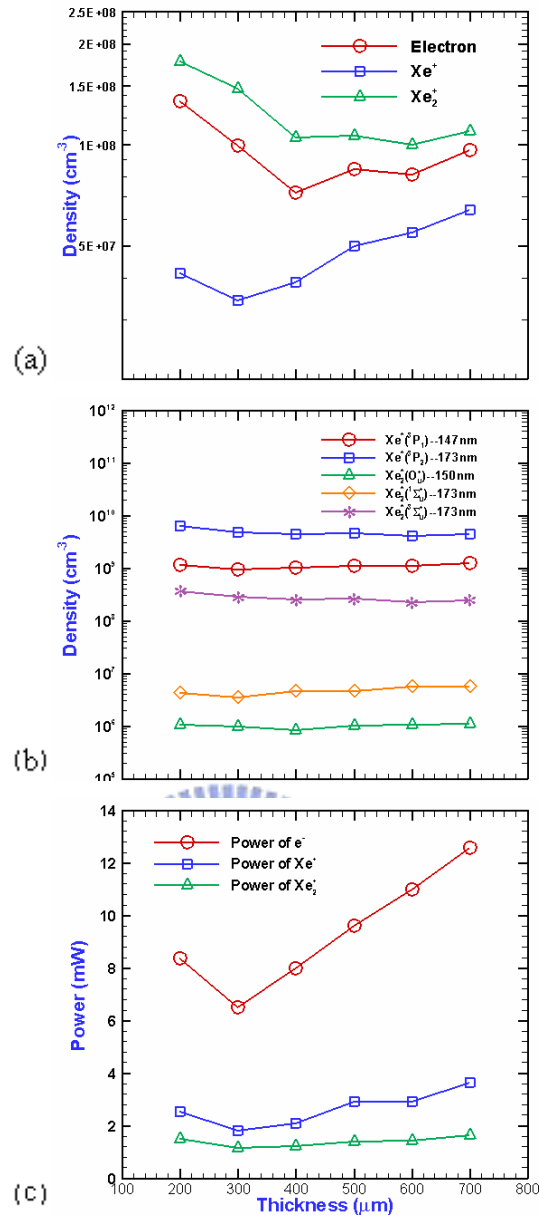


Figure 4.34. The averaged quantities (a) charged species densities, (b) excited species densities, and (c) charged species powers versus dielectric thickness 200~700μm.

Table 7. Details of averaged quantities versus dielectric thickness 200~700μm.

Thickness (μm)	e ⁻ (%)	Xe ⁺ (%)	Xe ₂ ⁺ (%)	Xe [*] (P ₁) (%)	Xe [*] (P ₂) (%)	Xe ₂ [*] (O _u ⁺) (%)	Xe ₂ [*] (Σ _u ⁺) (%)	Xe ₂ [*] (Σ _u ⁺) (%)	Power of e ⁻ (%)	Power of Xe ⁺ (%)	Power of Xe ₂ ⁺ (%)
200	139.18	64.59	160.97	94.86	139.92	95.50	76.52	148.15	66.70	69.76	92.10
300	102.77	53.72	134.00	76.22	107.79	88.87	63.68	114.16	51.88	50.57	72.11
400	74.50	60.93	95.46	83.84	98.23	75.96	82.00	101.92	63.65	57.97	75.78
500	87.69	78.02	97.05	91.27	102.53	92.38	83.97	105.32	76.48	80.34	86.46
600	84.38	85.73	91.23	90.24	90.60	95.49	100.14	90.84	87.59	79.98	88.68
700	100.00	100.00	100.00	100.00	100.00	100.00	100.00	100.00	100.00	100.00	100.00
Quantity at 700 μm	5.28E+07 (cm-3)	2.64E+07 (cm-3)	8.51E+07 (cm-3)	6.26E+08 (cm ⁻³)	2.94E+09 (cm ⁻³)	5.58E+05 (cm ⁻³)	2.67E+06 (cm ⁻³)	1.69E+08 (cm ⁻³)	12.58 (mW)	3.65 (mW)	1.64 (mW)